

EXHIBIT 28

Effect of Heated-Air Blanket on the Dispersion of Squames in an Operating Room

Said Elghobashi

Mechanical and Aerospace Engineering
The Henri Samueli School of Engineering
4220 Engineering Gateway
University of California, Irvine
Irvine, CA 92697-3975
Phone: (949) 824-6131
Email: selghoba@uci.edu

March 23, 2017

Contents

1	Introduction	2
2	Operating Room Geometry and CAD Model	7
3	Numerical Simulation	11
3.1	Large-eddy Simulation (LES): Introduction and Need	12
3.2	Governing Equations	18
3.2.1	Gas-phase equations	19
3.2.2	Equations for calculating the trajectories of individual squames	20
3.3	Computational grid	23
3.4	Boundary Conditions	28
3.4.1	Inlet boundary conditions	28
3.4.2	Hot air blower and other heat sources	31
3.5	Numerical solution method	32
3.5.1	Advancing the Lagrangian squames equations	33
3.5.2	Advancing the Eulerian fluid flow equations	34
4	Results	36
4.1	Flow characteristics	37
4.2	Dispersion of squames	42
4.2.1	Initial locations of squames	42
4.2.2	Trajectories and snapshots of squames	47
4.2.3	Number density of squames in the regions of interest	55
5	Summary and Concluding Remarks	60
Appendices		63
Appendix A		63
Bibliography		65

Effect of Heated-Air Blanket on the Dispersion of Squames in an Operating Room

Abstract

A large-eddy simulation (LES) of the interaction between the ventilation air flow and forced hot air from a blower is performed to investigate the effect of hot air on dispersion of squames in a realistic operating room (OR) consisting of an operating table (OT), side tables, surgical lamps, medical staff, and a patient. Two cases with blower-off and blower-on are calculated together with Lagrangian trajectories of 3 million squames initially placed on the floor surrounding the OT. The squames particles are assumed as spheres of size 10 microns and the drag, lift and buoyancy forces are considered in calculating their instantaneous motion. It is shown that with the blower-off, squames are quickly transported by the ventilation air away from the table and towards the exit grilles. However, with the hot air blower turned on, the ventilation air flow above and below the OT is disrupted significantly. The rising thermal plumes from the hot blower air drag the squames above the OT and the side tables and then they are blown downwards toward the surgical site by the ventilation air from the ceiling. Temporal history of number of squames particles reaching four imaginary boxes surrounding the side tables, the OT, and the patient's knee shows that several particles reach these boxes with the blower turned on. The study shows that LES is necessary to accurately capture the mixing and transport in a turbulent flow and predict the dispersion of squames in an OR.

¹ 1 Introduction

² Microbial skin colonizers, such as *Staphylococcus aureus*, have been known as a major cause of
³ surgical site infections in operating rooms (Noble, 1975; Clark & de Calcina-Goff, 2009; Wood
⁴ *et al.*, 2014). These bacteria typically colonize on human skin cells or squames which are routinely
⁵ shed by humans, roughly about 10^7 particles per day (Noble, 1975). The squame particle size ranges
⁶ over 4–20 μm of equivalent diameter (Noble *et al.*, 1963; Lees & Brighton, 1972).

⁷ Reduction of post-operative surgical site infections has been linked to two main factors: (i)
⁸ ultra-clean ventilation (UCV) systems, and (ii) perioperative patient warming (Ng *et al.*, 2006; Legg
⁹ *et al.*, 2012; Wood *et al.*, 2014). Ultra-clean ventilation aims to reduce the quantity of airborne
¹⁰ bacteria in the operating room (OR) and most importantly near the surgical site. This is typically
¹¹ achieved by the constant delivery of highly filtered ultra-clean air with a downward uniform velocity
¹² of 0.3-0.5 m/s (McGovern *et al.*, 2011). The UCV performance depends critically on volumetric
¹³ airflow, proper temperature gradients, use of uniform downward flowing ventilation air, potentially
¹⁴ in the laminar regime (Memarzadeh & Manning, 2002; Pereira & Tribess, 2005). Surgeons and
¹⁵ other medical equipment within the operating room (surgical lights, tables, patient, computers, etc.),
¹⁶ motion of surgeon's arms and their bending motion (Chow & Wang, 2012) can disrupt this air flow

17 and create wakes, flow unsteadiness, and turbulence, thereby increasing the amount of cfu in the
 18 OR.

19 Perioperative patient warming is the other important clinical practice to prevent inadvertent sur-
 20 gical hypothermia, wherein the core temperature of the patient drops below 36°C. Preventing in-
 21 advertent perioperative hypothermia has several benefits that include reduced operative blood loss,
 22 reduced duration of surgery, improved wound healing, reduced wound infections, reduction in post-
 23 operative ulcers, reduced duration of hospital stay, and increased survival rates (*Wood et al., 2014;*
 24 *Ng et al., 2006; Legg et al., 2012*). Monitoring and maintaining body temperature during surgery is
 25 therefore an accepted and required practice. *Warttig et al. (2014)* review different methods used to
 26 combat inadvertent perioperative hypothermia. These include use of warm cotton blankets, reflective
 27 blankets, warmed intravenous and irrigation solutions, circulating warm water mattresses, a reusable
 28 electric blanket, an electric heating pad, and forced-air warmers (*Kellam et al., 2013; Austin, 2015*).
 29 Of these, active warming using forced air warming (FAW) devices, and passive warming based on
 30 the use of reflective blankets, are the two main techniques used to keep the patient's body warm
 31 and prevent hypothermia. Although passive heating techniques may show similar effectiveness as
 32 the FAW devices, the latter have been used for over two decades due to their efficacy in maintain-
 33 ing patient's core body temperature. These techniques use forced convection to increase the skin
 34 temperature and the total body heat content. These devices contain a blower (such as 3M™ Bair
 35 Hugger™) that extracts the room temperature air through an air-intake filter heats the air using a
 36 heating coil, and vents the air into the sterile field adjacent to the operative site (*Albrecht et al.,*
 37 *2011; Leaper et al., 2009; Wood et al., 2014*). The filtered and warm air flows through a connecting
 38 hose into blankets made of plastic and exits the blankets through tiny holes over the patient's skin.
 39 However, this forced warm air has the potential to generate and mobilize airborne contamination in
 40 the operating room.

41 A number of studies have examined at the safety of forced-air warming, and whether FAWs
 42 can affect surgical site infections through mobilized airborne contamination. FAWs can potentially
 43 lead to surgical site contamination in two ways: (i) direct contamination of the air from the blowers
 44 that reaches the patient's body, and (ii) disruption of the ultra-clean ventilation air by the thermal
 45 plumes and turbulence. The former risk can potentially be reduced by using intake filers that are
 46 HEPA-rated and show high filtration efficiency. The latter has been studied extensively as reviewed

47 by [Wood et al. \(2014\)](#). It is hypothesized that the temperature gradients and resultant thermal plumes
 48 created by the FAW devices could disrupt the benefits of UCV flow, that is designed to be uniform
 49 and downwards. The interaction between the FAW and UCV flows may lead to increased surgical
 50 site infections (SSI).

51 [McGovern et al. \(2011\)](#); [Legg et al. \(2012\)](#) have shown that temperature gradients and excess
 52 heat created by FAW devices can transport air from the unsterilized floor level to the surgical site,
 53 thus increasing the potential risk of SSIs. [Moretti et al. \(2009\)](#) measured an increase in the bacterial
 54 load when FAWs were used. Lack of flow visualization is the main drawback of these studies as
 55 it does not provide information about whether the particles came from the floor or from the FAW
 56 blower. [Legg et al. \(2012\)](#); [Sessler et al. \(2011\)](#) used smoke particle visualization to understand the
 57 source of these particles near the surgical site comparing cases with no warming, FAW, and radiant
 58 warming. Although they found that FAW increased the particle count with blower turned on (almost
 59 10-fold increase), they also showed that the uniform, laminar flow from the ultra-clean ventilation
 60 reduced the effect of particles by limiting their numbers near the surgical site.

61 It is clear from the available literature that the interaction between the UCV flow and the rising
 62 plumes from the forced-air warming devices plays a critical role in deciding whether FAWs indeed
 63 can lead to increased number of particles near the surgical site. However, there have not been de-
 64 tailed experimental measurements of flow patterns in the OR setting with the FAW blower turned on.
 65 Recently, [McNeill et al. \(2012, 2013\)](#) conducted particle-image velocimetry (PIV) measurements
 66 to understand the flow pattern in an OR with the ultra-clean ventilation system. This study, however,
 67 did not investigate the effect of FAW blower. [McNeill et al. \(2013\)](#) also made detailed measure-
 68 ments of temperature fields on surgeon's and patient's body to be used for computational modeling.
 69 Although the above PIV was able to visualize and measure the flow field, it was limited to planar
 70 data (2D PIV) and thus a full three-dimensional data are not available for the OR. Nevertheless,
 71 some useful information on the flow unsteadiness, turbulence within the room was obtained from
 72 the [McNeill et al. \(2013\)](#) study.

73 The only other way to characterize the flow field in an OR with and without FAW blowers,
 74 is to use computational fluid dynamics (CFD) modeling in three-dimensions. This, however, is
 75 a difficult task due to the size and complexity of the domain involving medical equipment, staff,
 76 computers, etc. There are only few CFD studies in the literature that used Reynolds-averaged Navier

77 Stokes (RANS) models ([Memarzadeh & Manning, 2002](#); [Memarzadeh, 2003](#); [Chow & Wang, 2012](#)),
 78 wherein only the time-averaged velocity field is computed. All information about the turbulence and
 79 velocity fluctuations is completely *modeled*. As is shown later (section 3), RANS approach is not
 80 predictive, since the instantaneous velocity field needed for calculating the trajectories of squames is
 81 not directly computed. Thus, RANS is incapable of accurately predicting the locations of squames at
 82 any time in the OR. [Memarzadeh & Manning \(2002\)](#); [Memarzadeh \(2003\)](#) investigated the effect of
 83 various UCV inlet flow conditions on the transport of squames particles in an OR. They considered
 84 a realistic OR with medical staff, equipment, surgical lamps, etc. and accounted for the thermal
 85 plumes created by heat radiated from various sources. However, they used a RANS model coupled
 86 with a Lagrangian particle-tracking of around 4000 representative particles. Their study did not
 87 include the FAW blower discharge. They showed that use of a uniform inlet flow with laminar
 88 conditions¹ is better for reducing the number of particles near the surgical site. In addition, they
 89 found that the thermal plume created by the hot surface of the surgical site prevented particles from
 90 reaching the site. They showed that roughly 2-5% of particles reach the surgical site, *provided they*
 91 *are originated very close, about 1.3cm above the site*. Particles originating from locations away
 92 from the surgery did not have a statistically significant probability of reaching the surgical site. As
 93 is discussed later in section 3, RANS model cannot compute the instantaneous velocity field needed
 94 to accurately calculate the forces on particles, and particle trajectories.

95 [Chow & Wang \(2012\)](#) investigated the ultra-clean ventilation flow and its effect on bacteria-
 96 carrying particles in an OR using a RANS model as well. They simulated the bacteria particles as
 97 a non-inertial pollutant, wherein an Eulerian transport equation for the concentration of the bacteria
 98 is calculated. In addition, they considered periodic bending movement of one of the surgeons per-
 99 forming the operation. They found that if the surgical staff stands upright (no bending), the UCV
 100 flow keeps the bacteria concentration very low (< 1 cfu/m³) near the surgical site. However, with
 101 the surgeon's bending motion included, they showed that this concentration increased to larger than
 102 the recommended value (10 cfu/m³).

103 All of the above computational studies are based on RANS modeling and did not include the

1It should be noted that the literature uses the terminology ‘laminar flow’ for the ultra-clean ventilation flow. Based on the standard values of air changes per hour (ACH) for an OR (25 per hour), the inlet grille sizes, and properties of air, the flow Reynolds numbers are much larger than 2000, a critical value beyond which turbulence occurs in a duct. The inlet grille flow, thus is not typically laminar. Although the level of turbulence in the inlet flow is not large (< 10%), the flow contains velocity fluctuations and is unsteady.

104 FAW blower system together with a blanket cover above the patient. In order to assess the in-
 105 teraction between UCV and FAW blower, a systematic, predictive simulation is needed. Large-
 106 eddy simulation (LES) is a numerical technique that involves computing the properties of the large,
 107 energy-containing eddies of turbulence accurately, without any user adjustable tuning parameters,
 108 and models only the more homogeneous, small scales of turbulence (Pope, 2000; Piomelli, 2014).
 109 This technique provides the instantaneous three-dimensional velocity, temperature, and pressure
 110 fields and has been shown to be far more accurate than the RANS model. Section 3 outlines the dif-
 111 ferences between LES and RANS in detail. In addition, since the time dependent, three-dimensional
 112 velocity field is available in LES, then the forces on particles and their trajectories can be calculated
 113 accurately (Apte *et al.*, 2003b; Ham *et al.*, 2003; Apte *et al.*, 2009; Moin & Apte, 2006; Mahesh
 114 *et al.*, 2006). The only challenge with this technique is that it is computationally intensive and re-
 115 quires fine grid resolutions and small time-steps to capture the large-scales of turbulence. Recent
 116 advances made in algorithmic developments for LES on arbitrary shaped, unstructured grids (Ma-
 117 hesh *et al.*, 2004; Ham *et al.*, 2003; Moin & Apte, 2006; Mahesh *et al.*, 2006; Ham & Iaccarino,
 118 2004) have facilitated application of LES to more realistic problems involving complex geometries
 119 and flow conditions. These advances have been successfully applied to turbulent, reacting flows in
 120 a gas-turbine combustion chamber and has led the gas-turbine industry to switch from RANS to the
 121 predictive LES technique in their design cycle (Moin & Apte, 2006; Mahesh *et al.*, 2006; Apte *et al.*,
 122 2009).

123 LES applied to operating rooms with medical staff and other instruments is still challenging,
 124 owing to the size of the room and the complexity of the geometries involved. At the time of writing
 125 this report, only one LES study has been performed for an operating room by Saarinen *et al.* (2015).
 126 They studied the escape of air into an isolation room during opening and closing of a door and
 127 passage of a human figure. They used passive smoke visualizations to compute the volume flux
 128 of air when a door is opened. Although this study had some complex geometry (a human figure),
 129 it did not have the intricacies of the OR table, surgeons, patient and other medical equipment, nor
 130 it computer the dispersion of squames in the OR. Nevertheless, it showed that LES can accurately
 131 predict such flows through validation with experimental observations.

132 The main goal of the work reported here is to use large-eddy simulation to compute the in-
 133 teraction of the OR ultra-clean ventilation air flow and the flow created by forced air warming

134 system (such as 3MTM Bair HuggerTM) and investigate their impact on the dispersion of squames.
 135 Specifically, computations are conducted for the cases with blower-off and blower-on, including the
 136 Lagrangian tracking of inertial squame particles, starting from the operating room floor, to prove
 137 whether the FAW system and the resultant thermal plumes play a role in transporting squame parti-
 138 cles to the surgical site.

139 The rest of the report is arranged as follows. In section 2, details of the operating room geometry
 140 and CAD model are described. This includes the OR dimensions, the surgical lamps, four medical
 141 staff, an operating room table, two side tables, the blower, and the patient undergoing knee surgery.
 142 The numerical approach is described in section 3. This includes a detailed discussion of LES and
 143 RANS, the governing equations used for LES, the computational grid, and the boundary conditions.
 144 The numerical algorithm used is briefly summarized in section 3.5. This is followed by detailed
 145 description of the results in section 4 on flow field, particle trajectories and particle counts that reach
 146 the surgical site and other key regions of interest. Finally, the findings are summarized in section 5.

147 2 Operating Room Geometry and CAD Model

148 The operating room CAD (computer aided design) model was created using Ansys[®] SpaceClaim
 149 Direct ModelerTM (ANSYS, Inc., Canonsburg, PA, USA). The CAD model replicated a realistic
 150 operating room (OR) depicting a knee surgery being performed on a patient. An original baseline
 151 CAD model was obtained from M/E Engineering P.C. ([Straub, 2016](#)) and was further modified
 152 to incorporate the measured dimensions of the inlet air grilles and the surgical drape as shown
 153 below. Figure 1a shows the OR dimensions used to create the CAD model. The length, width
 154 and height of the room are 7.32m, 7.01m and 3.18m, respectively. These dimensions are from 3M
 155 video at: <https://www.youtube.com/watch?v=QhzeInWIJ54>. Figure 1b shows a close-up view of the
 156 surgeon's hands extended over the patient's knee mimicking a real world operating procedure.

157 The CAD model also includes several objects that are usually present in a real OR. Typically,
 158 there can be several combinations of such objects, but for this study the following objects were
 159 included in the model. These are shown in a top view in figure 2 and include: (i) OR Table; (ii) OR
 160 drape; (iii) patient's body under the drape with knee exposed; (iv) four surgeons (two of the surgeons
 161 have extended hands and two have hands down), (iv) two side tables, (v) two surgical lamps, (vi)

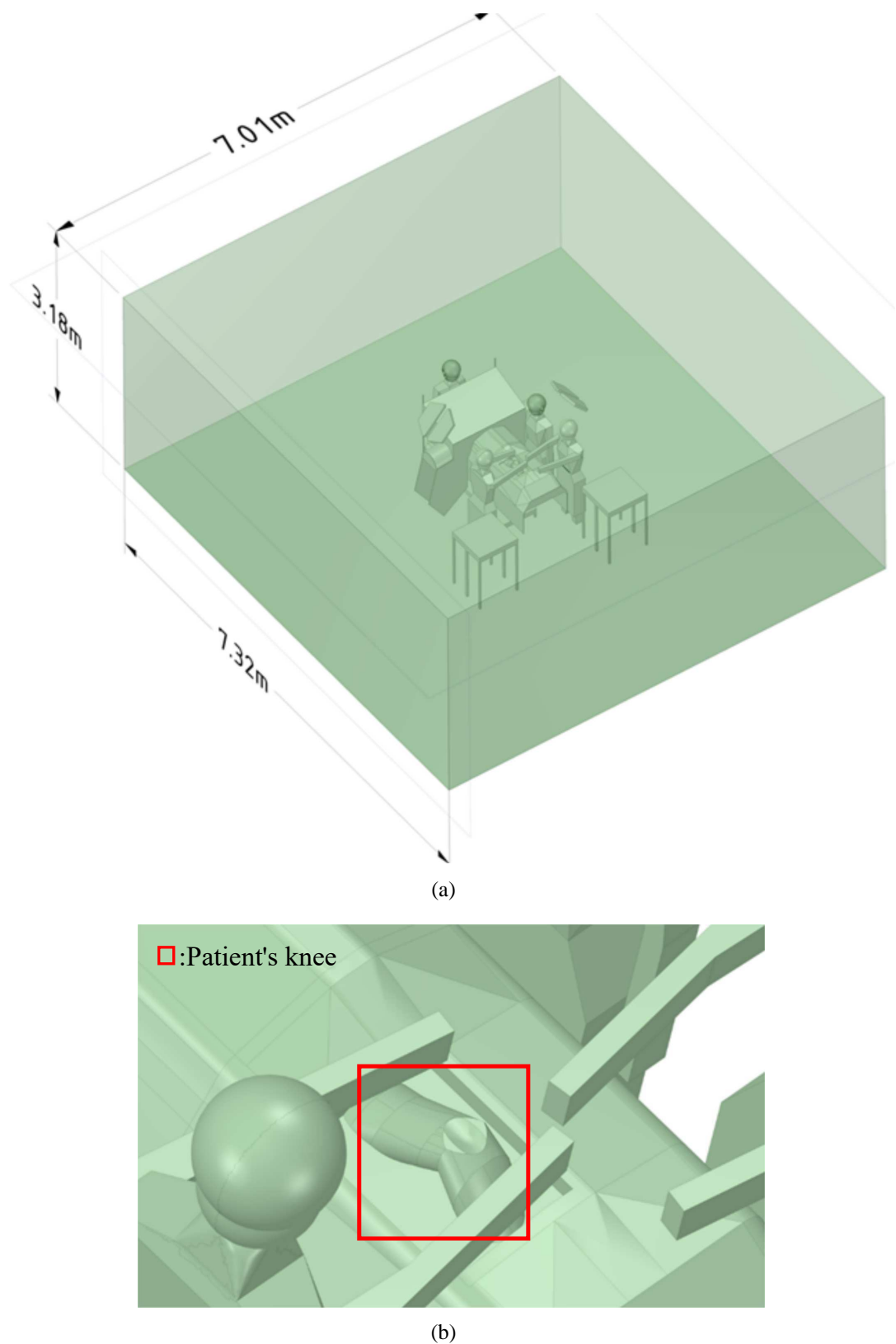


Figure 1: CAD model showing (a) operating room dimensions, and (b) closeup of the patient's knee.

3MTM Bair HuggerTM blower unit (partly visible near the top left corner under the drape).

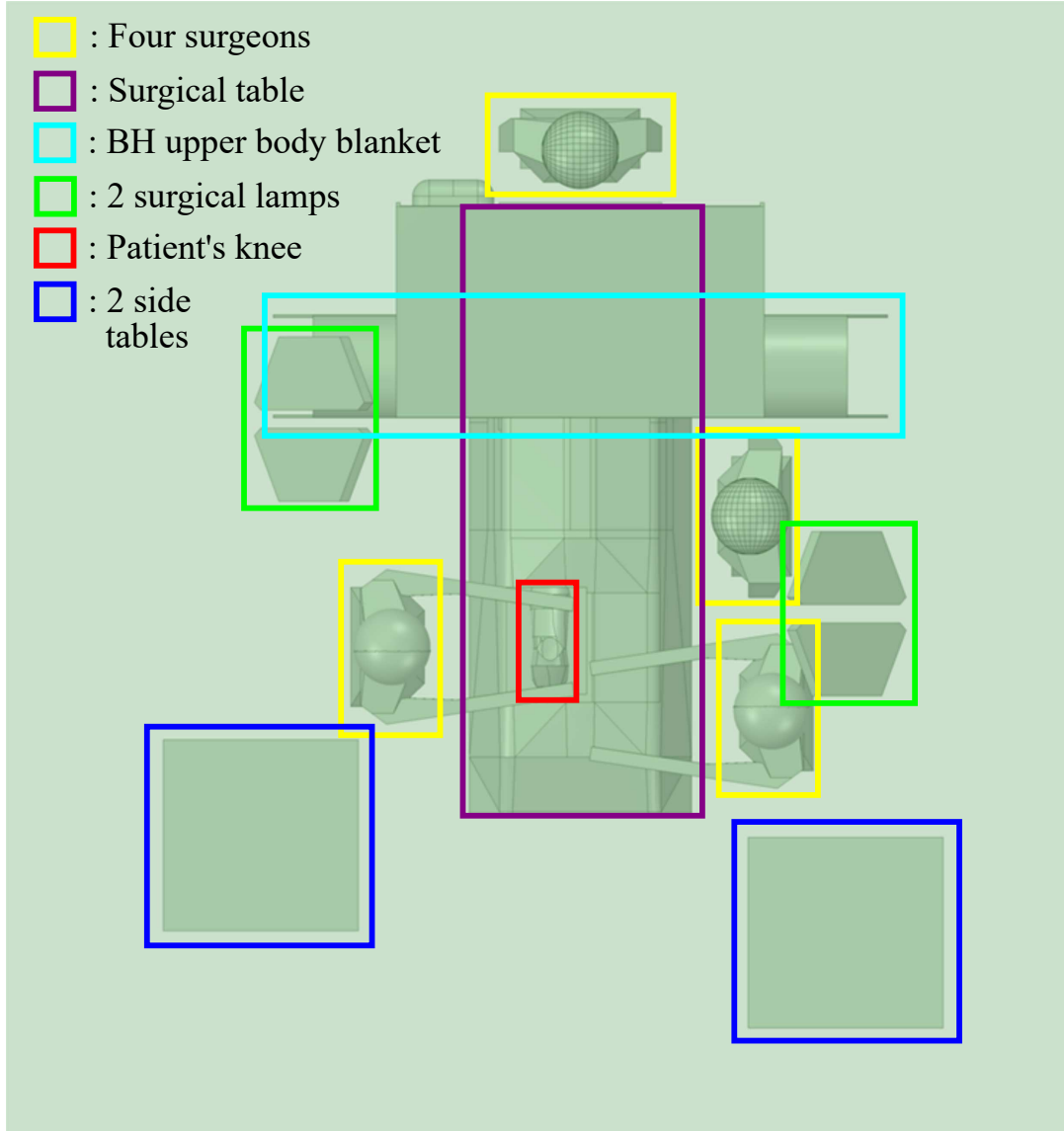


Figure 2: Close-up view of various objects included in the CAD model.

162

163 Figure 3 shows a side view of the OR table together with a few key dimensions. The bottom of
 164 the OR table is 0.94m above the floor of the room. The drape on the OR table covering the patient's
 165 torso is suspended 0.52m above the floor. The 3MTM Bair HuggerTM blower unit is also seen in the
 166 bottom right side of the figure.

167 The drape design from the base CAD model was modified to better represent the drape layout in
 168 a real OR room. The modifications mainly focused on using accurate dimensions and shape of the
 169 drape near the front end based on an actual picture taken in an OR room as shown in figure 4b. A
 170 corresponding CAD model used in the present study is shown in figure 4a. For the CAD model, the

□:Patient's knee □:BH Blower
□:Drape of the BH blanket

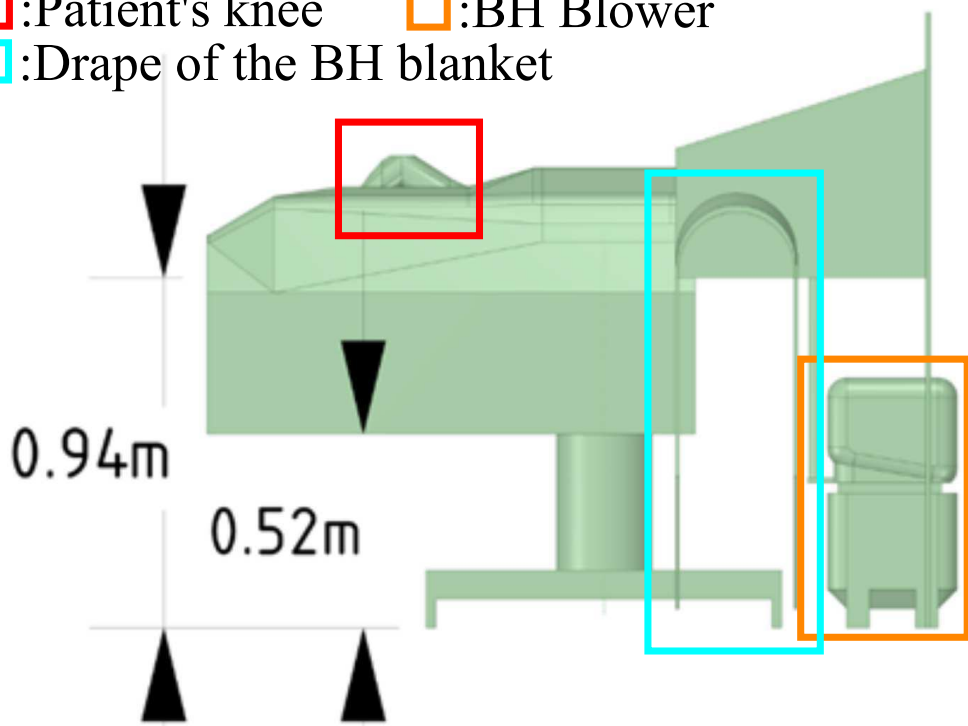


Figure 3: Side view of the OR table with some key dimensions. The 3M™ Bair Hugger™ blower unit is clearly visible on the bottom ride side.

171 front end of the drape was designed to mimic the shape obtained by dimensions A, D, C, E in figure
 172 4a. The dimensions in the CAD model are given in both metric and imperial units (in brackets) in
 173 this figure to facilitate direct comparison with the real picture on the right. The distance between the
 174 vertical bars holding the drape, denoted by dimension F in Figure 4b, was also implemented in the
 175 CAD model.

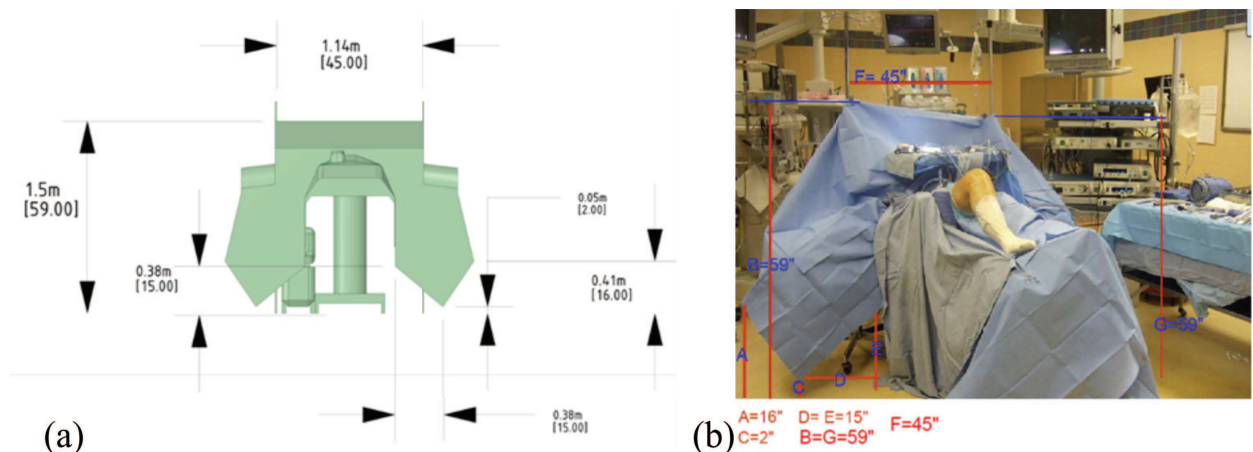


Figure 4: Drape dimensions and configuration: (a) model developed to match the drape dimensions, (b) actual drape picture in an OR room. The dimensions are shown in both metric and imperial units (in brackets).

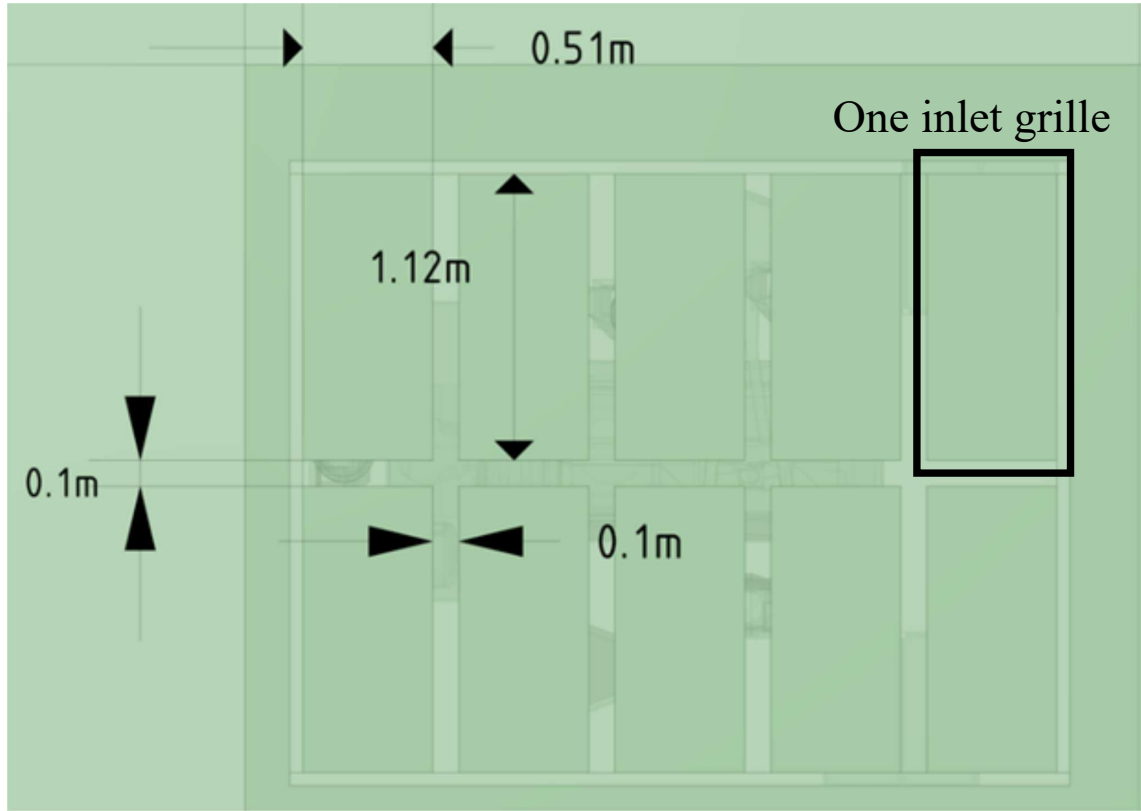


Figure 5: Ten inlet grills to supply clean filtered air into the OR.

176 The CAD model included ten inlet grilles (figure 5) for supplying clean filtered air to the OR.

177 Each inlet grille is 0.51m in width and 1.12m in length. All ten grilles are of the same size. There is
178 a gap of 0.1m between the neighboring grilles at all sides.

179 There are four exhaust (or outlet) vents, two on each side wall. Figure 6 shows two outlet grilles
180 (with the other two outlets located on the opposite wall). Each outlet grille is 0.71m in width and
181 0.71m in length.

182 3 Numerical Simulation

183 A state-of-the art, fully parallel, unstructured, co-located grid flow solver based on principles of
184 kinetic energy conservation for large-eddy simulation ([Moin & Apte, 2006](#)) of turbulent flow in
185 the limit of zero-Mach numbers is used in this study. This solver is MPI-based, uses algebraic
186 multigrid for the pressure Poisson equation, and third-order WENO-based scheme for transport of
187 scalar fields such as temperature. It has been thoroughly validated for a number of different particle-
188 laden turbulent flows ([Apte et al., 2003b,a, 2008a, 2009, 2008b](#)) including swirling turbulent flow

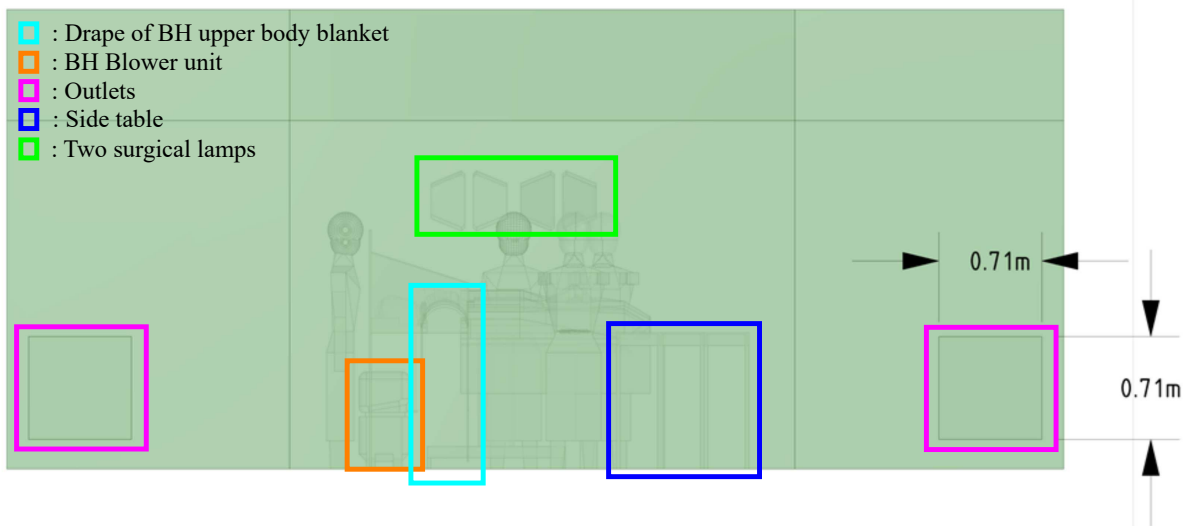


Figure 6: Outlet (exhaust) grilles for air exit from the room. Out of the four outlets in the CAD model, only two are visible in the picture. The other two outlets are on the the opposite wall.

189 in a co-axial combustor, turbulent reacting flow, as well as spray combustion in a realistic Pratt and
 190 Whitney gas-turbine combustion chamber ([Moin & Apte, 2006](#); [Mahesh *et al.*, 2006](#)).

191 **3.1 Large-eddy Simulation (LES): Introduction and Need**

192 The physics of turbulent air flow containing heated buoyant plumes and laden with inertial particles
 193 in a real-life operating room is highly complex. Simulating such flows with predictive capability is
 194 difficult as turbulence, by nature, consists of a broad range of length- and time-scales and is inher-
 195 ently three-dimensional. In addition, the geometry of a realistic operating room consists of complex
 196 surfaces involving surgeons, operating table, surgical lights, patient, among other. If a probe mea-
 197 sures the velocity at a certain location in such a flow, the velocity signal will show a broad range of
 198 frequencies and fluctuations around a mean. A typical kinetic energy spectrum obtained via Fourier
 199 transform of turbulent velocity field is shown in figure 7, especially for moderate to large Reynolds
 200 numbers. The spectrum is broad-band with large amount of kinetic energy per wavenumber present
 201 at large scales (small wavenumbers) and small amount of energy present at smaller scales (larger
 202 wavenumbers). There also exists an inertial range, scales in this regime simply transfer the energy
 203 from larger scales to smaller scales through a process commonly known as the energy cascade ([Pope,](#)
 204 [2000](#)). As the Reynolds number increases, this spectrum is known to broaden. The largest scales
 205 (\mathcal{L}) of motion are typically confined by the size of the domain (for example, size of the inlet jet

206 or size of the room). However, as the Reynolds number increases, the smallest scales of motion
 207 (known as the Kolmogorov scales, η) are reduced until the kinetic energy is dissipated into internal
 208 energy by the viscous effects. Owing to this broad range of scales, prediction of turbulent flows at
 209 large Reynolds numbers becomes difficult and is only possible if the behavior of all scales of motion
 210 is captured properly.

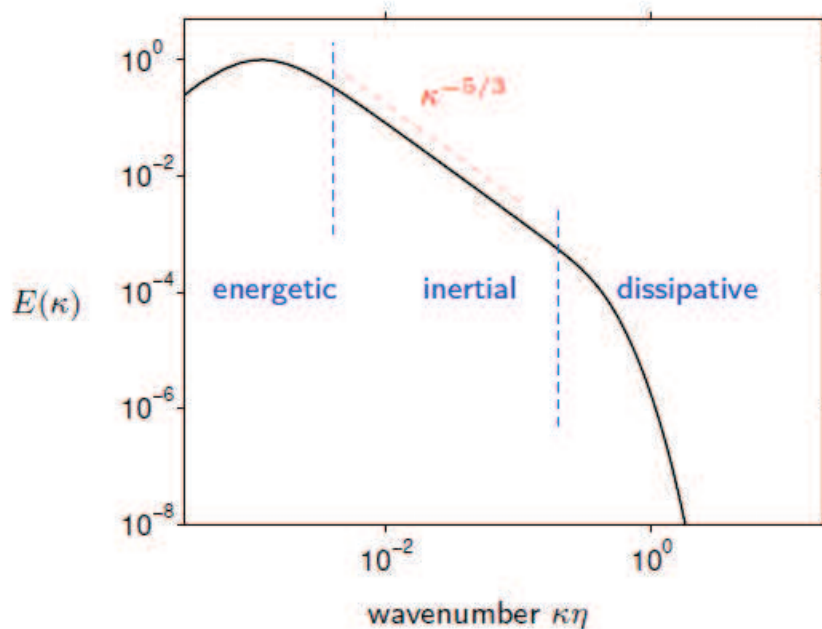


Figure 7: Schematic of a turbulence kinetic energy spectrum showing energy per wavenumber as a function of the wavenumber (Pope, 2000). The inertial range of scales is indicated by the $-5/3$ slope line that separates the energetic large scales and dissipative small scales of turbulence. In DNS, the grid resolution is fine enough to capture all scales, whereas in LES, the grid resolution is coarser (typically 10 times the Kolmogorov length scale), placing the grid cut-off somewhere in the inertial range.

211 Three basic approaches can be identified for prediction of turbulent flows: (i) direct numerical
 212 simulation (DNS), (ii) Reynolds averaged Navier-Stokes (RANS) modeling, and (iii) large-eddy
 213 simulation (LES), and are briefly described below.

214 **DNS:** In direct numerical simulation (DNS), the Navier-Stokes equations are solved on a com-
 215 putational grid that is fine enough, in space and time, to directly capture *all* the scales associated
 216 with the fluid flow motion without requiring any additional models. This means that the computa-
 217 tional grid in three-dimensions is small enough to capture the smallest scales of turbulence and the
 218 time-step is small enough to capture the smallest time-scale associated with the flow. Using scaling
 219 arguments based on the Kolmogorov hypotheses (Tennekes & Lumley, 1972; Pope, 2000) used in
 220 the theory of turbulence, it can be shown that for a simple homogeneous, isotropic turbulence in a
 221 box, the grid resolution requirement ($\Delta \sim \mathcal{L}/\eta$; where \mathcal{L} is the size of the large, energy-containing

eddies) for DNS varies as $Re_{\mathcal{L}}^{3/4}$, where $Re_{\mathcal{L}}$ is the Reynolds number based on \mathcal{L} and the velocity fluctuations u , in one coordinate. Hence, the total number of mesh points needed in three-dimensions varies as $Re_{\mathcal{L}}^{9/4}$. A simple isotropic turbulence in a box at $Re_{\mathcal{L}} = 2000$, would require computational grid containing about 27M control volumes ($= 300^3$). In addition, based on numerical constraints of a computational solver, for a fluid flow of unit velocity, the grid spacings (Δ) and the time-steps (Δt) are roughly of the same order of magnitude ($CFL = u\Delta t/\Delta \sim 1$) and thus the spatio-temporal resolution will require a computational power that increases as $Re_{\mathcal{L}}^3$. Owing to the grid requirements and associated computational costs, DNS is not practical for realistic engineering applications and is restricted to canonical geometries and flow problems to study the fundamentals of turbulence (Moin & Mahesh, 1998).

RANS: According to the above discussion, the computation of practical turbulent flows relies predominantly on the Reynolds-averaged Navier-Stokes (RANS) equations approach. In RANS, the governing equations are averaged in time to obtain equations for the *time-averaged* velocity field, $\bar{u}(\mathbf{x})$. Thus, in this approach, only the mean velocity field that varies in space is obtained, and all information about the time-dependent fluctuations of the velocity field around the mean flow is lost. Because the momentum equations are non-linear (owing to the inertial, advective terms), a time-average of the non-linear term creates additional quantities that are unknown, giving rise to the classical closure problem of turbulence (Tennekes & Lumley, 1972; Pope, 2000). In order to evaluate these terms, models are introduced wherein the effect of the entire spectrum of turbulence (involving the large, inertial, and small scales shown in Figure 7) is completely modeled. This is usually done by introducing two additional transport equations for the turbulence kinetic energy (k) and the kinetic energy dissipation rate (ε), giving rise to the $k - \varepsilon$ model. It should be noted that the transport equations for k and ε also contain a large number of unknown, unclosed terms which also need to be modeled. The model constants are obtained by fitting the RANS predictions to the experimental data on simple, canonical flows such as wall bounded channel flow, isotropic turbulence, or free-shear flows. Because these models and model constants *are not universal*, using them for a complex flow such as air circulation in an operating room, invariably provides inaccurate results. Experimental data is necessary to adjust the model constants and thus the RANS models are not *predictive*. However, since only the time-averaged velocity field is calculated, the RANS approach is computationally the least expensive because it does not require the spatio-temporal resolution

252 necessary for the DNS studies. There are modified approaches, wherein the large-time scale variations
 253 are captured by solving the RANS equations in an unsteady manner. These unsteady-RANS
 254 simulations also suffer from the same hypotheses and models used for the basic RANS and their
 255 predictive capability is also poor.

256 **LES:** The energy spectrum (figure 7) shows that a substantial portion of the turbulence kinetic
 257 energy (TKE) is contained in the large-scales, known as the energy containing scales. In LES, only
 258 the contribution of the large, energetic structures to momentum and energy transfer is computed
 259 exactly, and the effect of the small scales, also termed as unresolved or subgrid scales, of turbulence
 260 is modeled. Since the small scales tend to be more homogeneous, and less affected by the domain
 261 boundary conditions as compared to the large eddies, then the subgrid closure models used in LES
 262 are universal and can be applied to a range of flows as compared to the RANS closures. Owing to
 263 these differences between the LES and RANS approaches, LES has been shown to be far superior
 264 to RANS in accurately predicting turbulent mixing of momentum and scalar (Mahesh *et al.*, 2004),
 265 pollutant and heat transport, combustion (Pierce, 2001)), and particle dispersion (Apte *et al.*, 2003b;
 266 Ham *et al.*, 2003).

267 In LES, the Navier-Stokes (NS) equations are filtered in space (as opposed to time as done
 268 in RANS) using a local filter (Gaussian, box, spectral etc.) to obtain a filtered velocity field,
 269 $\bar{u}_i(\mathbf{x}, t)$ (Pope, 2000). Using the local grid resolution as a spatial filter, the small, under-resolved
 270 scales of turbulence are filtered out. However, applying the filtering operation to the inertial, non-
 271 linear terms in the NS equations, gives rise to the closure problem. The resulting additional terms
 272 need to be modeled. Most often, the models used to close the unknown terms, known as Reynolds
 273 stresses, are based on the same types of assumptions, such as the gradient diffusion hypothesis, as
 274 employed in RANS. However, the fact that, in LES, modeling is only applied to capture the effect
 275 of unresolved, subgrid scales, which are homogeneous and universal, the closure models work very
 276 well in a wide range of problems. A dynamic procedure, typically employed in LES subgrid scale
 277 modeling, renders the modeling process completely free of any tuning parameters in contrast to
 278 RANS. All constants in the model are obtained directly in the calculations and are not set by the
 279 user. As long as the grid resolution is sufficient such that the motion of the energy-containing large
 280 eddies is captured correctly, unlike RANS, the LES approach can then be used in a truly predictive
 281 manner.

282 In addition, away from the boundaries, a typical LES grid can be 10 times coarser than a DNS
 283 grid in each direction (that is 10 times the Kolmogorov scale), resulting in significant savings in the
 284 computational cost. This makes LES an attractive tool compared to the DNS. However, there are
 285 still several challenges. Just like DNS, the LES computations are inherently three-dimensional and
 286 time-dependent, making the cost of the calculation large as the important large-scale spatio-temporal
 287 variations in the flow must still be resolved. In addition, the computational algorithm must not add
 288 large amounts of numerical dissipation as it has been shown that dissipative numerical approaches
 289 mask the physical dissipation present in turbulent flows and provide inaccurate predictions ([Mittal & Moin, 1997](#); [Kravchenko & Moin, 1997](#)). These restrictions typically limits the use of LES to
 290 simple, canonical geometries and flows (as free-shear flows (jets, wakes, shear layers), wall bounded
 291 channel flows, or flow over backward facing step ([Pierce, 2001](#); [Piomelli, 2014](#))) for which the
 292 underlying algorithms are based on a non-dissipative schemes developed for structured Cartesian
 293 grids.

295 Applying LES to the complex and realistic geometries of engineering applications such as the
 296 the operating room; including the operating table, surgeons, patient and other equipment, or other
 297 applications such as gas-turbine combustors, propellers, among others, requires use of arbitrary
 298 shaped unstructured meshes. In recent years; however, considerable progress has been made in
 299 handling complex configurations and unstructured grids accurately ([Piomelli, 2014](#)). [Mahesh et al. \(2004\)](#);
 300 [Ham et al. \(2003\)](#); [Mahesh et al. \(2006\)](#) have developed a numerical algorithm for high-
 301 fidelity simulations of incompressible, variable density flows on unstructured grids. A novelty of
 302 their algorithm is that it is discretely energy-conserving which makes it robust at high Reynolds
 303 numbers *without numerical dissipation*. This makes LES applicable to complex configurations and
 304 it has been successfully used to simulate multiphase, spray combustion processes in a realistic Pratt
 305 and Whitney gas-turbine combustion chamber ([Moin & Apte, 2006](#); [Mahesh et al., 2006](#); [Apte et al., 2009](#)). These simulations are still computationally intensive, often requiring 3–4 weeks of
 306 simulation on parallel supercomputers, however, the detailed data obtained from the simulations are
 307 of significant importance to researchers and engineers since such information could not be obtained
 308 from laboratory experiments. This has led several gas-turbine industries, who generally use RANS
 309 in their design cycle, to switch from RANS-based approaches to LES.

311 Furthermore, turbulent flows laden with dispersed particles (either solid particles, or droplets or

312 bubbles) involve the complexity of capturing the dynamics of turbulence as well as that of the dis-
 313 persed phase. The physics of particle-turbulence interactions is complex (Elghobashi, 1994, 2006),
 314 and depending upon the magnitudes of the particle relaxation times relative to the Kolmogorov time
 315 scales, heavier-than-fluid particles (solid particles, droplets, squames) can exhibit behavior such as
 316 preferential clustering on the edges of vortices (Eaton & Fessler, 1994; Rouson & Eaton, 2001;
 317 Kulick *et al.*, 2006; Reade & Collins, 2000; Eaton & Segura, 2006), whereas, lighter-than-fluid
 318 particles (bubbles) can break the vortical structures (Ferrante & Elghobashi, 2004; Druzhinin &
 319 Elghobashi, 1998; Ferrante & Elghobashi, 2007; Sridhar & Katz, 1999).

320 RANS is not capable of capturing this complex physics of particles interacting with turbulence
 321 because only the mean velocity field is computed by RANS, yet it is commonly used owing to
 322 its low cost. However, if the objective is to accurately simulate the dispersion of inertial particles
 323 in a turbulent flow, then a three-dimensional, instantaneous velocity field is necessary to calculate
 324 the forces on the particles. Inertial particle trajectories and dispersion are strongly influenced by
 325 the spatio-temporal variations in the velocity fields. Hence, using only the mean velocity field
 326 provides inaccurate dispersion characteristics. An improved RANS to capture the transient effects
 327 uses a model for particle motion that utilizes the local turbulence kinetic energy and introduces some
 328 randomness (typically a Gaussian distribution) in the particle equations (Sommerfeld *et al.*, 1992) is
 329 necessary. Recent work on the dispersion of squames in an operating room and the effect of different
 330 inlet air flow conditions used RANS together with such a stochastic, Lagrangian particle-tracking
 331 algorithm (Memarzadeh & Manning, 2002). Such a model must be tuned by the user to calculate
 332 different particle-laden flows and can behave differently in free-shear versus wall-bounded flows. As
 333 can be seen from the results presented by Sommerfeld *et al.* (1992); Chen & Pereira (1998), particle
 334 dispersion predicted using a RANS approach for turbulent flows in a wide range of applications
 335 involving swirling, separated flows do not agree with the experimental data. However, the same
 336 flowfields computed using LES (Apte *et al.*, 2003b; Moin & Apte, 2006; Apte *et al.*, 2008b, 2009)
 337 show considerably better predictive capability and agree with the experimental data very well. In
 338 LES, the resolved instantaneous velocity field, which varies in time and space, at the particle location
 339 is used to compute the forces on the particles as opposed to the time-averaged velocity in RANS.
 340 Accordingly, the effect of the energetic, turbulence scales (of the order of the grid resolution and
 341 larger) are completely captured in LES, thus predicting its impact on particle dispersion directly.

342 To summarize, it is essential to use LES instead of RANS to accurately predict the air circulation
 343 and dispersion of squames in an operating room for the following reasons:

- 344 • LES provides a three-dimensional, instantaneous flow field (velocity, pressure, temperature)
 345 of the resolved, energetic, large-scales, and only models the effect of the unresolved, subgrid
 346 (small) scales of turbulence. The subgrid scales tend to be more homogeneous, and less
 347 affected by the domain boundary conditions and thus allow the appropriate use of the eddy-
 348 viscosity models to calculate their stresses. RANS, on the other hand, only calculates the
 349 time-averaged velocity field and models the effect of all the scales of turbulence on the mean
 350 flow, resulting in unrealistic flow predictions.
- 351 • The subgrid model constants used in LES can be obtained dynamically, thus making LES
 352 truly predictive without any user-defined tuning parameters, whereas RANS model constants
 353 are not universal and often require manual tuning.
- 354 • LES is considerably more accurate in predicting passive as well as inertial particle dispersion
 355 since the instantaneous, three-dimensional resolved velocity field is available for computing
 356 the forces on the particles. In RANS, a random perturbation must be added to the mean ve-
 357 locity field to construct an artificial, time-dependent, three-dimensional velocity field needed
 358 to calculate the particle motion. This renders the calculation of particle dispersion highly
 359 inaccurate.

360 3.2 Governing Equations

The air flow in an operating room involves temperature variations within the room owing to various sources of heat; such as the operating room lamps, heat radiated from the medical personnel bodies, hot air discharged from a blower system, among others. The local temperature variations change the local air density. However, since the air flow in the room is low-speed (maximum velocity on the order of, $u \sim 0.5$ m/s compared to speed of sound of around, $c \sim 343$ m/s), the Mach number (u/c), that represents the ratio of acoustic to convective time-scales, is small ($\ll 0.01$). Small Mach numbers mean that the convective time-scales are much larger than acoustic time-scales, and thus the compressibility effects are negligibly small. Under these conditions, the variable-density equations in the limit of zero-Mach number are valid and the pressure field at any point within the

domain and time can be split into a bulk thermodynamic pressure, P_0 , and the dynamic pressure p that appears in the momentum equation,

$$P(x, t) = P_0(t) + p(x, t). \quad (1)$$

The background thermodynamic pressure (P_0) for the operating room is assumed constant and equal to the atmospheric pressure, $P_0 = 1$ atm.. Accordingly, the density of the air (assumed as ideal gas) varies only with the local temperature field according to the equation of state as,

$$\rho = \frac{P_0 R_{\text{universal}} T}{M_{\text{air}}}, \quad (2)$$

361 where $R_{\text{universal}}$ is the universal gas constant, M_{air} is the molecular mass of the air, and T is the
 362 absolute temperature. The governing equations for large-eddy simulation of turbulent flows with
 363 variable density in the limit of zero Mach number are given below.

364 **3.2.1 Gas-phase equations**

365 The spatially filtered, Favre averaged, governing equations used for large-eddy simulation of particle-
 366 laden, turbulent air flow with heat transfer and buoyancy effects are given as,

$$\frac{\partial \bar{\rho}_g}{\partial t} + \frac{\partial \bar{\rho}_g \tilde{u}_j}{\partial x_j} = 0. \quad (3)$$

$$\frac{\partial \bar{\rho}_g \tilde{u}_i}{\partial t} + \frac{\partial \bar{\rho}_g \tilde{u}_i \tilde{u}_j}{\partial x_j} = -\frac{\partial \bar{p}}{\partial x_i} + \frac{\partial}{\partial x_j} (2\bar{\mu} \tilde{S}_{ij}) - \frac{\partial q_{ij}^r}{\partial x_j} + (\bar{\rho}_g - \rho_0) g_i, \quad (4)$$

$$\frac{\partial \bar{\rho}_g \tilde{h}}{\partial t} + \frac{\partial \bar{\rho}_g \tilde{h} \tilde{u}_j}{\partial x_j} = \frac{\partial}{\partial x_j} \left(\bar{\rho}_g \alpha_h \frac{\partial \tilde{h}}{\partial x_j} \right) - \frac{\partial q_{hj}^r}{\partial x_j}, \quad (5)$$

where

$$\tilde{S}_{ij} = \frac{1}{2} \left(\frac{\partial \tilde{u}_i}{\partial x_j} + \frac{\partial \tilde{u}_j}{\partial x_i} \right) - \frac{1}{3} \delta_{ij} \frac{\partial \tilde{u}_k}{\partial x_k}. \quad (6)$$

Here, $\bar{\rho}_g$ is the filtered density, \tilde{u}_i is the Favre averaged velocity field, \bar{p} is the filtered pressure, μ is the dynamic viscosity, $\alpha_h = k/\bar{\rho}_g C_p$, is the thermal diffusivity (k is the conductivity and C_p the specific heat at constant pressure), g_i is the gravitational acceleration, and \tilde{S}_{ij} is the filtered rate of

strain. In addition, the specific enthalpy, h , is given as,

$$h = \frac{T - T_0}{T_0}, \quad (7)$$

367 where T is the local temperature. Also, T_0 and ρ_0 are the temperature and density fields correspond-
368 ing to the air inlet conditions and pressure of P_0 .

The additional terms q_{ij}^r and q_{hj}^r in the momentum and the enthalpy equations, respectively, represent the subgrid-scale stress and energy flux and are modeled using the dynamic Smagorinsky model by [Moin et al. \(1991\)](#) as demonstrated by [Pierce & Moin \(1998a\)](#). The unclosed terms in Eqs. (4-5) are modeled using the gradient-diffusion hypothesis with eddy-viscosity/diffusivity,

$$q_{ij}^r = \overline{\rho_g}(\tilde{u}_i\tilde{u}_j - \widetilde{u_i u_j}) = 2\mu_t \tilde{S}_{ij} - \frac{1}{3}\overline{\rho_g}q^2 \delta_{ij}, \quad (8)$$

$$q_{hj}^r = \overline{\rho_g}(\tilde{h}\tilde{u}_j - \widetilde{h u_j}) = \overline{\rho_g}\alpha_t \frac{\partial \tilde{h}}{\partial x_j}, \quad (9)$$

where the eddy viscosity (μ_t) and eddy thermal diffusivity α_t are modeled as,

$$\mu_t = C_\mu \overline{\rho_g} \bar{\Delta}^2 \sqrt{\widetilde{S_{ij} S_{ij}}}, \quad (10)$$

$$\overline{\rho_g} \alpha_t = C_\alpha \overline{\rho_g} \bar{\Delta}^2 \sqrt{\widetilde{S_{ij} S_{ij}}}. \quad (11)$$

369 The coefficients C_μ , C_α are calculated dynamically at each time-step and for each grid point using
370 the dynamic procedure as outlined by [Germano et al. \(1991\)](#). For the unstructured grids, the filter
371 width $\bar{\Delta}$ is taken as $V_{cv}^{1/3}$ where V_{cv} is the volume of the grid element.

372 3.2.2 Equations for calculating the trajectories of individual squames

373 The human skin cells or squames typically are disc-shaped with a diameter ranging from 4–20 μm
374 and a thickness of 3–5 μm with density close to that of liquid water (1000 kg/m^3) ([Noble et al.,
375 1963; Noble, 1975; Snyder, 2009](#)). Although the squames shape is more disc-like, in the present
376 work they are considered as non-deformable, spherical in shape. A spherical shape is assumed as
377 the dynamics of the spherical particle is easier to calculate and also the lift and drag forces on small
378 particles of disc or spherical shape are not significantly different. The diameter of the spherical

379 particle is assumed to be 10 microns and matches an average settling velocity of a disc-shaped
 380 particle considering the mean flow normal and parallel to the disc (see Appendix A). Recent work
 381 using RANS model by Memarzadeh & Manning (2002); Memarzadeh (2003) also approximates the
 382 squames particles as spherical with a size of 10 microns.

An Eulerian-Lagrangian approach is used wherein individual squames trajectories will be tracked in a Lagrangian frame. The different forces on the particles will be calculated using standard closure laws. The effect of the particles on the fluid flow will be negligible owing to their small concentration and thus a one-way coupling approach is adopted, wherein the squame motion uses the fluid flow parameters (velocity) to compute the forces, however, the effect of squames on the fluid momentum is neglected (Elghobashi, 1994, 2006). In addition, since the volume fraction of the squames in an operating room is not very large ($<< 10^{-3}$), collisions amongst the squames are neglected. The squame particle motion equation is that of Maxey & Riley (1983),

$$\frac{d}{dt}(\mathbf{x}_p) = \mathbf{u}_p \quad (12)$$

$$m_p \frac{d}{dt}(\mathbf{u}_p) = \mathbf{F}_g + \mathbf{F}_d + \mathbf{F}_\ell + \mathbf{F}_{am} + \mathbf{F}_p + \mathbf{F}_H, \quad (13)$$

383 where \mathbf{x}_p is the particle (squames) centroid location, m_p is the mass of an individual particle, \mathbf{u}_p is
 384 the particle velocity, \mathbf{F}_g is the gravitational force, \mathbf{F}_d is the drag force, \mathbf{F}_ℓ is the lift force, \mathbf{F}_{am} is the
 385 added mass force, \mathbf{F}_p is the pressure force, and \mathbf{F}_H is the Basset history force.

386 The large ratio of particle density to air density, ρ_p/ρ_g , renders both the Basset history force
 387 and the added mass force negligible compared to the drag force. The ratio of the Saffman lift to
 388 the drag force is given by, $F_\ell/F_{drag} \sim \rho_g d_p^2 (du/dy)^{1/2}/\mu$, and is dependent on the shear rate and
 389 particle diameter. For particles with small diameter and low inertia this force can also be neglected
 390 in comparison to the drag force (Crowe *et al.*, 1996; Saffman, 1965). However, the lift force is in-
 391 corporated in our calculations to account for the saltation of the squame particles from the operating
 392 room floor. The gravity, drag and lift forces are given as,

$$\mathbf{F}_g = (\rho_p - \bar{\rho}_g) \mathcal{V}_p \mathbf{g}; \quad \mathbf{g} = -9.81 m/s^2 \quad (14)$$

$$\mathbf{F}_d = -\frac{1}{8}C_d \bar{\rho}_g \pi d_p^2 |\mathbf{u}_p - \tilde{\mathbf{u}}_{g,p}| (\mathbf{u}_p - \mathbf{u}_{g,b}); \quad C_d = \frac{24}{Re_p} (1 + 0.15 Re_p^{0.687}), \quad (15)$$

$$\mathbf{F}_\ell = -C_\ell m_p \frac{\bar{\rho}_g}{\rho_p} (\mathbf{u}_p - \tilde{\mathbf{u}}_{g,p}) \times (\nabla \times \tilde{\mathbf{u}}_g)_p; \quad C_\ell = \frac{1.61 \times 6}{\pi d_p} \sqrt{\frac{\mu}{\bar{\rho}_g} |(\nabla \times \tilde{\mathbf{u}}_g)_p|} \quad (16)$$

393 where the subscript p represents the squame particle, $\tilde{\mathbf{u}}_{g,p}$ represents the fluid velocity interpo-
 394 lated at the particle center location, \mathcal{V}_p is the particle volume, d_p is the particle diameter, $Re_p =$
 395 $\bar{\rho}_g |\mathbf{u}_p - \tilde{\mathbf{u}}_{g,p}| d_p / \mu$ is the particle Reynolds number, C_d is the drag coefficient, C_ℓ is the lift coeffi-
 396 cient.

397 The gas-phase velocity, $\tilde{\mathbf{u}}_g$, in the particle equations above, is computed at individual particle
 398 locations within a control volume using a generalized, tri-linear interpolation scheme for arbitrary
 399 shaped elements. Introducing higher order accurate interpolation is straight forward; however, it
 400 was found that tri-linear interpolation is sufficient to represent the gas-phase velocity field at particle
 401 locations. As mentioned earlier, in LES of particle-laden flows, the particles are presumed to be
 402 *subgrid*, and the particle-size is smaller than the filter-width used. The gas-phase velocity field re-
 403 quired in equations (12) and (13) is the total (unfiltered) velocity, however, only the filtered velocity
 404 field is computed in equations (4). The direct effect of the unresolved (subgrid) velocity fluctuations
 405 on particle trajectories depends on the particle relaxation time-scale, and the subgrid kinetic energy.
 406 [Pozorski & Apte \(2009\)](#) performed a systematic study of the direct effect of subgrid scale velocity on
 407 particle motion for forced isotropic turbulence. It was shown that, in poorly resolved regions, where
 408 the subgrid kinetic energy is more than 30%, the effect on particle motion is more pronounced. A
 409 stochastic model reconstructing the subgrid-scale velocity in a statistical sense was developed ([Po-](#)
 410 [zorski & Apte, 2009](#)). However, in well resolved regions, where the amount of energy in the subgrid
 411 scales is small, this direct effect was negligible. In the present work, the direct effect of subgrid
 412 scale velocity on the droplet motion is neglected. However, it should be noted that the particles *do*
 413 *feel* the subgrid scale stresses through the subgrid model that affects the resolved velocity field. For
 414 well-resolved LES of swirling, separated flows with the subgrid scale energy content much smaller
 415 than the resolved scales, the direct effect is shown to be small ([Apte *et al.*, 2003b, 2009](#)). This is
 416 the main advantage of LES as compared to RANS. In RANS, only the time-average mean velocity
 417 is available, and all scales of turbulence affecting the instantaneous fluctuations around the mean

418 must be modeled. Approximating the effect of turbulent fluctuations on the particle dispersion is
 419 thus necessary for RANS, whereas, it is implicitly accounted for in the LES.

420 Equations (12,13) are integrated using a fourth-order Runge-Kutta time-stepping algorithm. Af-
 421 ter obtaining the new particle positions, the particles are relocated, particles that cross interprocessor
 422 boundaries are duly transferred, boundary conditions on particles crossing boundaries are applied,
 423 source terms in the gas-phase equation are computed, and the computation is further advanced.
 424 Solving these Lagrangian equations thus requires addressing the following key issues: (i) efficient
 425 search and location of particles on an unstructured grid (ii) interpolation of gas-phase properties to
 426 the particle location for arbitrarily shaped control volumes (iii) inter-processor particle transfer. The
 427 details on efficiently locating the particles on unstructured grids, search algorithms for particles, and
 428 interpolation schemes can be found in the work by *Apte et al.* (2003b, 2009).

429 In addition, if the squames impact internal boundaries, a simple, perfectly elastic specular re-
 430 flection is assumed wherein the squames reverse the wall-normal velocity and preserve the wall-
 431 tangential velocity. If the squames impact the patient's knee or the inlet (suction port) of the 3M™
 432 Bair Hugger™ blower system, they are assumed to stick to the surface and are no longer advanced
 433 in the computations.

434 3.3 Computational grid

435 Use of high quality computational mesh is critical in LES for accurate prediction of the turbulent
 436 flow, but also having a stable numerical solution. However, to handle complex configurations, use
 437 of hybrid elements involving tetrahedrons, pyramids, hexagons and wedges, etc. is common in a
 438 typical computational grid. This helps with the grid generation surrounding complex features such
 439 as the operating table, the surgeons, the patient and the drape, for example. The transitions from
 440 one type of grid element to another; however, can lead to skewed elements. It is thus critical that
 441 the numerical algorithm be robust, stable and accurate at high Reynolds numbers on skewed or bad
 442 grid elements. A numerical algorithm developed for arbitrary shaped unstructured grids (*Mahesh*
 443 *et al.*, 2004; *Ham et al.*, 2003; *Ham & Iaccarino*, 2004; *Mahesh et al.*, 2006) that is based on kinetic
 444 energy conservation principles offers the much needed robustness and accuracy on such grids with-
 445 out resorting to explicit artificial dissipation. As discussed below, we use a research solver based on

446 such an algorithm.

447 For the present study, a computational mesh (figure 8) was generated using the CAD model
 448 described earlier to facilitate predictive large eddy simulations. The mesh was generated using both
 449 tetrahedral and hexahedral cells. The transition of mesh from tetrahedral cells to hexahedral cells
 450 was done using a combination of pyramid and wedge type cells. Care was taken to generate a
 451 computational grid that minimizes the grid skewness as much as possible. As shown below, in the
 452 regions away from the complex OR configuration involving the surgeons, the tables, the patient and
 453 the drape, a mostly hex-dominant mesh is used. As one approaches closer to the operating table, the
 454 computational grid is transitioned to a predominantly tetrahedra-based mesh (see figure 8b). The
 455 total mesh count for the computational domain is about 66 million.

456 Figure 9 shows the grid resolution near the air inlet cross-sections. The grid is appropriately re-
 457 fined to capture the shear layer generated by the inlet flow between the grilles. The mesh surrounding
 458 the OR table, patient, surgeons, side tables, the blower, and surgical lamps is predominantly tetra-
 459 hedral. The tetrahedral mesh was carefully refined to capture surface curvature. Extra refinement
 460 was performed near surfaces which were in close proximity to other surfaces. This enhanced mesh
 461 refinement is to ensure that the effect of surface shapes on the flow and particles going around them
 462 will be captured by the simulation (figure 10a,b.)

463 As is shown in the above figures, a high quality mesh was generated for the present LES inves-
 464 tigation. The minimum tetrahedral cell size (defined as cube root of the cell volume) used near all
 465 key regions such as drape, patient, operating bed, surgeons, etc. was around 1mm. Smallest grid
 466 spacing in proximity regions resolving the gaps between closely placed surfaces is 0.7mm. The
 467 coarsest tetrahedral cell size used away from the key regions is 2.5cm. As mentioned earlier in the
 468 report a fine mesh was used near the inlet regions to resolve the flow entering the operating room.
 469 A uniform hexahedral cell size of 2.5cm was used to resolve the air inlet grille faces with 20 cells
 470 along its width and 44 cells along its length. The gaps between the inlet grilles were resolved us-
 471 ing a finer mesh with each cell size of 0.63cm. To capture the inlet air flow structures properly,
 472 a refined uniform mesh of 0.38cm was used along the flow direction. Finally, a uniform cell size
 473 of 2.5cm was used to resolve each outlet grille with 28 cells along its width and 28 cells along its
 474 length. Various mesh metrics were checked to ensure that the quality of the generated mesh was
 475 good. Figure 11a shows histogram plot of cell skewness in the mesh. The average skewness was

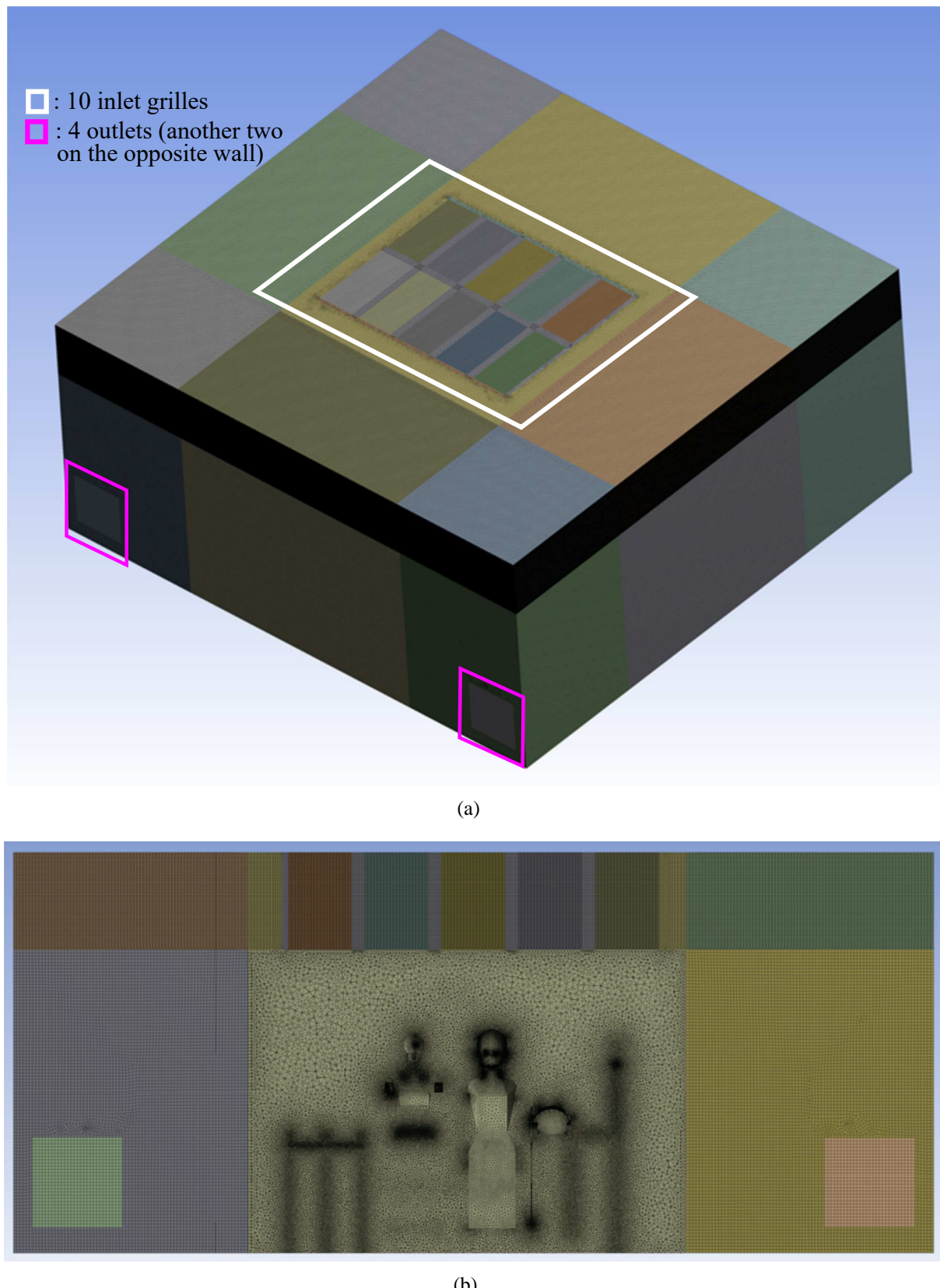


Figure 8: Computational mesh for the operating room model consisting of about 66M hybrid grid elements consisting of hexagons, tetrahedrons, pyramids and wedges: (a) the full 3D mesh, (b) cross-sectional slice showing hex-dominant mesh in the inlet and outlet regions and a tetrahedral mesh near the operating table.

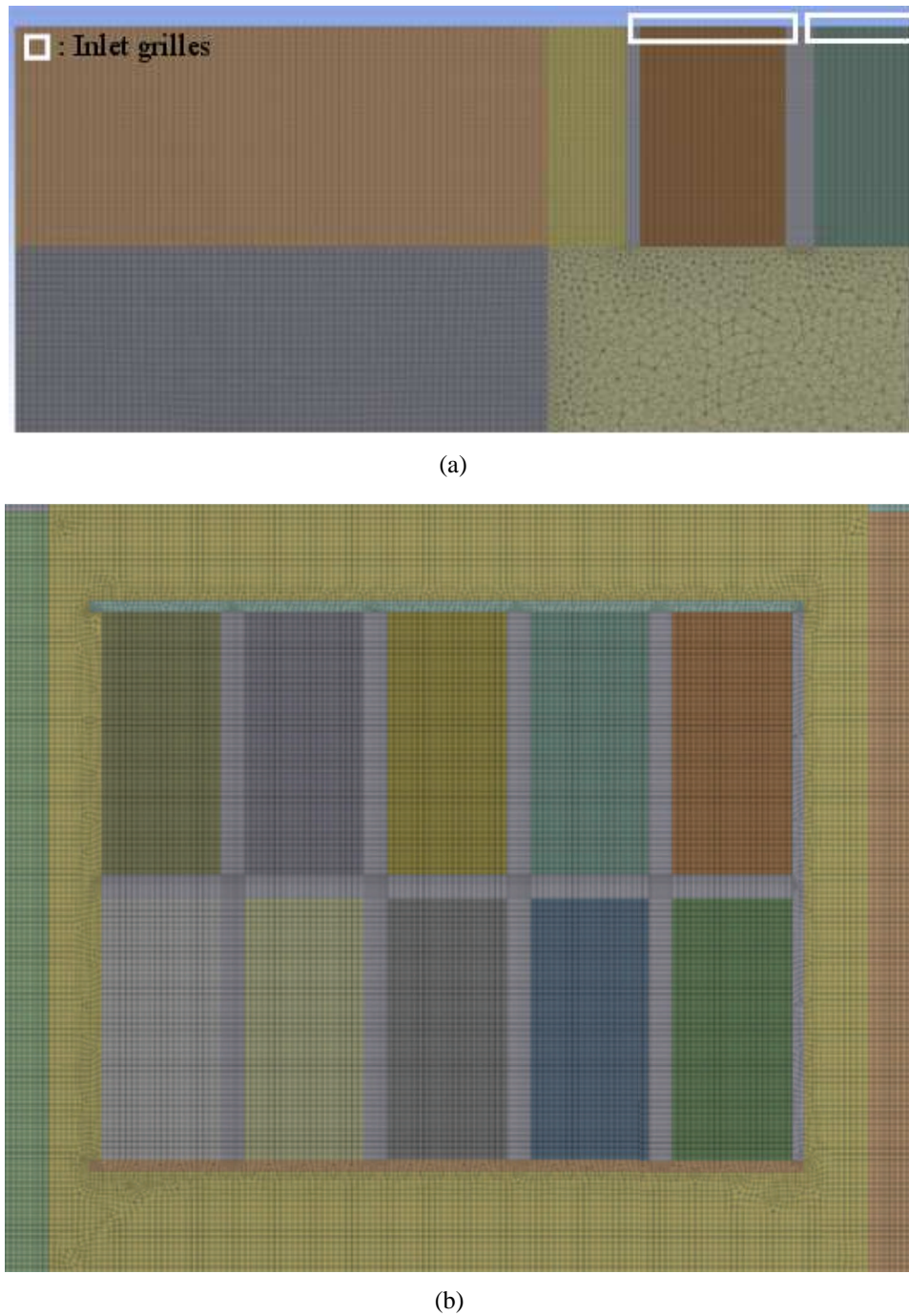
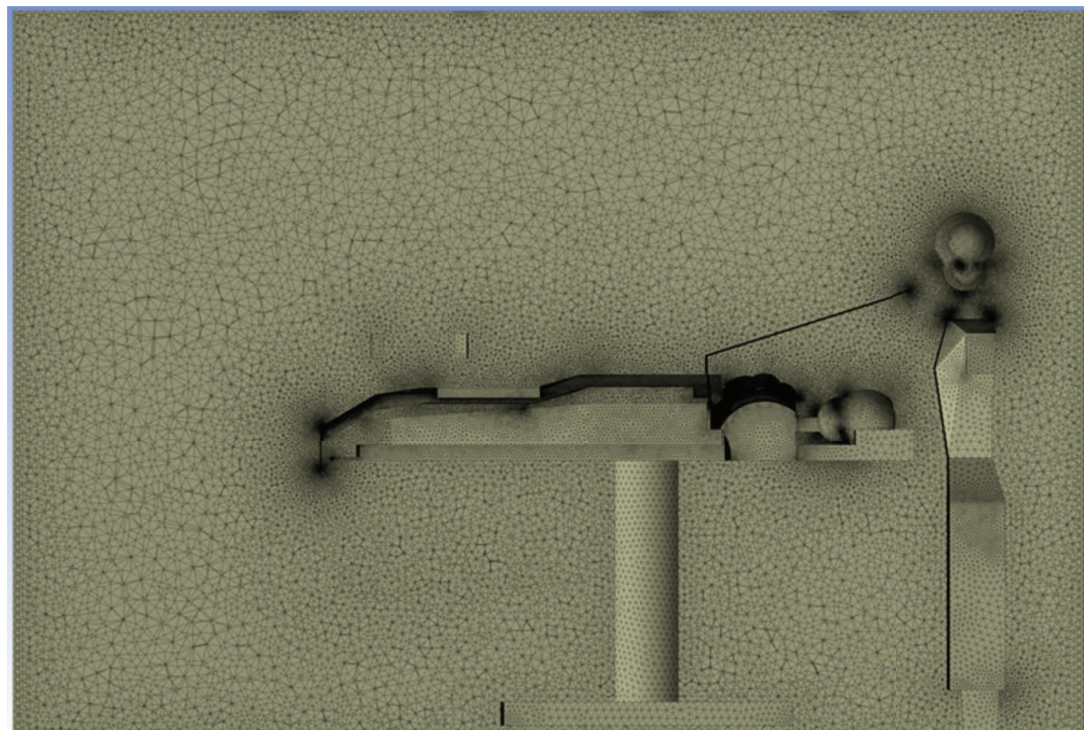
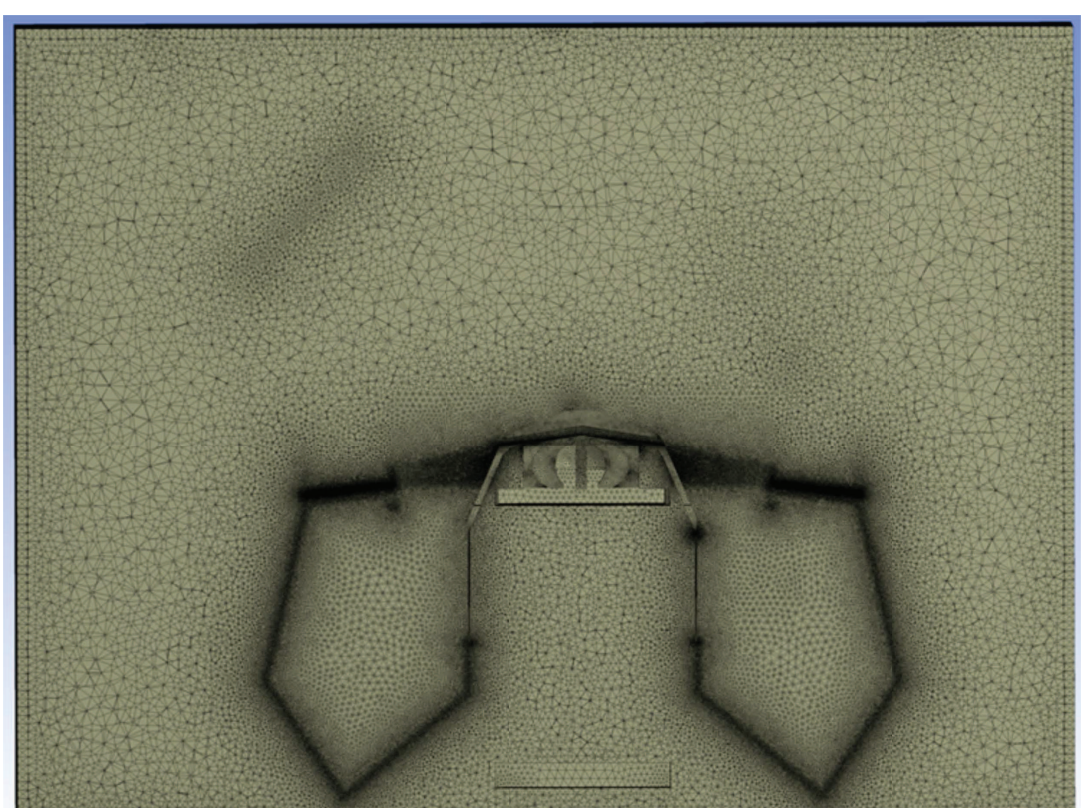


Figure 9: A cross section cut showing fine mesh near the ceiling of the room: (a) top view zoom-in, (b) top view showing all air inlet grilles.



(a)



(b)

Figure 10: Mesh refinement near curved surfaces and surfaces that are in close proximity to others: (a) side view showing the entire operating table, (b) side view showing drapes.

476 0.14 and with maximum skewness was 0.91. Only 0.018% of cells had total skewness greater than
 477 0.8 indicating the high quality of cells in the mesh. Another mesh metric that was checked was the
 478 aspect ratio of cells. The maximum aspect ratio was 16.2 and the average cell aspect ratio was 2.9,
 479 which indicate that a majority of cells in the mesh were mostly uniform (see figure 11b).

480 3.4 Boundary Conditions

481 This subsection provides details of all boundary conditions used in the calculation, starting with
 482 operating room (OR) air inlet conditions, heat sources, BH hot air blower inflow (suction) and
 483 outflow, and OR air outlet conditions.

484 3.4.1 Inlet boundary conditions

The dimensions of the operating room are shown in Table 1. As shown, there are 10 inlet grilles supplying air. The net supply air volumetric flow rate, \dot{V} , is $1.10436 \text{ m}^3/\text{s}$ ($0.39 \text{ ft}^3/\text{s}$). Using the inlet flow rates, the air changes per hour (ACH) of the room is calculated as follows,

$$\text{ACH} = \dot{V} \times 3600 / (LWH) = 24.45 \text{ per hour}, \quad (17)$$

485 where L , W and H are the room length (in x), width (in y) and height (in z) directions. The ACH is
 486 according to the ASHRAE handbook [Memarzadeh & Manning \(2002\)](#), which suggests the ACH to
 487 be about 25 per hour for an operating room with recirculating air system.

The inlet boundary conditions are imposed at the 10 grilles on the ceiling of the operating room to model the inlet part of the forced ventilation system. The average inlet velocity, \bar{U}_{in} , is found to be 0.1933 m/s based on,

$$\bar{U}_{in} = \dot{V} / (10 \times A_{grill}), \quad (18)$$

488 where A_{grill} is the area of the cross-section ($1.12 \times 0.51 = 0.5712 \text{ m}^2$) and $\dot{V} = 1.1044 \text{ m}^3/\text{s}$ ($39 \text{ ft}^3/\text{s}$)
 489 is the net inlet volumetric flow rate. The air temperature of the inlet flow, T_{in} , is set to 59°F (15°C).

490 Based on Reynolds number for the inlet grilles, $Re_{in} = 9226.54$ (Table 1), the inlet flow is turbulent.
 491 In order to have completely predictive numerical simulation and to minimize the effect of
 492 boundary conditions, it is necessary to impose a proper, fully developed turbulent flow field at the in-

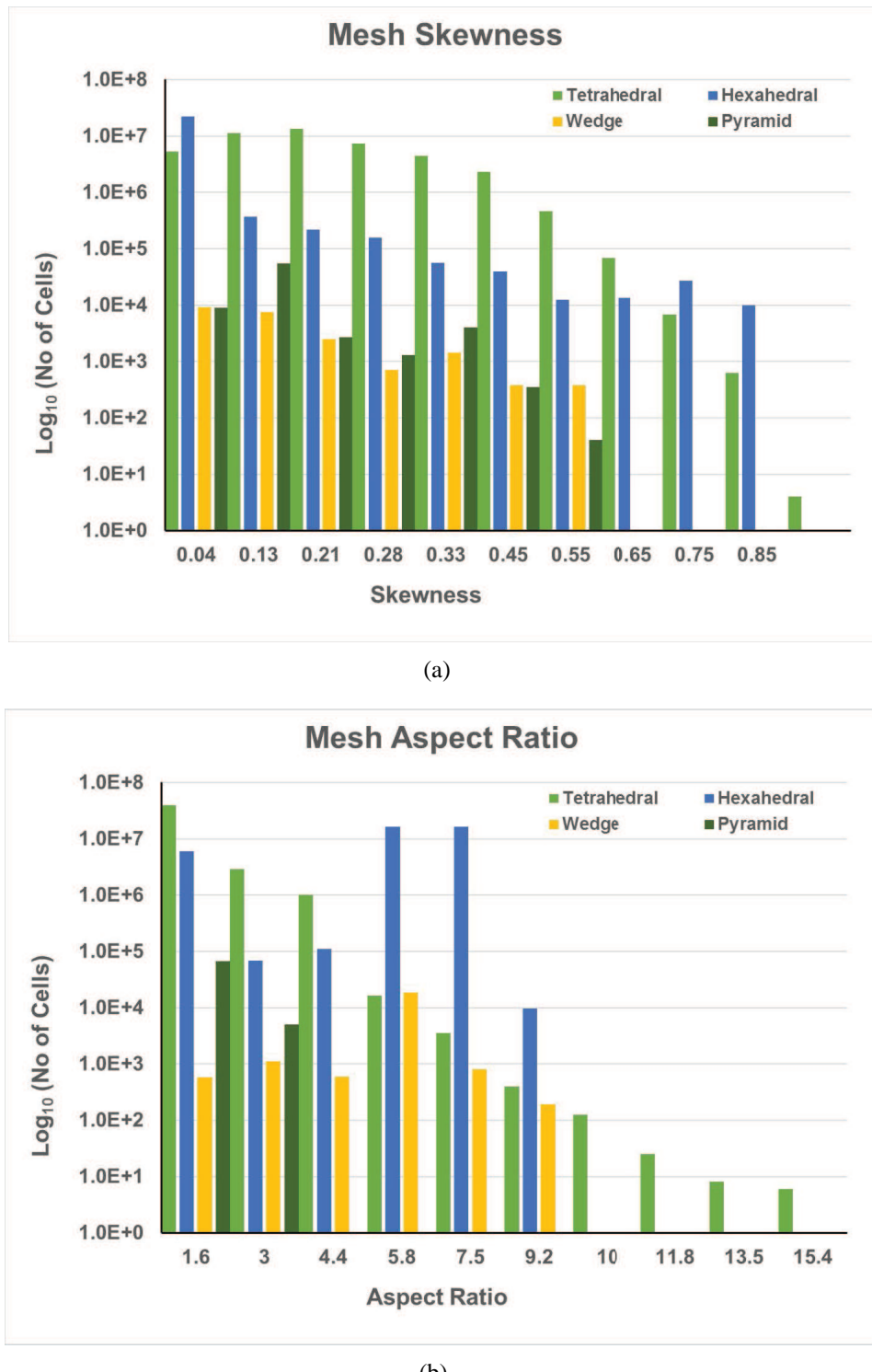


Figure 11: Statistics histograms of the quality of mesh used in the computation: (a) skewness, (b) aspect ratio.

Table 1: Operating room characteristics

Parameter	Value
Room dimensions [m], L, W, H	$7.315 \times 7.00 \times 3.175$
Supply air flow rate [m^3/s], \dot{V}	1.10436
ACH [1/hr]	24.45
Room air temperature [$^\circ\text{C}$]	15
Inlet air density [kg/m^3], ρ_{in}	1.225
Supply air temperature [$^\circ\text{C}$]	15
Room air pressure [Pa]	1.0131×10^5
Grille dimensions [m]	1.12×0.51
Grille Area [m^2]	0.5712
Grille hydraulic diameter [m], D_h	0.7
Mean inlet velocity [m/s], \bar{U}_{in}	0.1933
Inlet Reynolds number, $Re_{in} = \frac{\rho_{in}\bar{U}_{in}D_h}{\mu}$	9226.54

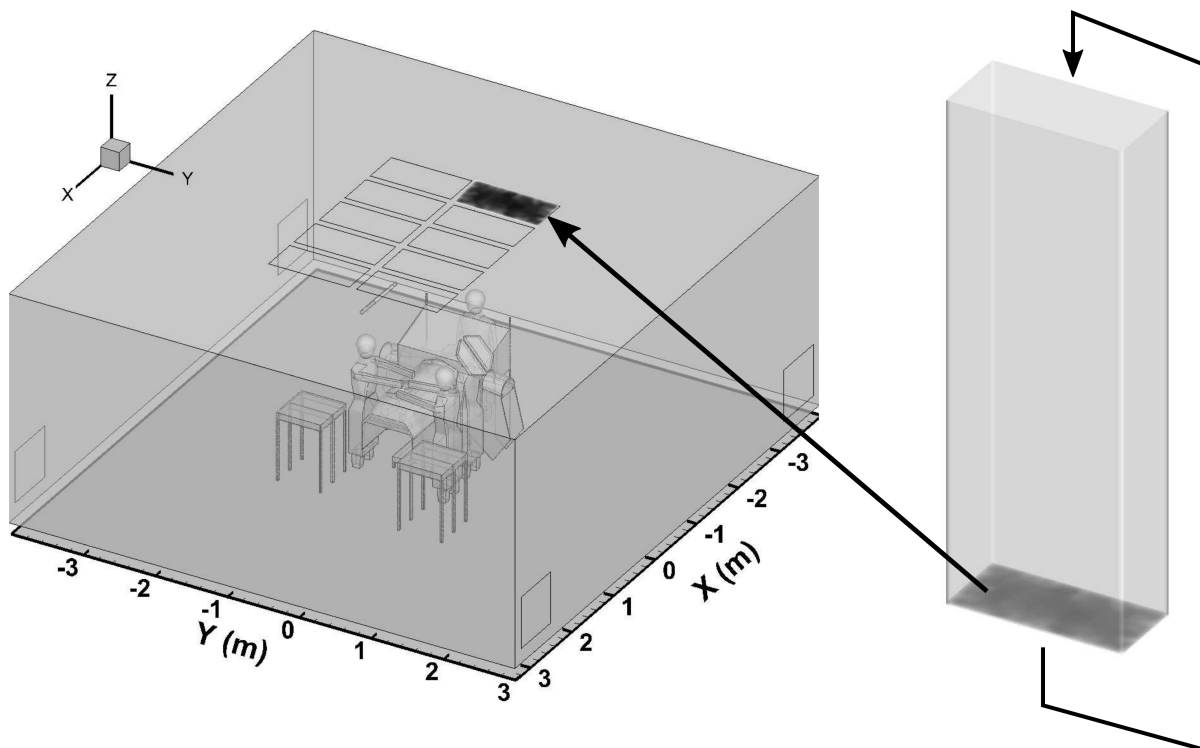


Figure 12: Schematic of the periodic duct used to generate inlet flow data.

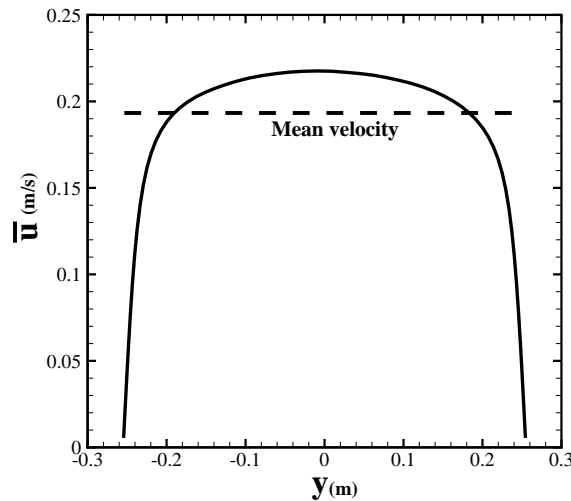


Figure 13: Mean velocity profile generated by a periodic duct flow for the inlet grilles.

493 let. Thus, a periodic turbulent duct flow was computed (figure 12) to produce a target mean flow rate
 494 equal to that prescribed ($\dot{V} = 1.10436 \text{ m}^3/\text{s}$) using a body force technique of [Pierce & Moin \(1998b\)](#).
 495 This also generates turbulence fluctuations at the inlet plane that satisfy the continuity equation. The
 496 cross-sectional area of the periodic duct used is the same as that of each grille ($1.12\text{m} \times 0.51\text{m}$), and
 497 the length is about 4.5 times the hydraulic diameter of the cross-section. The velocity field data at
 498 the inlet cross-section was recorded in time series for almost 400 seconds of physical time. Figure 13
 499 shows the time-averaged velocity field in the center plane of the duct obtained from the periodic duct
 500 simulation. The turbulence intensity ($I = \sqrt{\frac{1}{3}(u_{rms}^2 + v_{rms}^2 + w_{rms}^2)/\bar{U}_{in}}$) at the inlet cross-section is
 501 5-6% of the mean inlet velocity (\bar{U}_{in}), and is in agreement with the experimental measurements con-
 502 ducted by [McNeill et al. \(2012, 2013\)](#). Here, u_{rms} , v_{rms} and w_{rms} are the root-mean square velocity
 503 components in the x , y and z directions, respectively.

504 3.4.2 Hot air blower and other heat sources

A 3M™ Bair Hugger™ 750 blower draws air from the floor of the operating room, heats it and blows it into the blanket (3M™ Bair Hugger™ Model 522) that covers the torso region of the patient. The blanket is covered with a plastic drape. The maximum flow rate of the blower is $\dot{V}_{blower} = 0.021 \text{ m}^3/\text{s}$. The hot air moves along the surface of the drape that faces the patient and then it is discharged into the room along the drape edges. In the present calculation, the bottom surface (facing the floor) of the 3M™ Bair Hugger™ blower is considered as a suction surface with

surface area ($A_{extraction} = 0.03796\text{m}^2$). A Dirichlet boundary condition is applied at this surface that prescribes the extraction velocity $\bar{U}_{extraction}$ as

$$\bar{U}_{extraction} = \frac{\dot{V}_{blower}}{A_{extraction}}, \quad (19)$$

giving an extraction velocity of 0.5532m/s . To model the hot air discharged along the edges of the drape. The total area of this edge of the drape is measured to be $A_{drape} = 0.07794\text{m}^2$. A Dirichlet boundary condition is applied such that the air is injected into the room perpendicular to the edges of the drape with velocity, \bar{U}_{drape} , calculated as,

$$\bar{U}_{drape} = \frac{\dot{V}_{blower}}{A_{drape}}, \quad (20)$$

giving an average injection velocity along the drape edge as 0.2694 m/s . The temperature of the hot air at the BH blower outlet is prescribed equal to 109°F (42.77°C) and the temperature of the air leaving the drape edge is set equal to 106°F (41.11°C) according to 3M video at: <https://www.youtube.com/watch?v=QhzeInWIJ54>. The flow rates at the inlet grilles and for the blower are summarized in Table 3.4.2.

Other heat sources in the surgical room are mainly the surgeons, patient, surgical lamps, and exposed surface of the patient's knee. These heat sources can cause warming of the air in contact with the surfaces and result in a rising thermal plume. For these surfaces, a Dirichlet condition was used for temperature based on the experimentally measured values. In their work, [McNeill et al. \(2012\)](#) conducted detailed measurements of detailed surface temperatures that may lead to buoyant plumes specifically to be used in CFD calculations. The values are summarized in Table 3.4.2, among which, the temperatures of surgeons and patient's heads as well as the surgical lamps are based on the work of [McNeill et al. \(2012\)](#) and the rest are from the *3M video*. For all other other solid surfaces, a no heat flux Neumann condition was specified, $\frac{\partial T}{\partial n} = 0$.

3.5 Numerical solution method

The computational approach is based on a co-located, finite-volume, energy-conserving numerical scheme on unstructured grids ([Moin & Apte, 2006](#); [Mahesh et al., 2006](#)) and solves the variable

Table 2: Flow and temperature conditions

Parameter	Value
Inlet volume flow rate \dot{V} , [m ³ /s]	1.1044
Temperature of inlet grille air, [°C]	15
Mean inlet velocity [m/s], \bar{U}_{in}	0.1933
BH blower volume flow rate \dot{V}_{blower} , [m ³ /s]	0.021
Temperature of hot air leaving the drape edge, [°C]	41.11
Heads of the surgeons and patient, [°C]	31.44
The patient's knee , [°C]	37.78
Two surgical lamps, [°C]	93.92

526 density gas-phase flow equations in the limit of zero-Mach number. In this co-located scheme, the
 527 velocity and pressure fields are stored and solved at the centroids of the control volumes. Numerical
 528 solution of the governing equations of the continuum fluid phase and particle phase (squames) are
 529 staggered in time to maintain time-centered, second-order advection of the fluid equations. Denot-
 530 ing the time level by a superscript index, the velocities are located at time level t^n and t^{n+1} , and
 531 pressure, density, viscosity, and the scalar fields at time levels $t^{n+3/2}$ and $t^{n+1/2}$. Sqaumes position
 532 and velocity are advanced explicitly from $t^{n+1/2}$ to $t^{n+3/2}$ using fluid quantities at time-centered
 533 position of t^{n+1} .

534 3.5.1 Advancing the Lagrangian squames equations

535 The squames (particles) equations are advanced using a fourth-order Runge-Kutta scheme. Owing
 536 to the disparities in the flow field time-scale (τ_f) and the squames relaxation time (τ_p) sub-cycling
 537 of the squames equations may become necessary. Accordingly, the time-step for squames equation
 538 advancement (Δt_p) is chosen as the minimum of τ_p and the time-step for the flow solver (Δt). For
 539 the present simulations, the squames relaxation time, τ_p , based on the drag force, was found to be
 540 always larger than the time-step, Δt , used for solving the fluid flow equations in LES. Thus, the
 541 temporal evolution of the squames was well resolved by the flow time step, and subcycling of the
 542 particle equations was not necessary.

543 After obtaining their new positions, the squames are relocated, and the squames that cross inter-
 544 processor boundaries are duly transferred. Boundary conditions for squames crossing boundaries are
 545 applied and the computation is further advanced. Solving these Lagrangian equations thus requires

546 addressing the following key issues: (i) efficient search for locations of squames on an unstructured
 547 grid, (ii) interpolation of gas-phase properties to the squames location for arbitrarily shaped control
 548 volumes, (iii) inter-processor transfer of the squames.

549 Locating the squames particles in a generalized-coordinate structured code is straightforward
 550 since the physical coordinates can be transformed into a uniform computational space. This is not
 551 the case for unstructured grids used in the present simulations (*Apte et al., 2003b,a, 2009*). The ap-
 552 proach used here, projects the squames location onto the faces of the control volume and compares
 553 these vectors with outward face-normals for all faces. If the particle lies within the cell, the pro-
 554 jected vectors point the same way as the outward face-normals. This technique is found to be very
 555 accurate even for highly skewed elements. A search algorithm is then required to efficiently select
 556 the control volume to which the criterion should be applied. An efficient technique termed as ‘the
 557 known vicinity algorithm’ was used to identify the control volume number in which the particle lies.
 558 Given the previous particle location, the known-vicinity algorithm identifies neighboring grid cells
 559 by traversing the direction the particle has moved. In LES, the time steps used are typically small
 560 in order to resolve the temporal scales of the fluid motion. Knowing the initial and final location of
 561 the particle, this algorithm searches in the direction of the particle motion until it is relocated. The
 562 neighbor-to-neighbor search is extremely efficient if the particle is located within 5-10 attempts,
 563 which is usually the case for 98% of the squames in the present simulation. Once this cell is iden-
 564 tified, the fluid parameters are interpolated to the particle location using a generalized, tri-linear
 565 interpolation scheme for arbitrary shaped elements. Introducing higher order accurate interpolation
 566 is straight forward; however, it was found that tri-linear interpolation is sufficient to represent the
 567 gas-phase velocity field at particle locations. In the present case, particles are distributed over sev-
 568 eral processors used in the computation, and the load-imbalance was not significant. Details of the
 569 algorithm can be found in *Apte et al. (2003b, 2009)*. The overall increase in computational cost due
 570 to addition of about 3 million particles was about 25% per time-step.

571 3.5.2 Advancing the Eulerian fluid flow equations

572 The scalar field (enthalpy or non-dimensional temperature; equation 5) is advanced using the old
 573 time-level velocity field. A second-order WENO scheme is used for scalar advective terms and
 574 centered differencing for the diffusive terms. All terms, except the source terms due to buoyancy

575 effect, are treated implicitly using Crank-Nicholson for temporal discretization. Once the scalar field
 576 is computed, the density and temperature fields are obtained from constitutive relations (equation 7)
 577 and the ideal gas law (equation 2). The cell-centered velocities are advanced in a predictor step such
 578 that the kinetic energy is conserved. The predicted velocities are interpolated to the faces and then
 579 projected. Projection yields the pressure at the cell-centers, and its gradient is used to correct the
 580 cell and face-normal velocities. The steps involved in solving the projection-correction approach for
 581 velocity field are briefly described below, Details of this algorithm may be found in **Moin & Apte**
 582 (**2006**); **Mahesh et al.** (**2006**); **Apte et al.** (**2008b**).

- Advance the fluid momentum equations using the fractional step algorithm. The density field is available at intermediate time level is obtained from arithmetic average at the two time steps $t^{n+3/2}$ and $t^{n+1/2}$.

$$\frac{\rho u_i^* - \rho u_i^n}{\Delta t} + \frac{1}{2V_{cv}} \sum_{\text{faces of } cv} [u_{i,f}^n + u_{i,f}^*] g_N^{n+1/2} A_f = \quad (21)$$

$$\frac{1}{2V_{cv}} \sum_{\text{faces of } cv} \mu_f \left(\frac{\partial u_{i,f}^*}{\partial x_j} + \frac{\partial u_{i,f}^n}{\partial x_j} \right) A_f + (\rho - \rho_0) g_i$$

583 where f represents the face values, N the face-normal component, $g_N = \rho u_N$, and A_f is the
 584 face area. The superscript '*' represents the predicted velocity field, and $g_N^{n+1/2} = 0.5(g_N^n +$
 585 $g_N^{n+1})$.

- Interpolate the velocity fields to the faces of the control volumes and solve the Poisson equation for pressure:

$$\nabla^2(p\Delta t) = \frac{1}{V_{cv}} \sum_{\text{faces of } cv} \rho_f u_{i,f}^* A_f + \frac{\rho^{n+3/2} - \rho^{n+1/2}}{\Delta t} \quad (22)$$

- Reconstruct the pressure gradient, compute new face-based velocities, and update the cv-velocities using the least-squares interpolation used by **Mahesh et al.** (**2004**); **Ham et al.** (**2003**); **Mahesh et al.** (**2006**),

$$\frac{\rho (u_i^{n+1} - u_i^*)}{\Delta t} = -\frac{\delta p}{\delta x_i}. \quad (23)$$

586 **4 Results**

587 The numerical simulation was initiated with stagnant air (zero velocity) in the operating room and
 588 proper boundary conditions. A simulation was carried out with the blower off and all surfaces at
 589 room temperature for about 67s of physical time, which corresponds to about 4 flow through times
 590 based on the average inlet air velocity and the height of the room. After the initial transients, the
 591 thermal boundary conditions were applied at the surgeons heads, the patient's knee, the surgical
 592 lights. A calculation was performed for another 54s to establish a stationary flow with the thermal
 593 plumes created by the surfaces with higher-than-ambient temperatures. At this time, calculation
 594 of statistics for time-averaged mean velocity field and turbulence intensity were initiated and also 3
 595 million squame particles were placed at the floor in three different regions surrounding the operating
 596 table as described below. With the blower-off the time-step used in the calculation was $\Delta t = 6 \times$
 597 10^{-5} s giving a CFL number of about 0.75. This time step was able to resolve the important time-
 598 scales of turbulence and particle motion accurately. The flow statistics were collected for a total
 599 of 80s after a stationary flow field was established and the squames trajectories were calculated for
 600 about 21s.

601 After the above calculation was completed, the remaining squames particles in the computational
 602 domain were removed, and the blower was turned on. With the blower discharging a hot air at
 603 higher speeds, the time-step was reduced by a factor of 2.5 to $\Delta t = 2.4 \times 10^{-5}$ s maintaining the
 604 CFL number about 0.6. The reduction in time step is related to both the explicit treatment of the
 605 gravitational source term in the momentum equation as well as increased velocity at the blower
 606 discharge location. A calculation was performed for about 30s to obtain a developed plume from
 607 the hot air discharged by the blower. Flow statistics and the initial location of 3 million squames
 608 particles were initiated. With the blower-on, the flow statistics were collected for about 37s and
 609 particle trajectories were calculated for about 30s.

610 All calculations were performed on a parallel computer and used 1600 processors. The com-
 611 putational domain was decomposed such that each processor contains roughly the same number of
 612 control volumes. The overall calculation (including initial transient, the case with blower-off and
 613 the case with blower-on including particle trajectories for both cases) took about 2M CPU-hrs. For
 614 the case of blower-off, about 20s of physical time would cost roughly 100,000 CPU-hours, whereas

615 the same calculation with blower-on would cost roughly 220,000 CPU-hours. For each case, tracking
 616 3 million trajectories of squames would add about 20-30% additional computing cost. This is
 617 because, initially the 3 million squames are clustered in a small region near the floor causing load
 618 imbalance as the particles were present on only a few processor domains. The flow statistics and
 619 particle trajectories are discussed below.

620 4.1 Flow characteristics

621 Figures 14a and 14b show the locations of two slices through the three-dimensional computational
 622 domain at $x = -0.88\text{m}$ and $y = -0.162\text{m}$ for which the mean velocity magnitude, turbulence inten-
 623 sity, and instantaneous temperature contours are plotted. The $x = -0.88\text{m}$ slice shows a planar cut
 624 that includes the surgical lamp and the operating table (OT). The $y = -0.162\text{m}$ slice shows a side
 625 view and contains 2 medical staff, a side table, the surgical lamp, and part of the inverted U-shaped
 626 drape. For these two slices, the flow characteristics with blower-off and blower-on are compared.

627 Figures 15, 16, and 17 show the contours of mean velocity magnitude, turbulence intensity, and
 628 instantaneous temperature, respectively, for the two cases of blower-off and blower-on. For the case
 629 of blower-off, figure 15a shows that the ventilation air from the ceiling inlet grilles moves down-
 630 wards, gets deflected by the surgical lights and the table, impinges on the floor farther away from
 631 the table, and finally exits through the outlet grilles. Large recirculation regions are created on both
 632 sides of the table. The flow is not symmetric owing to asymmetries in the configuration itself. In
 633 comparison, with the blower turned on, the flow underneath and around the table is considerably
 634 modified as can be seen from the large velocity magnitudes under the table (figure 15b). The recir-
 635 culation region is also disrupted by the rising air from the hot blower discharge. This difference is
 636 clearly visible from the turbulence intensity contours shown in figure 16a,b. With the blower-off,
 637 the maximum turbulence intensity level is about 30% in the high shear regions between the inlet air
 638 streams, as well as near the warm surgical lights due to the buoyant plume. With the blower-on, the
 639 turbulence intensity level is as high as 60% in regions affected by the rising thermal plumes from
 640 the blower hot air. The instantaneous temperature contours shown in figure 17a,b confirm that the
 641 increased turbulence level is mainly because of the thermal plumes from the hot blower air as can
 642 be seen by the high temperature regions under the OT.

643 Figures 18, 19, and 20 show the contours of mean velocity magnitude, turbulence intensity, and

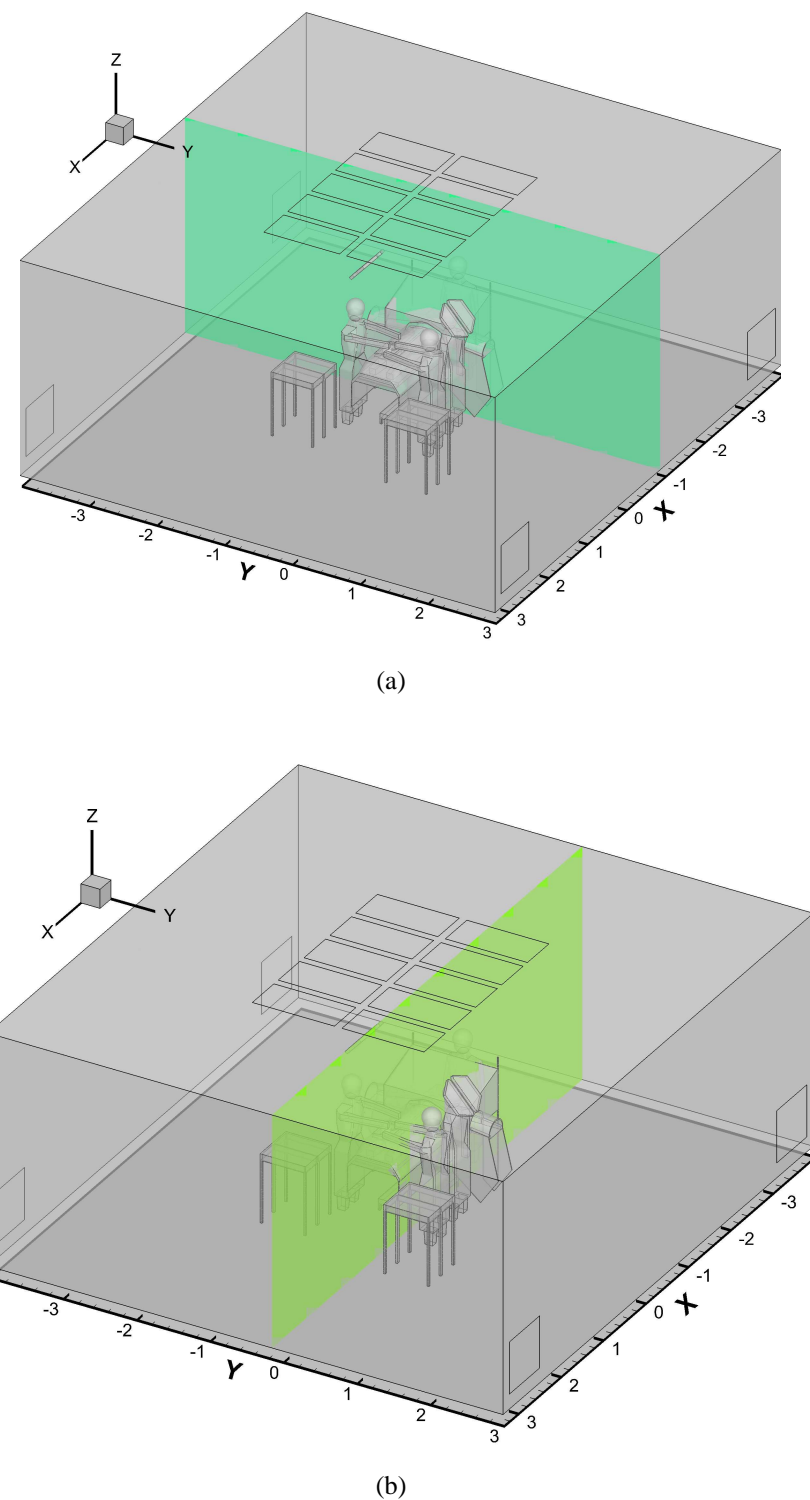
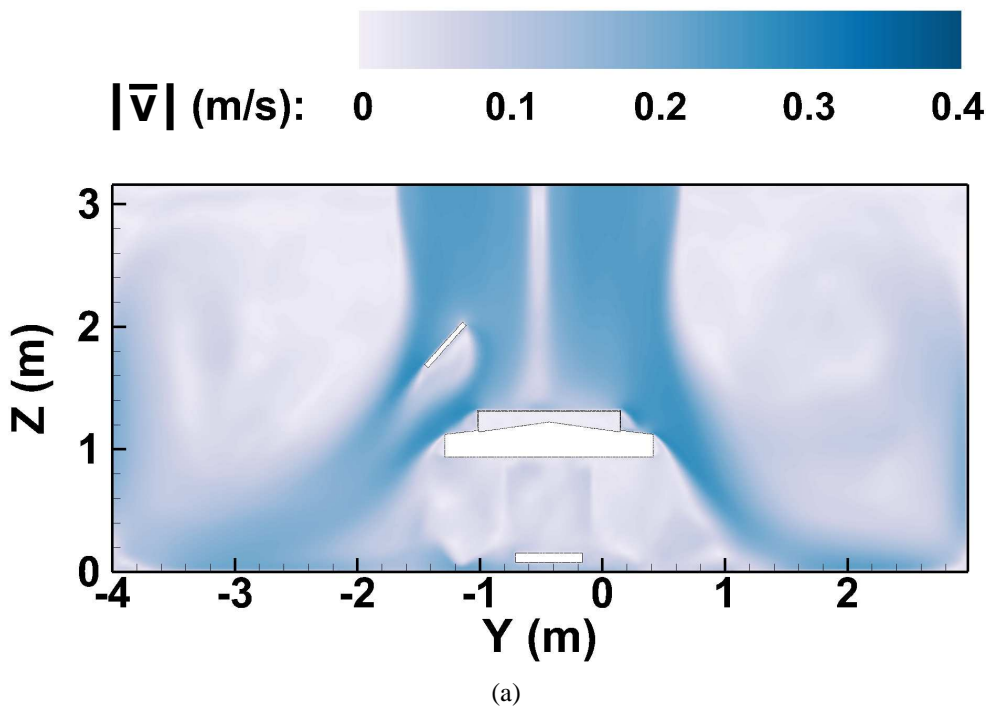
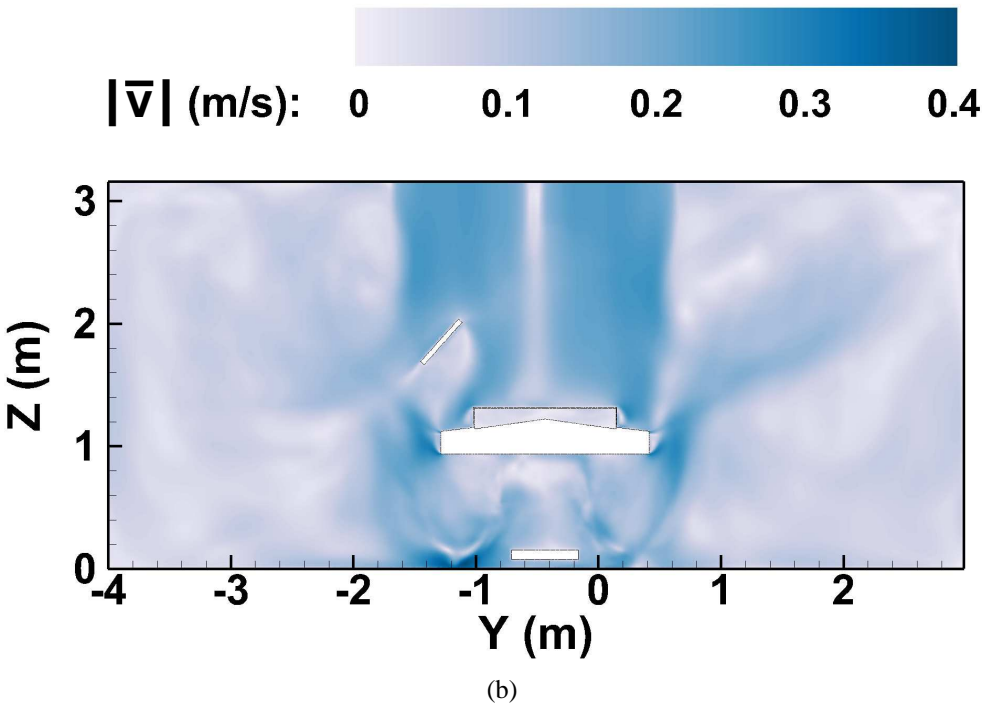


Figure 14: Locations of the planes for which contour plots of mean velocity magnitude, turbulence intensity and instantaneous temperature are presented to compare the effect of the blower discharge on the flowfield: (a) $x = -0.88\text{m}$ (b) $y = -0.162\text{m}$.



(a)



(b)

Figure 15: Contours of the mean velocity magnitude at $x = -0.88\text{m}$ (a) with blower-off and (b) with blower-on. The time average is taken over a physical time of 80s (no blower) and 37s (with blower) after establishing a stationary state.

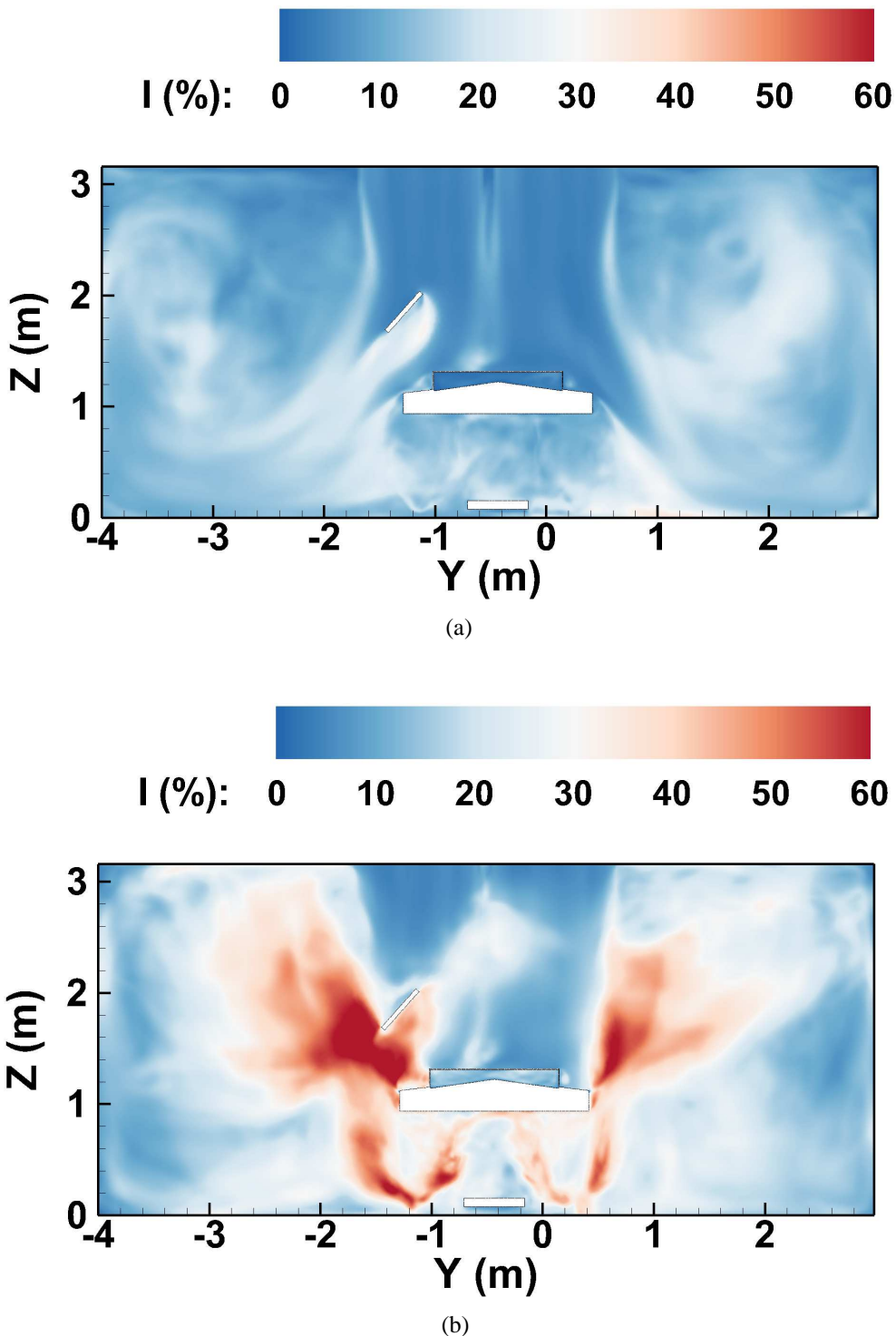


Figure 16: The turbulence intensity contours at $x = -0.88\text{m}$ (a) with blower-off and (b) with blower-on. The time average is taken over a physical time of 80s (no blower) and 37s (with blower) after establishing a stationary state.

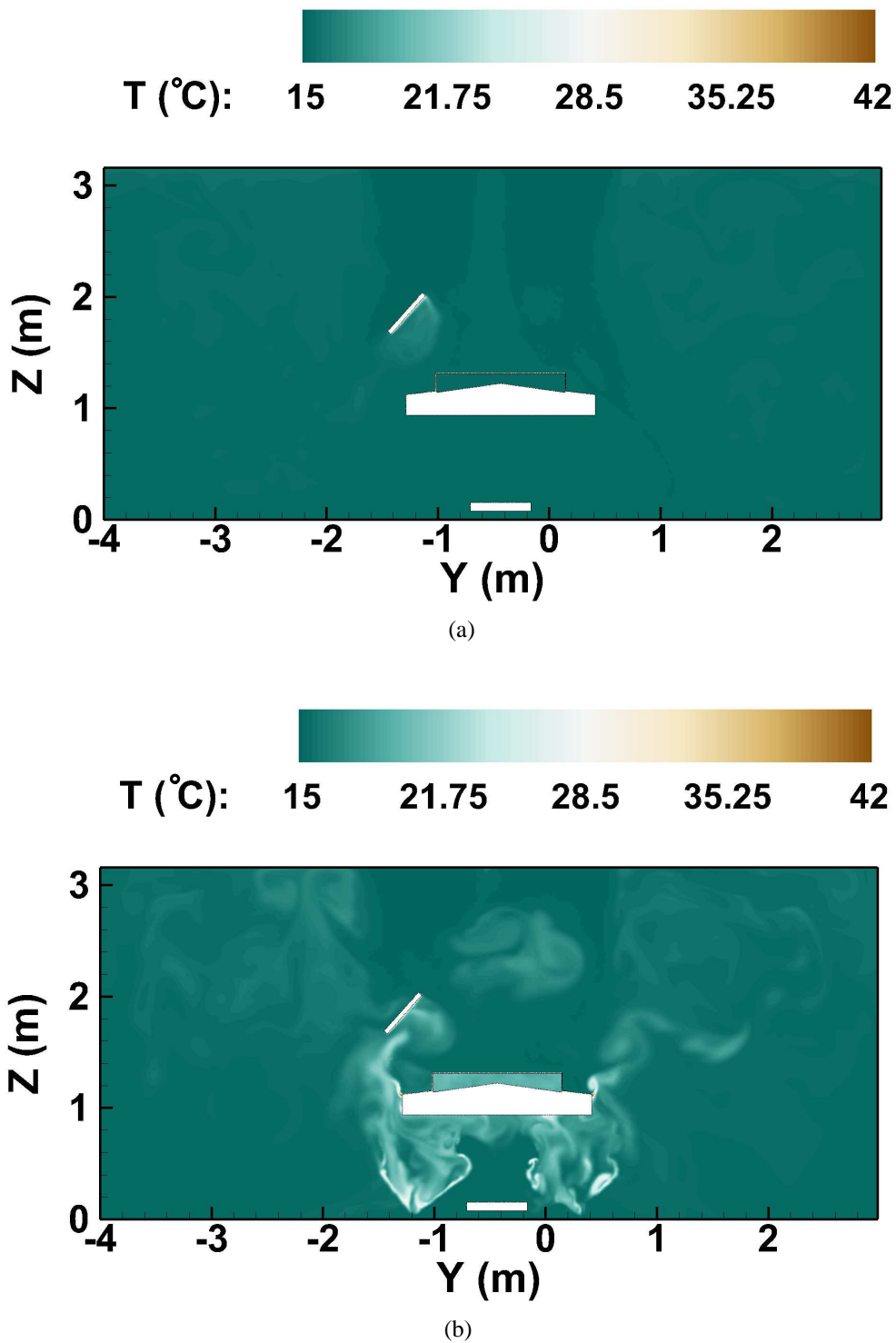


Figure 17: The instantaneous temperature contours at $x = -0.88\text{m}$ (a) with blower-off and (b) with blower-on. These snapshots are at about 35s after a stationary flow field was obtained and calculation for flow statistics was initiated.

644 instantaneous temperature, respectively, for the cases of blower-off and blower-on at $y = -0.162\text{m}$.
 645 Similar trends as described before are observed. The hot blower air and the rising thermal plumes
 646 disrupt the downward ventilation air flow. The high temperatures and turbulence intensity under the
 647 inverted U-shaped drape are clearly visible. The flow is also highly asymmetric with the blower
 648 turned on owing to the orientation and location of the drape. It is also seen from figure 20b that
 649 the rising thermal plumes may reach the ceiling in some regions. With the blower off, however, the
 650 plumes from warm surfaces of surgical lights, surgeons heads, and patient's knee are weak and are
 651 not significant enough to disrupt the downward ventilation air flow.

652 4.2 Dispersion of squames

653 This section provides details of the initial locations of the squames, their trajectories, and statistics
 654 of sampling the particles in regions of interest with high potential of reaching the surgical site.

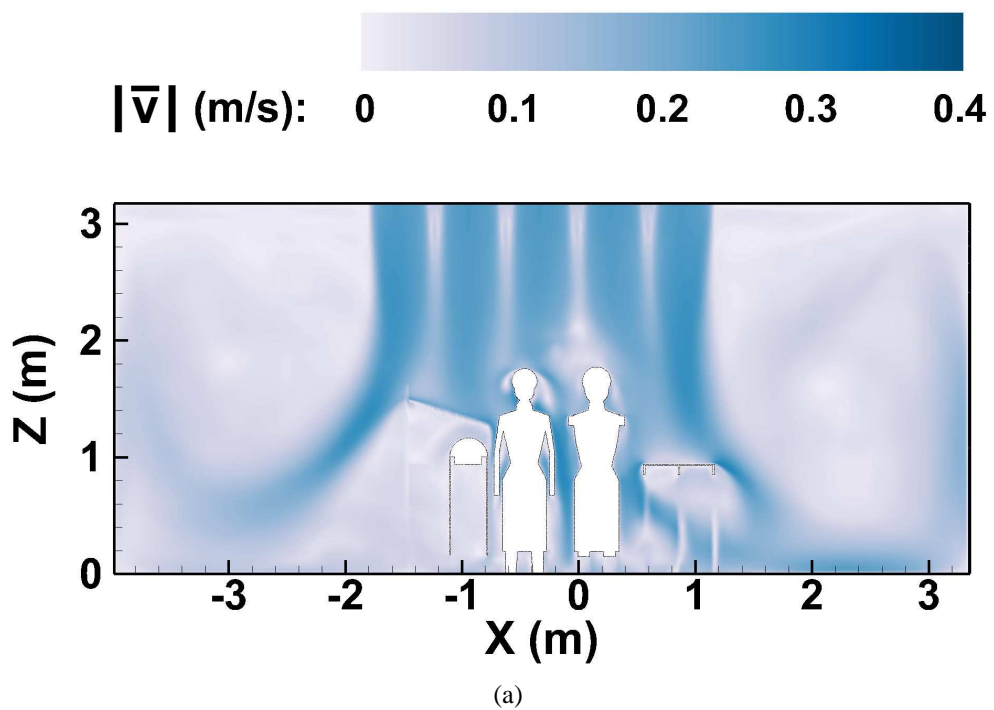
655 4.2.1 Initial locations of squames

656 In order to provide a worst-case (or least probable) scenario for the squames to be carried to the
 657 surgical site by the air convection, all 3 million squames were initially placed on the floor and
 658 randomly distributed in a small region surrounding the operating table within a height of about 1 cm
 659 above the floor of the OR. If these squames are lifted by the turbulent air and moved to the surgical
 660 site, other effects such as motion of medical equipment and staff, additional squames shed from the
 661 heads and faces of medical staff, surgical garments, etc. will have an even higher probability to
 662 reach the surgical site.

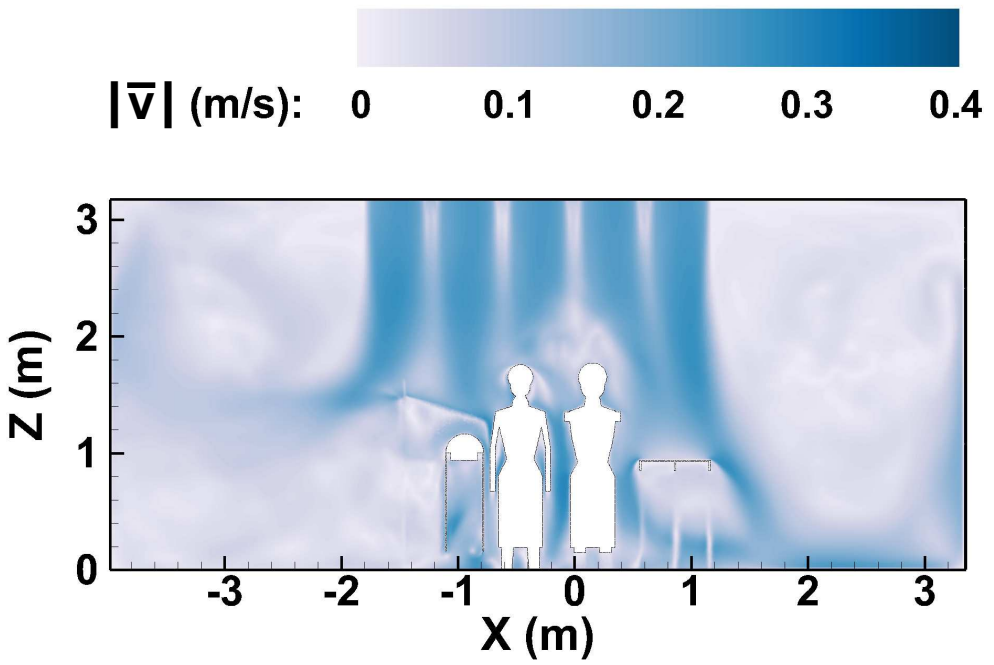
Table 3: Coordinates of color-coded regions for initial positions of squames as shown in figure 21.

Color-coded initial position	$(x, y, z)_{\min} [\text{m}]$	$(x, y, z)_{\max} [\text{m}]$
Red	(-1.40, -0.025, 0.0)	(0.70, 0.40, 0.01)
Green	(-1.80, -1.35, 0.0)	(-1.4, 0.4, 0.01)
Yellow	(-1.40, -1.35, 0.0)	(0.70, -0.855, 0.01)

663 Three million particles with a diameter of 10 micron are placed within a 1 cm thick layer above
 664 the floor of the OR. The region where the particles are located is around the OT, surrounding the
 665 feet of four surgeons present in the CAD model. To better visualize the trajectories the squames



(a)



(b)

Figure 18: Contours of the mean velocity magnitude at $y = -0.162\text{m}$ (a) with blower-off and (b) with blower-on. The time average is taken over a physical time of 80s (no blower) and 37s (with blower) after establishing a stationary state.

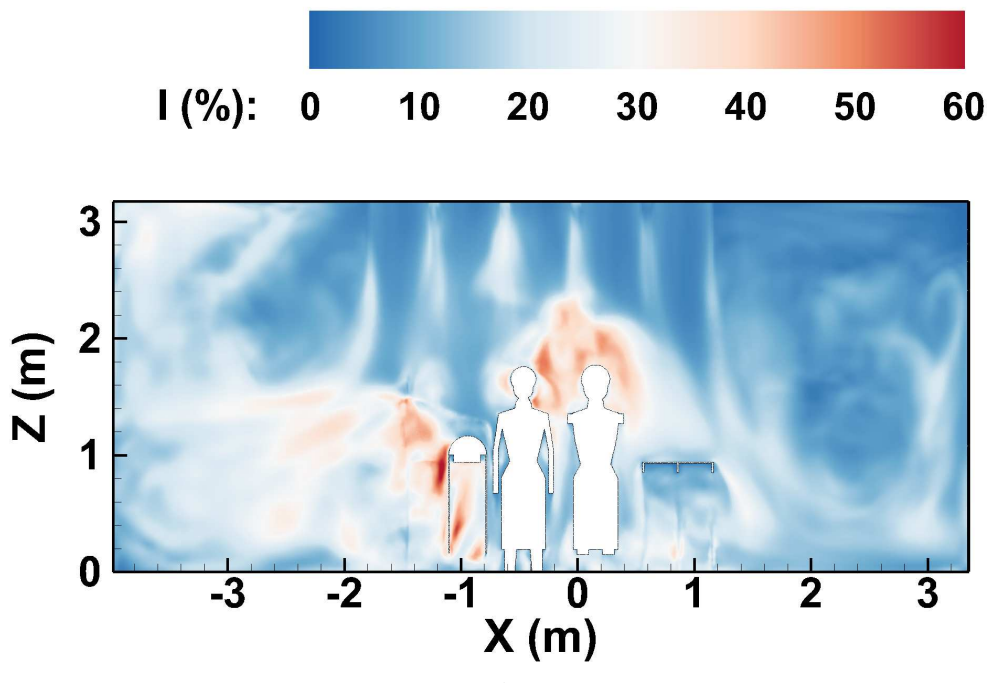
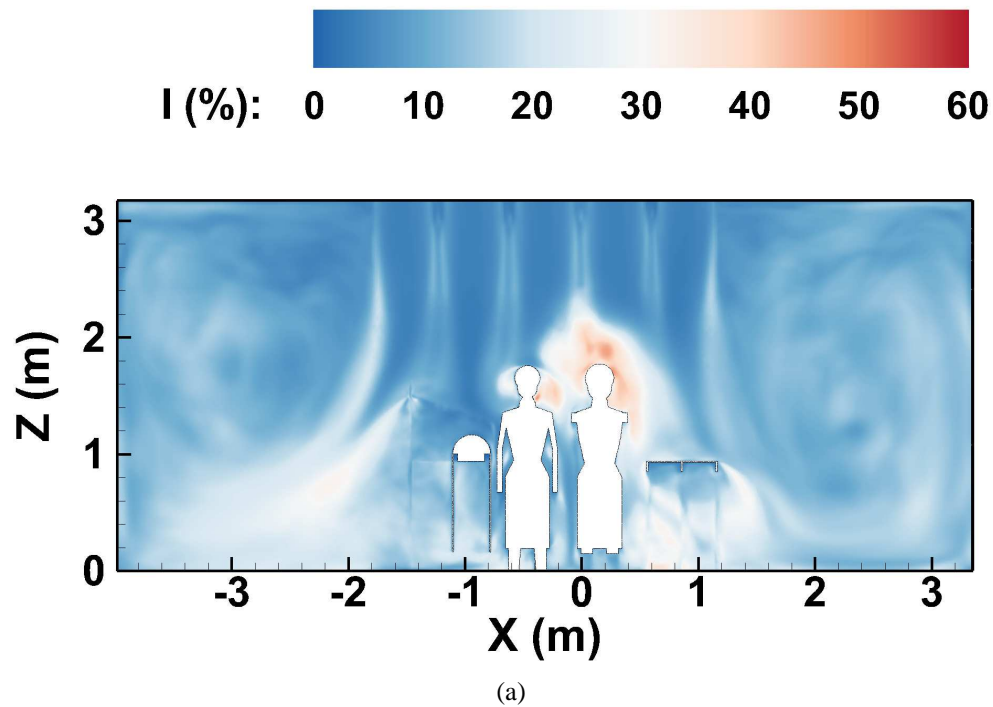
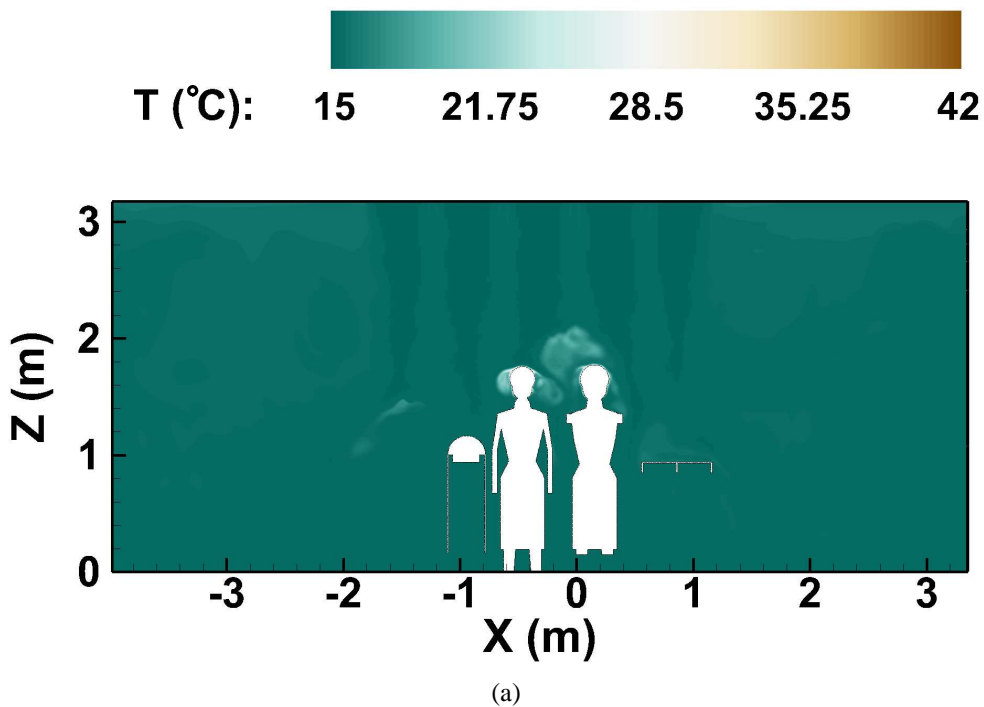
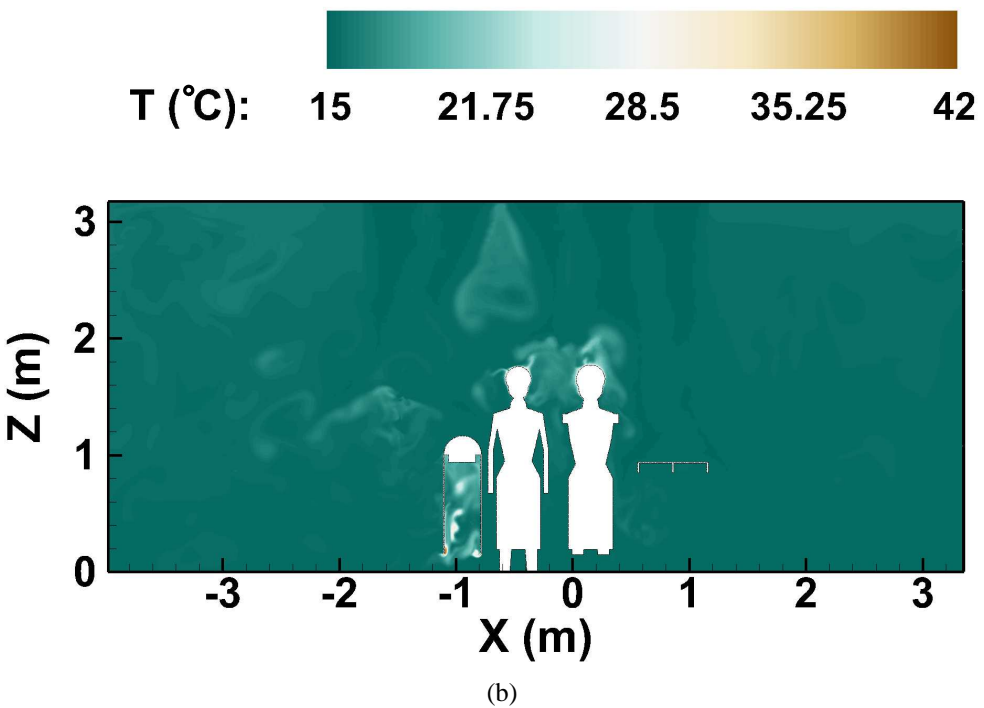


Figure 19: The turbulence intensity contours at $y = -0.162\text{m}$ (a) with blower-off and (b) with blower-on. The time average is taken over a physical time of 80s (no blower) and 37s (with blower) after establishing a stationary state.



(a)



(b)

Figure 20: The instantaneous temperature contours at $y = -0.162\text{m}$ (a) with blower-off and (b) with blower-on. These snapshots are at about 35s after a stationary flow field was obtained and calculation for flow statistics was initiated.

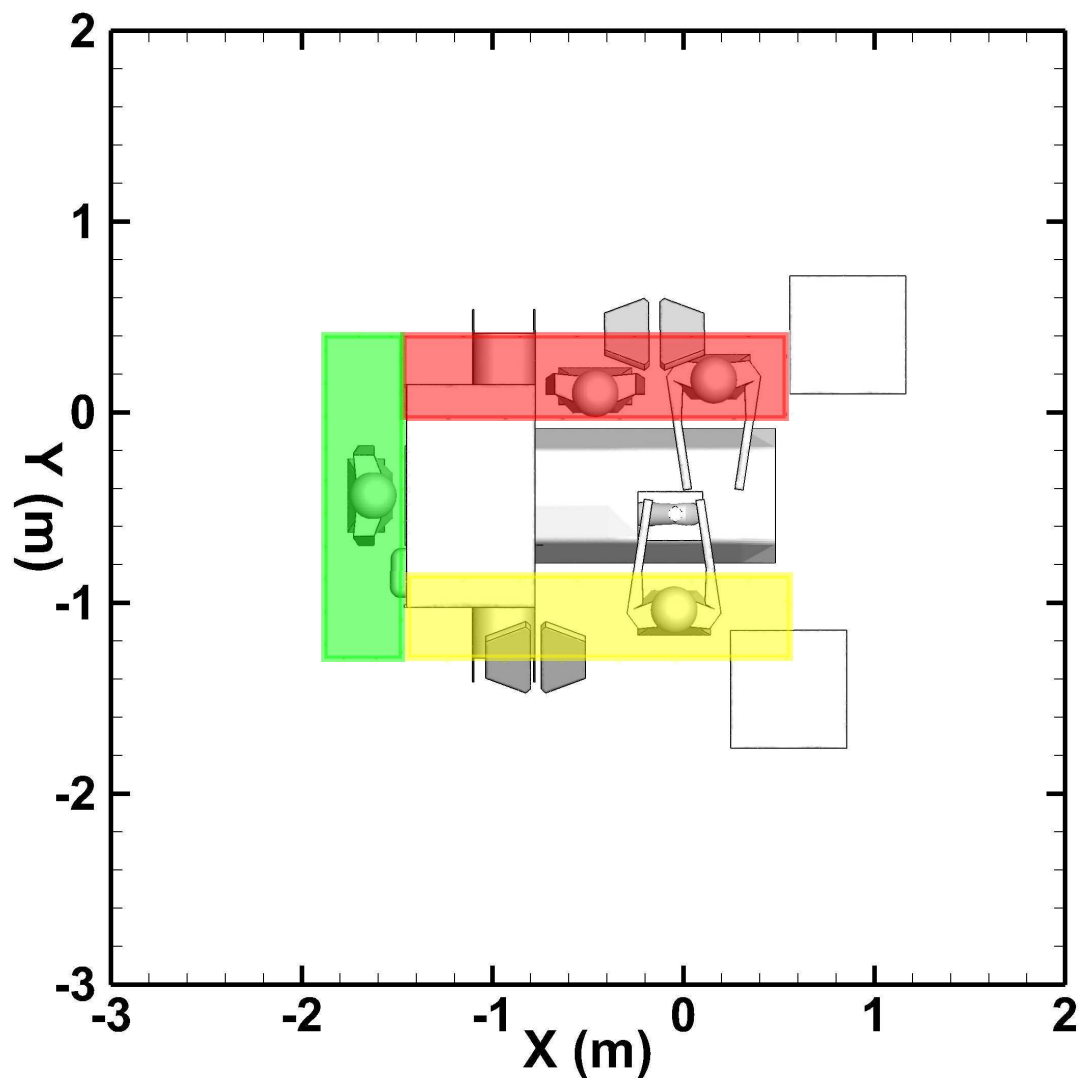


Figure 21: Three color-coded regions where the 3 million squames were initially distributed within a 1 cm height from the floor.

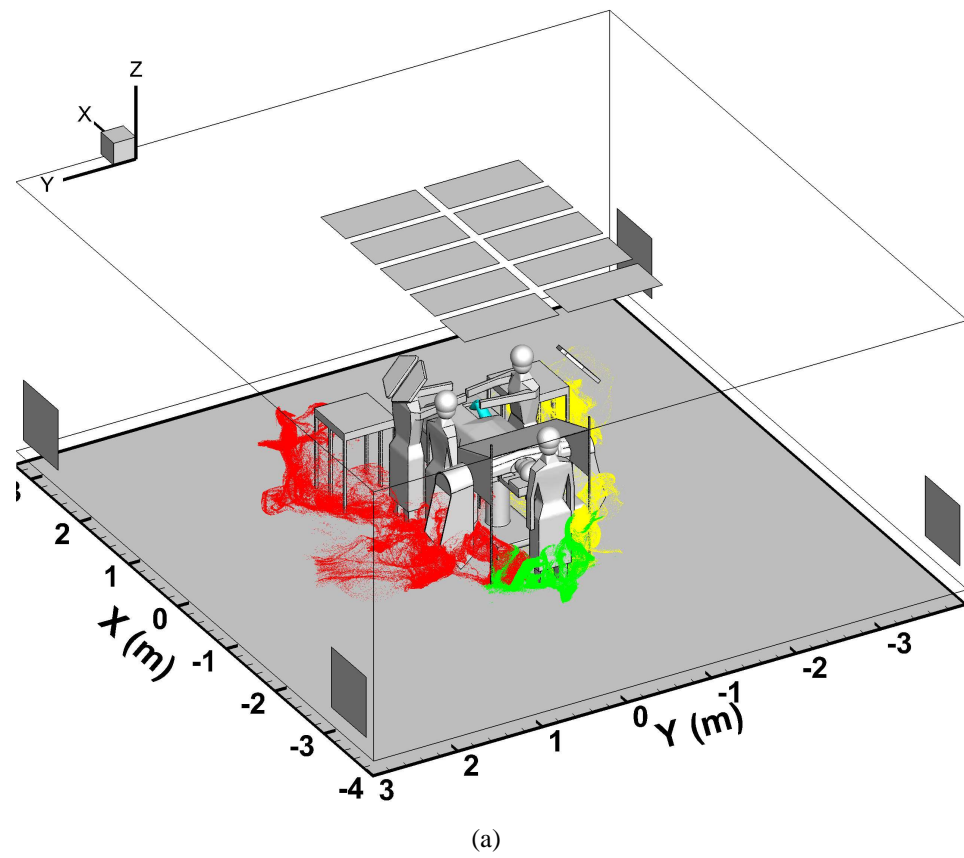
666 from different initial locations, the U-shaped region is divided into three rectangular sections color-
 667 coded as (i) red, (ii) green and (iii) yellow as shown in figure 21. One million squames are placed in
 668 each of the three sections at the same time, providing equal probability for the statistical analysis of
 669 motion of squames. The position of an individual squame particle in a section is chosen randomly
 670 using a uniform distribution. The squames of each section are tagged with distinct IDs. The actual
 671 coordinates of the three sections are given in Table 3.

672 4.2.2 Trajectories and snapshots of squames

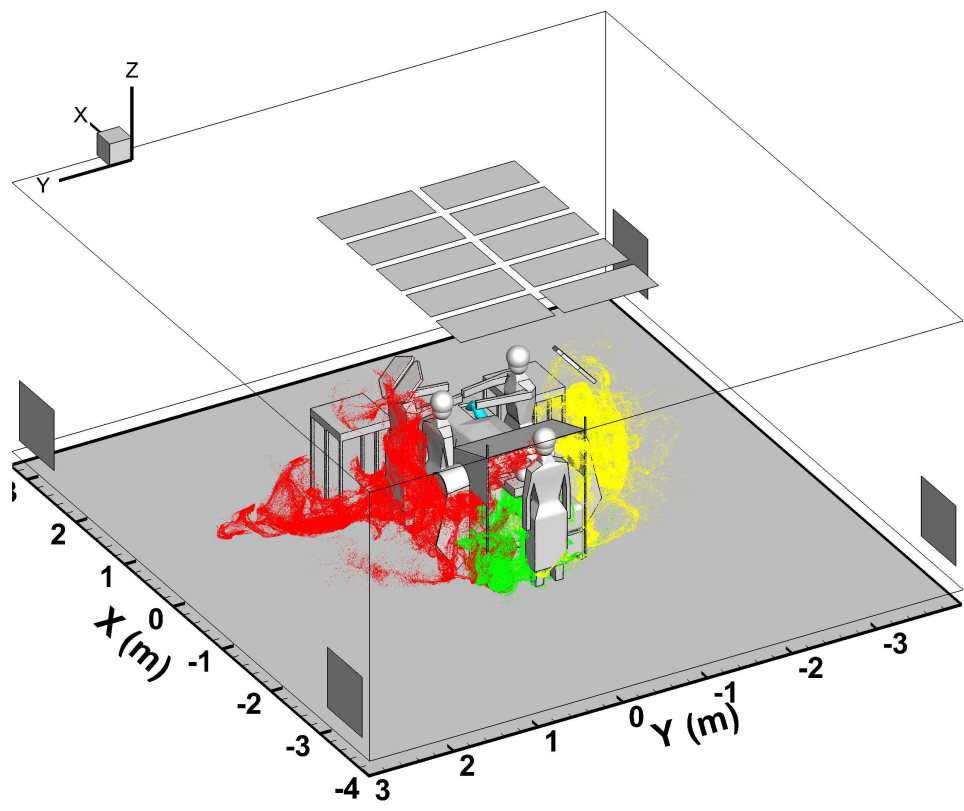
673 In order to visualize the effect of the hot blower air on the trajectory of squames, instantaneous
 674 scatter plots of squames are displayed at 10s and 20s after their initiation with blower-off and blower-
 675 on in figures 22a,b and 23a,b, respectively. The squames are also color-coded based on their region
 676 of origin as highlighted in figure 21. Drastic differences between the blower-off and blower-on
 677 cases are observed. It is clear from figures 23a that the majority of the squames are dispersed by the
 678 ventilation air flow towards the outlet grilles when the blower is off. None of the squames actually
 679 rise to the level of the side tables or the OT. In contrast, in the case of blower-on, a large number of
 680 squames are lifted upwards by the rising thermal plumes. Some of the squames (mostly red-colored
 681 and some yellow-colored) are lifted above the surgeons heads and are blown towards the OT by
 682 the incoming ventilation air. Large number of squames are seen to be above the OT, several are
 683 surrounding the surgeons hands, above the side tables, and some are very close to the patient's knee
 684 and the surgical site. This is better visualized by the zoom-in view shown in figures 24a,b.

685 Figures 25, 26, and 27 show a different view angle for the squames at the same time instances as
 686 in the above discussion. It is again seen that with the blower-on several particles are lifted upwards
 687 by the thermal plumes and rise above the operating table and then are blown downwards by the
 688 incoming ventilation air.

689 Finally, figure 28 shows an instantaneous snapshot of squames very close to the patient's knee.
 690 It seen that several of the red-coded particles are near the bottom of the knee, whereas some yellow-
 691 coded particles are in the very close vicinity of the surgical site. Several particles are still suspended
 692 above the OT and are being transported downwards by the ventilation air and may potentially reach
 693 close to the surgical site.

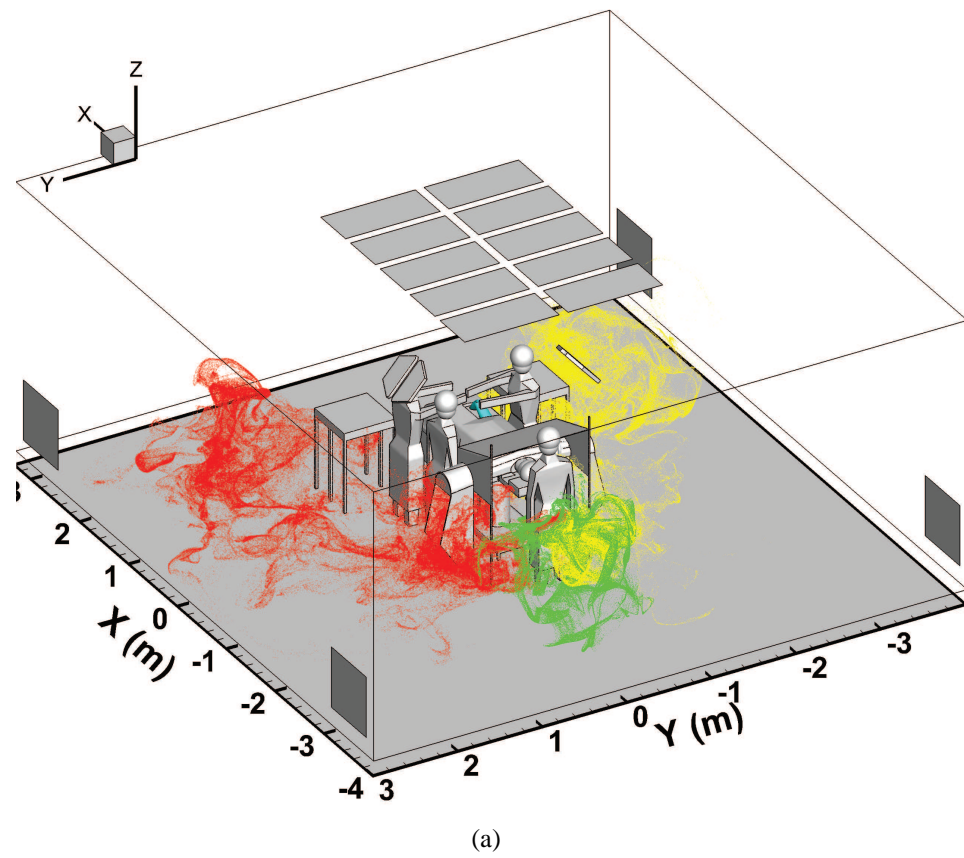


(a)

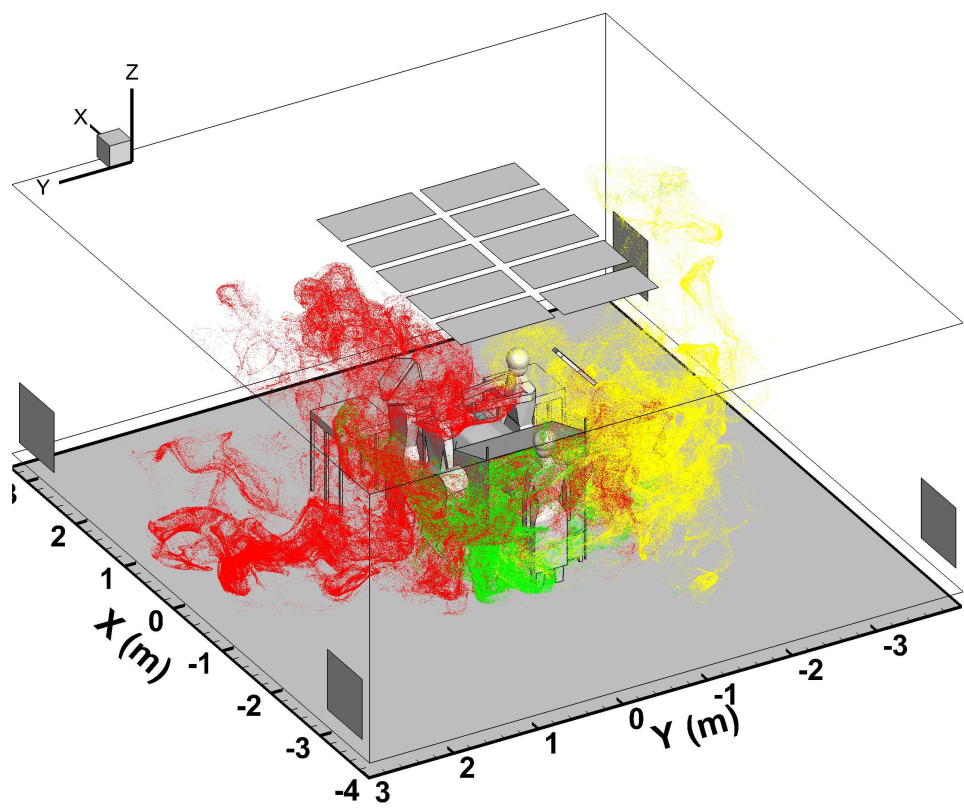


(b)

Figure 22: Instantaneous scatter plot of squames color-coded by their region of origin at 10s after initiation: (a) blower-off, (b) blower-on.

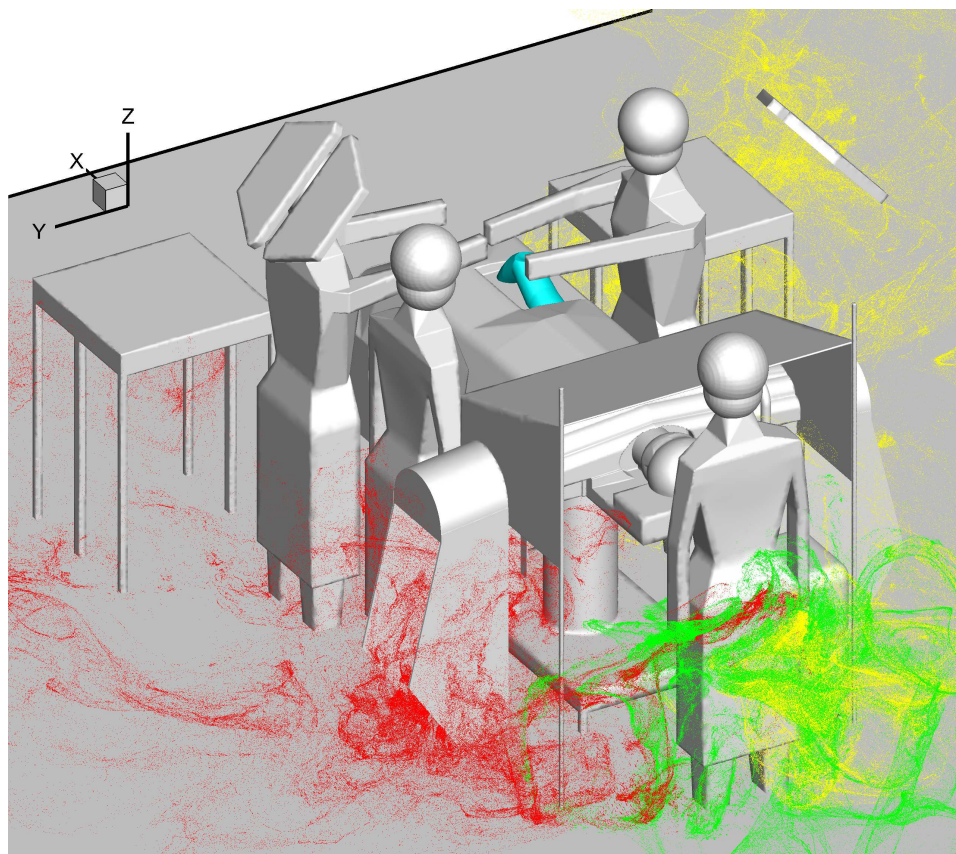


(a)

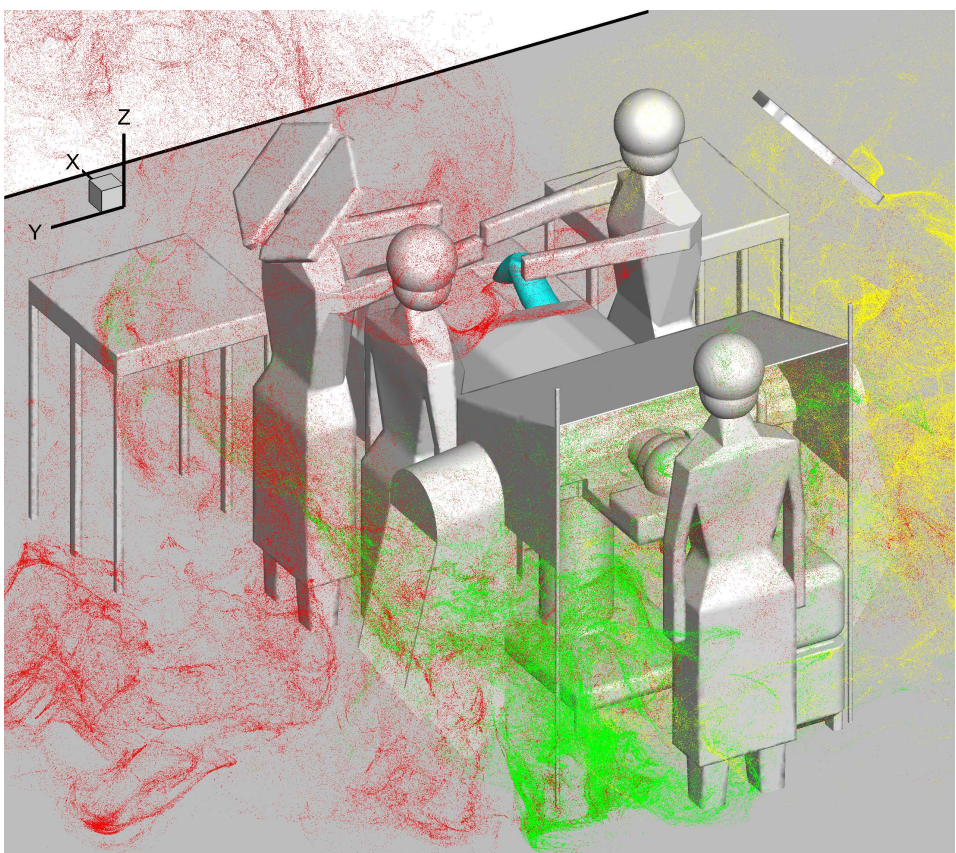


(b)

Figure 23: Instantaneous scatter plot of squames color-coded by their region of origin at 20s after initiation: (a) blower-off, (b) blower-on.

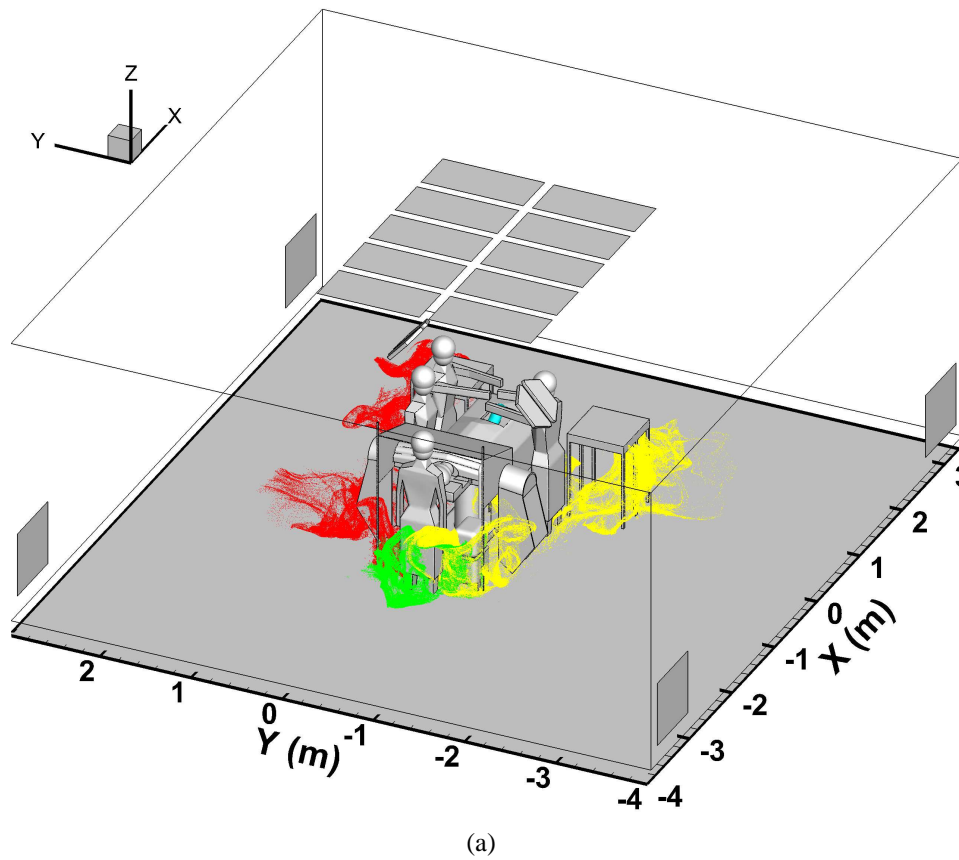


(a)

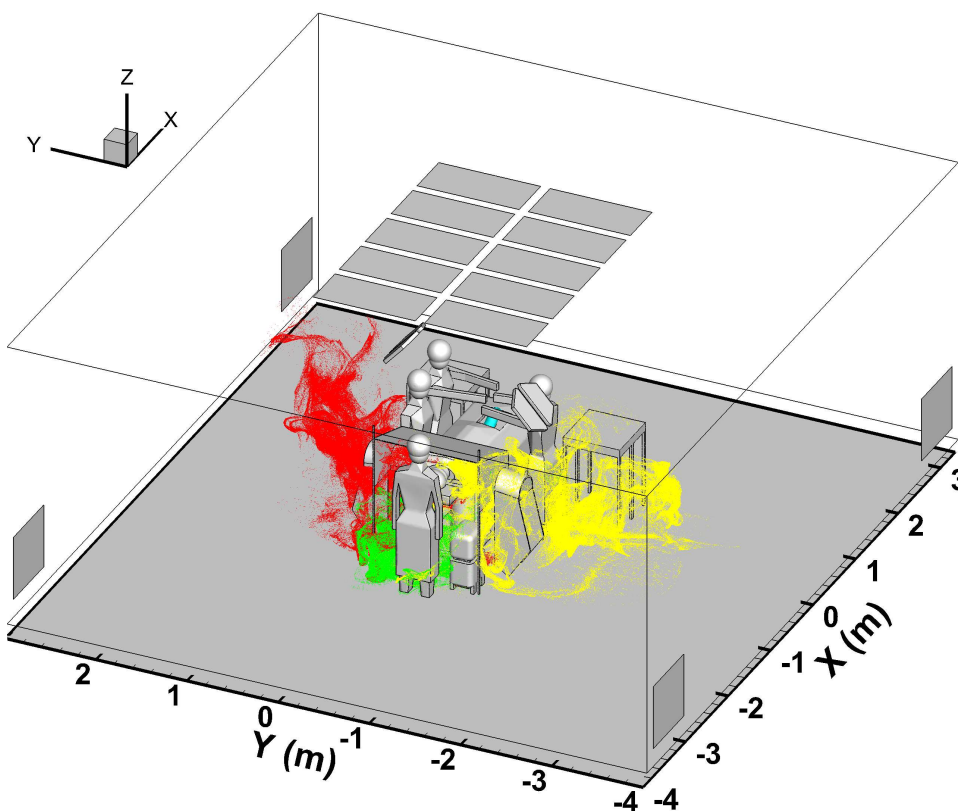


(b)

Figure 24: Zoom-in of the instantaneous scatter plot of squames color-coded by their region of origin at 20s after initiation: (a) blower-off, (b) blower-on.

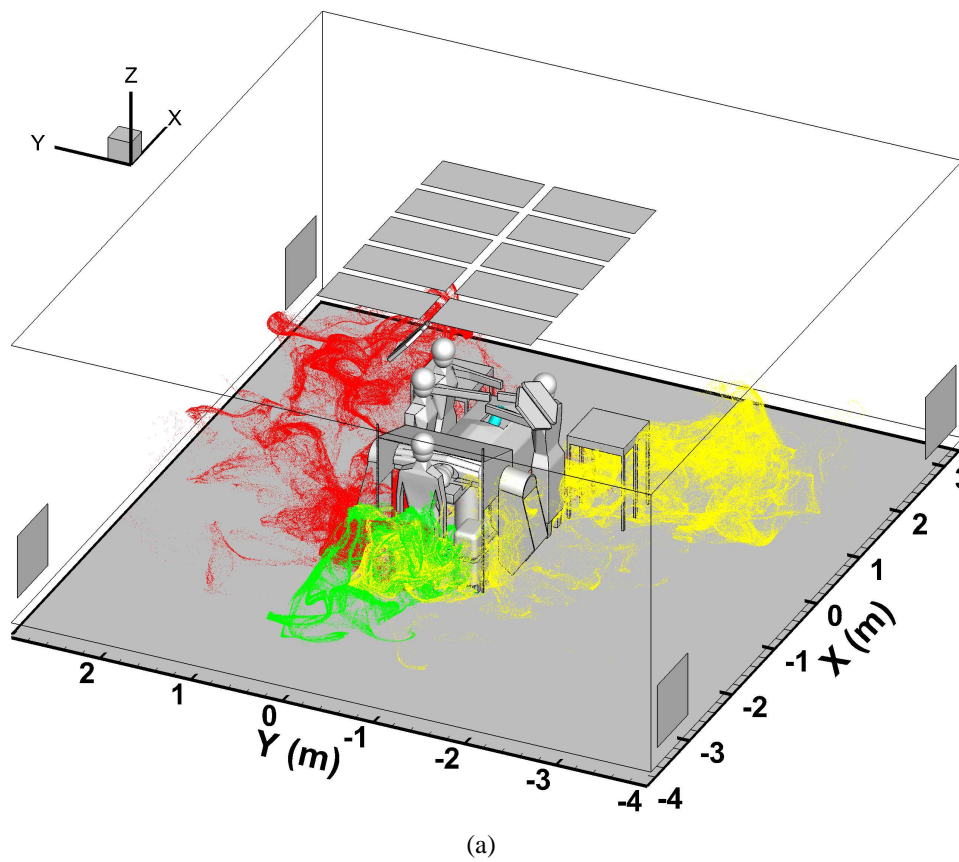


(a)

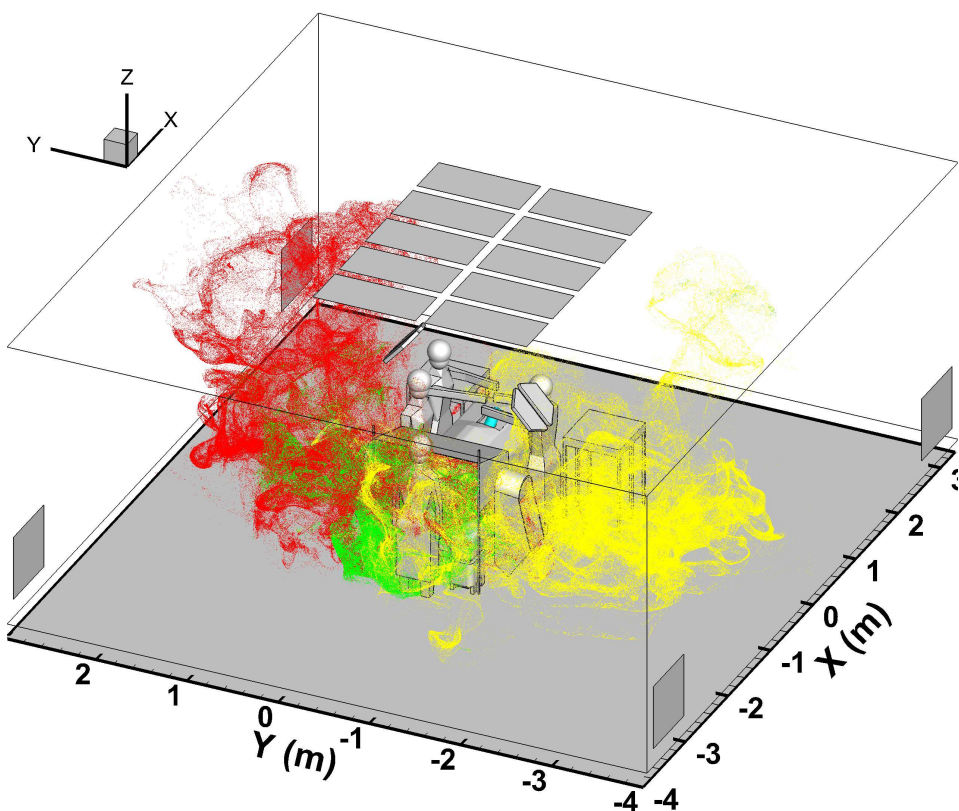


(b)

Figure 25: Instantaneous scatter plot of squames color-coded by their region of origin at 10s after initiation: (a) blower-off, (b) blower-on.

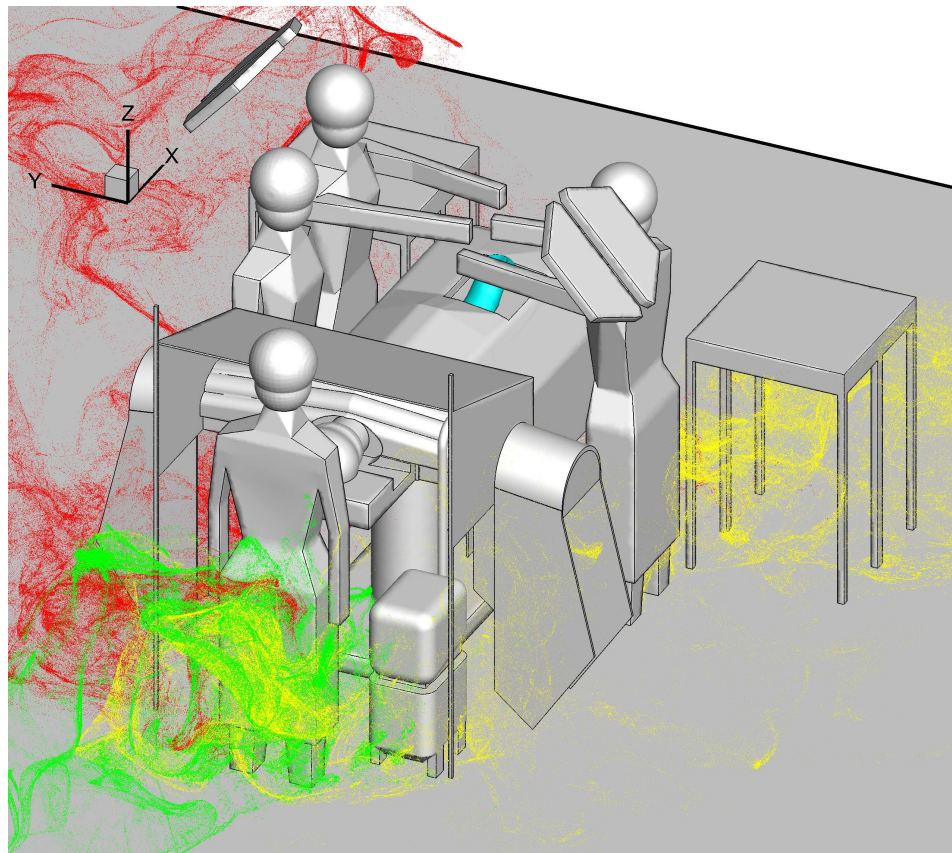


(a)

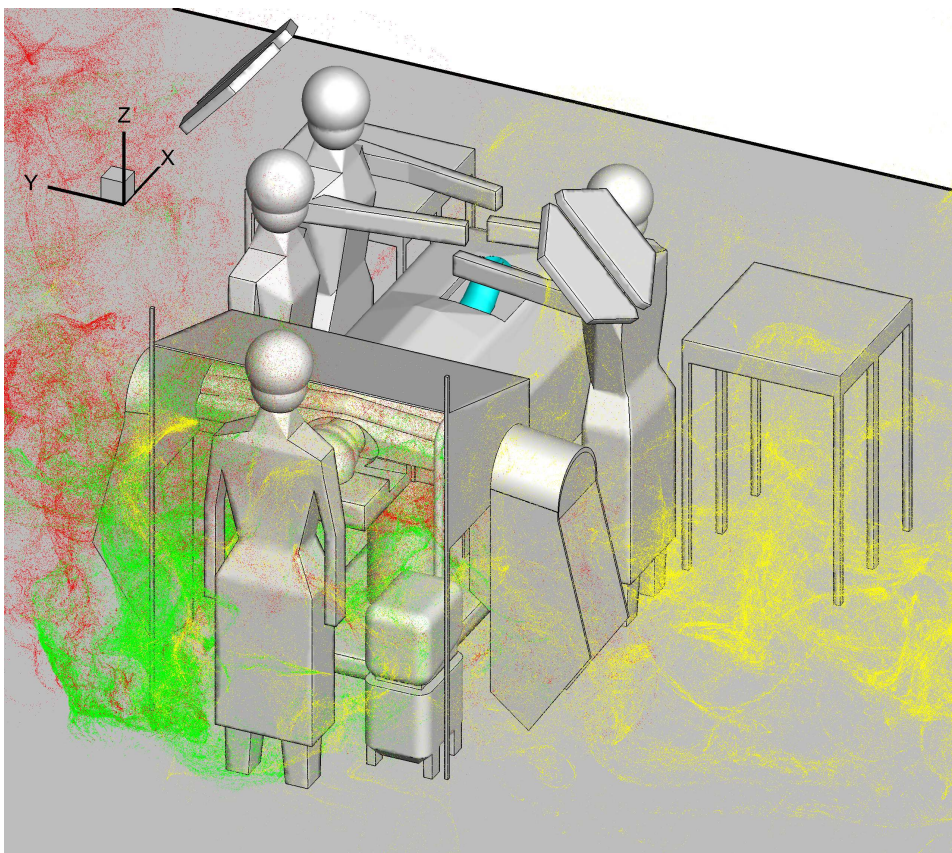


(b)

Figure 26: Instantaneous scatter plot of squames color-coded by their region of origin at 20s after initiation: (a) blower-off, (b) blower-on.



(a)



(b)

Figure 27: Zoom-in of the instantaneous scatter plot of squames color-coded by their region of origin at 20s after initiation: (a) blower-off, (b) blower-on.

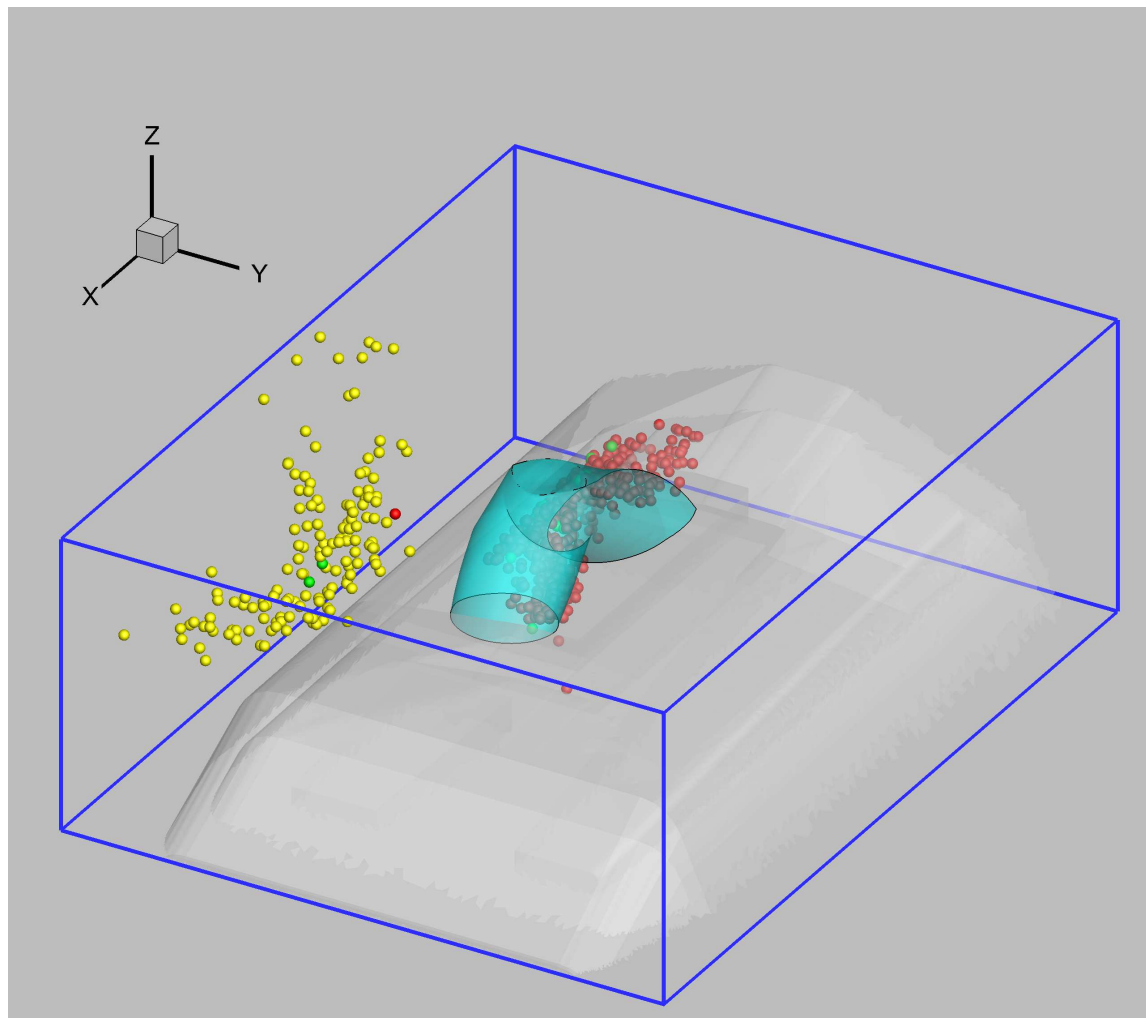


Figure 28: Zoom-in showing the instantaneous snapshot of squames near the surgical site at $t = 27\text{s}$.

694 **4.2.3 Number density of squames in the regions of interest**

695 To assess the probability of squames reaching the surgical site, four imaginary boxes were located
 696 as follows: two boxes covering the two side tables, a box around the OT, and a box around the
 697 patient's knee area. The surgeons and medical assistants are bound to use surgical instruments
 698 placed on the side tables. The possibility of squames reaching the surgical site is then dependent on
 699 the number density of squames within these four imaginary boxes (see figure 29). The number of
 700 squame particles inside the four boxes are recorded in time. A blue box (figure 29 (a) and (c)) is
 701 covering the whole OT. The top of this box is about 30 cm high, including the patient's whole body
 702 and the surgeons hands. An orange box (figure 29 (b) and (d)) is placed above the OT, just covering
 703 the patient's knee and part of the surgeon's hands; and the top of the box is only 2 cm above the
 704 surgeon's hands. One purple box (figure 29 (a) - (d)) is placed on each of the two side tables. The
 705 height of these boxes is about 1 cm, so that any surgical instrument placed on the side tables would
 706 be within the box.

707 Two computations of the trajectories of squames were performed after a statistically stationary
 708 flow field has been reached for the cases of blower-off and blower-on. Based on the average inlet
 709 air velocity and the height of the room, it takes 15 – 20s for a fluid particle to travel from the ceiling
 710 grille to the floor. First, the blower is turned off and only the ventilation air from the inlet grilles and
 711 thermal plumes created by the warm surfaces including surgical lights, surgeons' heads, patient's
 712 head, and patient's knee are responsible for the dispersion of squames. It was found that all the
 713 squames initiated in all three sections (red, green and yellow) are basically transported by the air
 714 flow reaching the floor and quickly dispersed to the for outlet grilles. After a calculation of about
 715 25s of physical time, some squame particles do rise to the underside of the side tables, but none of
 716 the squames was found to enter the four imaginary boxes representing the regions of interest. It was
 717 concluded that without the hot air discharged from the blower, the ventilation air circulation alone
 718 cannot disperse the squames to the surgical site. The thermal plumes from various warm surfaces
 719 only slightly affect the air coming from the inlet grilles and do not affect the motion of the squames.

720 With the blower turned on, computations were carried out for about 30s of physical time to obtain
 721 a flow field with well established thermal plumes created by the hot air discharged from the blower.
 722 After reaching a stationary state, the squames were initiated in the same color-coded sections and the

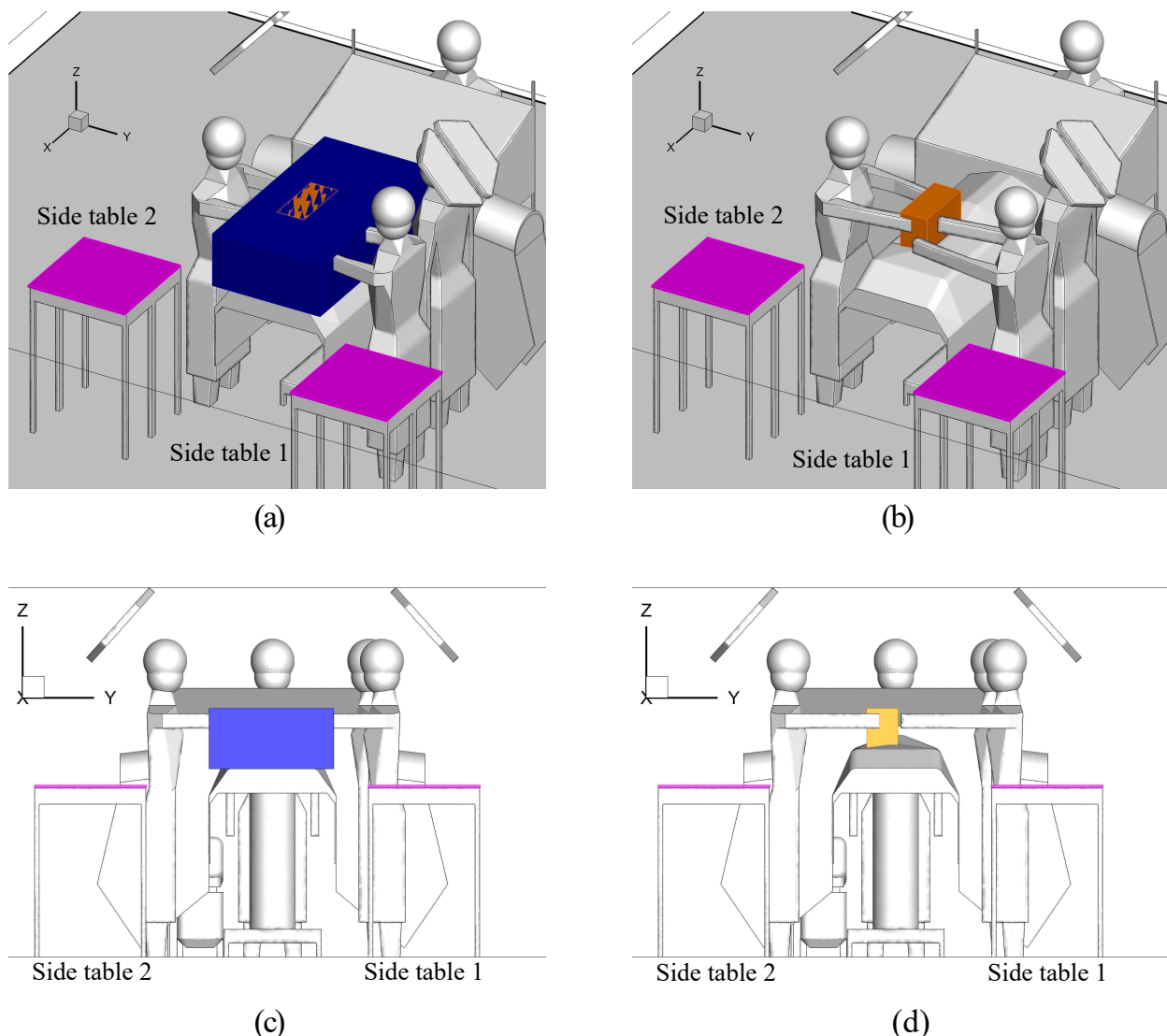
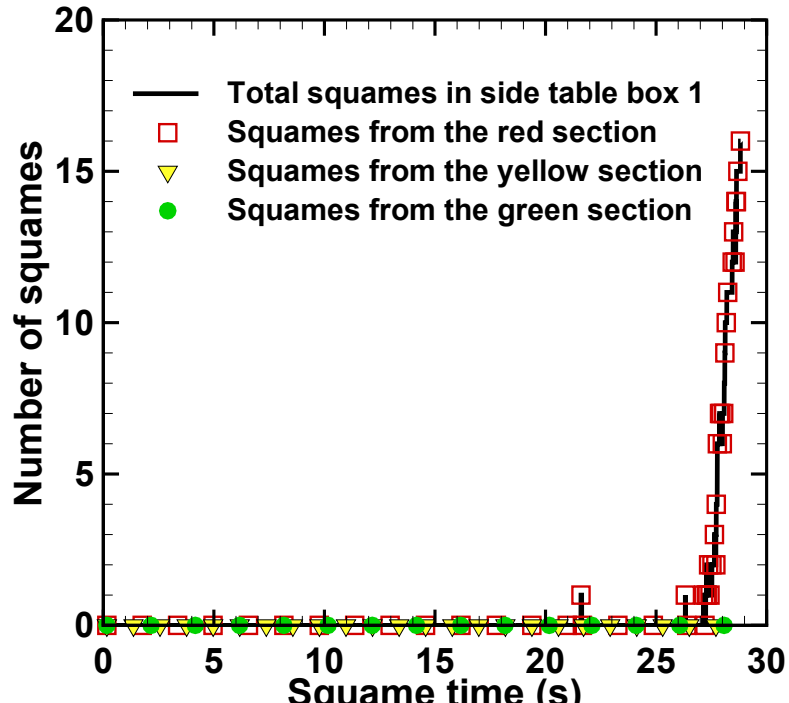


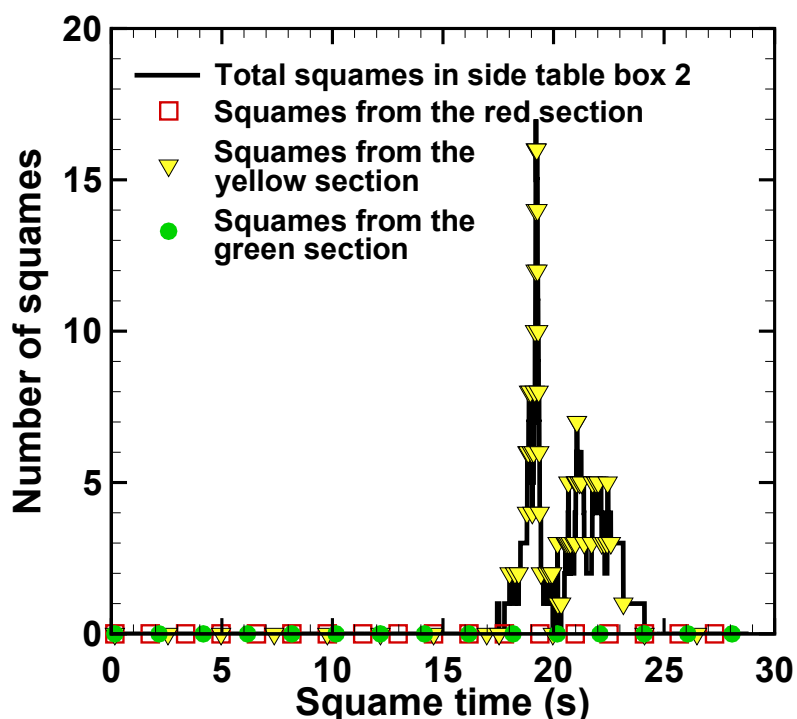
Figure 29: Four color-coded regions of interest, for recording the temporal history of the number of squames reaching them, shown in different views (a–d). The regions of interest include the zones above the two side tables, above the OT, and above the patient's knee.

723 computation continued for another 30s. With the blower on, hot air is discharged through the sides
 724 covering the patient's arms into the ambient air and strong thermal plumes rise under the operating
 725 table. Some of the edges of the drape are very close to the floor (see figure 4b) and the hot air plume
 726 drags squames with it making them rise upwards faster than in the case when the blower was off.
 727 A majority of the squame particles are transported away from the table towards the outlet grilles.
 728 However, a statistically significant number of particles are lifted above the operating table with some
 729 even reaching the height of the surgeons. The particles rise due to buoyancy and then get flushed
 730 down onto the operating table by the incoming ventilation air from the inlet grilles. The particles
 731 then do enter the imaginary boxes of interest, specifically above the operating table and the patient's
 732 knee.

733 Figures 30 and 31 show the number of squame particles as a function of time entering the four
 734 imaginary boxes of interest (above the side tables, above the operating table, and patient's knee). It
 735 can be seen from Figure 31b that no particles are found inside these boxes for the first 17s, which is
 736 about the time needed for the ventilation air to travel from the ceiling to the floor. After this time, the
 737 number of squame particles in the box above the OT increases almost in a linear fashion. Within 30s
 738 of physical time, the number of squame particles within the OT box are about 2500 and increasing.
 739 Figure 31a shows that at about 23s, some of the particles above the OT start to enter the box above
 740 the knee, which is a very narrow zone surrounding the patient's knee. The number of these particles
 741 increases linearly to about 600. Note that some of these particles do get trapped at the knee, some
 742 are carried away by the air flow and hence the number appears to be decreasing after about 25s .
 743 From the instantaneous snapshot of the squames shown in figures 24b and 27b, it can be seen that
 744 several particles are still above the OT and moving downward due to the air from the inlet grilles. It
 745 is thus expected that more particles will enter the box above the patient's knee, potentially raising
 746 the probability of infection. It is also interesting to note that the squame particles entering the box
 747 above the OT and above the knee are mainly the red-colored particles initiated from the side of the
 748 table with two surgeons. Owing to the asymmetry in the CAD model geometry, the flow pattern
 749 around each side of the table is different and the recirculation region created by the incoming air
 750 from the inlet grilles is also asymmetric. The rise and eventual trapping of the squames within the
 751 knee box is thus also related to which side of the table it originated from. The boxes above the side
 752 tables also entrain about 15 squame particles as can be seen from figures 30a,b. This suggests that

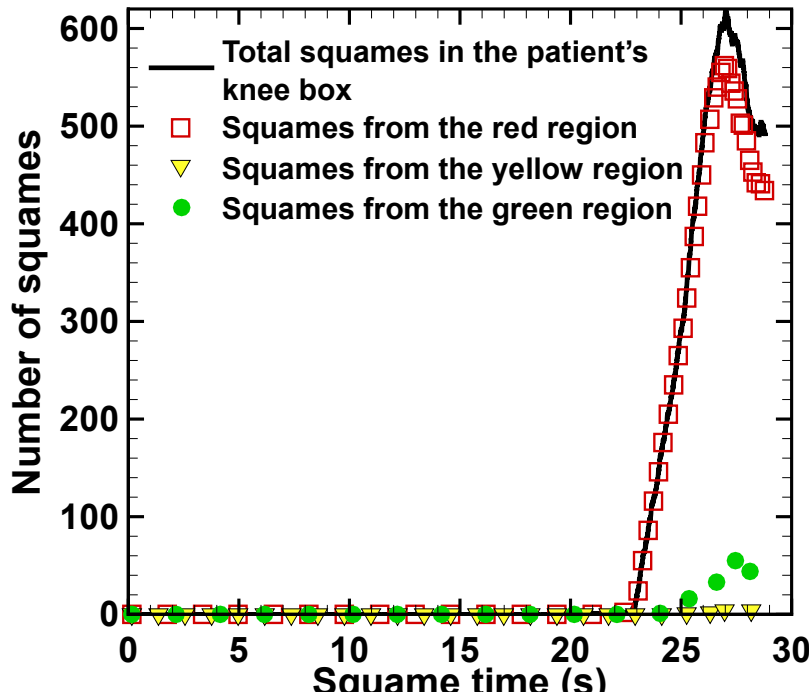


(a)

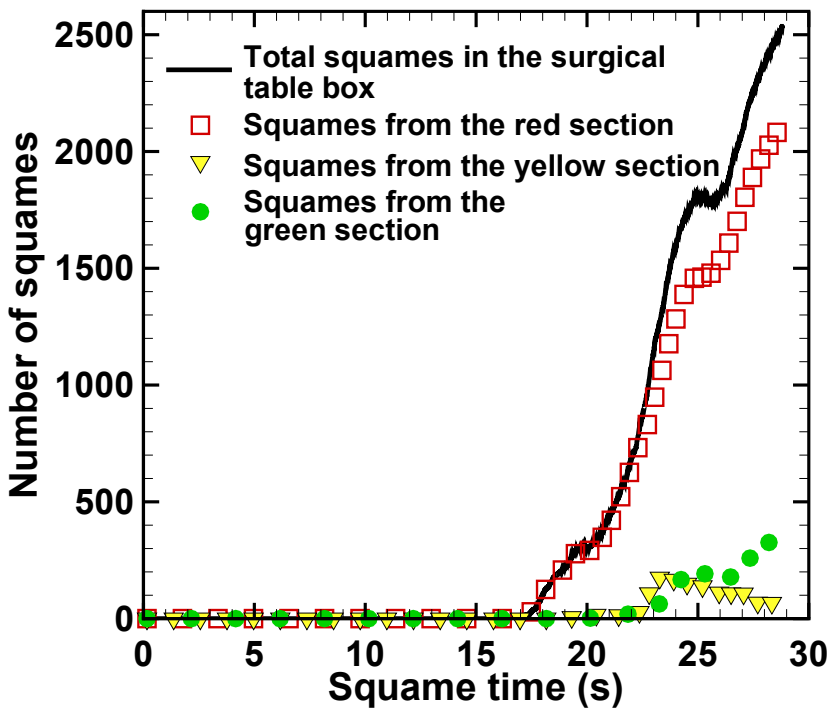


(b)

Figure 30: Temporal history of the total number of squames (shown by black color) entering four different regions of interest: (a) side table box 1, and (b) side table box 2Also shown in color is the number of color-coded squame particles entering from the red, green and yellow regions of the figure 21.



(a)



(b)

Figure 31: Temporal history of the total number of squames (shown by black color) entering four different regions of interest: (a) the patient's knee area, and (b) the OT box. Also shown in color is the number of color-coded squame particles entering from the red, green and yellow regions of the figure 21.

753 the surgical instruments on the side tables also have a small probability of carrying squames to the
 754 surgical site.

755 5 Summary and Concluding Remarks

756 A high-fidelity, large-eddy simulation (LES) was performed to study the interaction of the operat-
 757 ing room (OR) ultra-clean ventilation air flow and the flow created by a forced air warming system
 758 (3MTM Bair HuggerTM blower) and its impact on the dispersion of squames particles. A full three-
 759 dimensional design of an OR with operating table (OT), surgical lamps, medical staff, side tables,
 760 a blower, and a patient undergoing knee surgery was constructed. Unstructured grid elements in-
 761 volving hexahedra, tetrahedra, pyramids and wedges were used to capture the complex geometry of
 762 the OR. An arbitrary shaped, unstructured grid flow solver for LES based on governing equations
 763 for variable density in the limit of zero-Mach number was used. Ultraclean ventilation air enters the
 764 OR through 10 ceiling grilles with air changes per hour (ACH) of 24.45 and flow Reynolds num-
 765 ber, based on the air inlet grille size and mean air inlet velocity, of 9226. The air inlet flow was
 766 developed from a periodic duct flow with the required target mass flow rate for each grille. No-slip
 767 conditions were applied for all solid surfaces and convective outflow condition was used at the four
 768 outlet grilles. Temperature values were specified at the surfaces of inlet grilles, the surgical lamps,
 769 heads of the medical staff, patient's head, and patient's knee and all other boundary surfaces were
 770 assumed adiabatic. Computations were performed on 1600 processors in parallel and flow statistics
 771 involving the time-averaged mean velocity field, turbulence intensity, and temperature distribution
 772 were computed.

773 Two computations were performed with the blower-off and blower-on to calculate a three-
 774 dimensional, time-dependent flow within the OR. Rising thermal plumes from the warm surfaces
 775 of surgeons heads, the patient's knee, patient's head, and the surgical lamp were calculated. With
 776 the blower on, air was drawn from the floor of the OR, heated, and blown into a blanket that covers
 777 the torso region of the patient. The blanket was covered with a plastic drape. The blower hot air
 778 generated forced convective currents and strong thermal plumes that interacted with the ultra-clean
 779 ventilation air. For both cases, trajectories of 3 million squames, placed initially on the floor in a
 780 small region surrounding the OT and surgeons, were calculated and contrasted to quantify the effect

781 of the hot air blower. The squames particles were assumed to be spherical in shape with 10 micron
 782 diameter and density of liquid water. The particle trajectories were tracked in a Lagrangian frame
 783 by computing the drag, lift, and buoyancy forces. The temporal variations of the number of squames
 784 particles within four imaginary boxes placed strategically above the two side tables, over the OT,
 785 and one surrounding the patient's knee were calculated and contrasted between the blower-off and
 786 blower-on cases. The following main conclusions can be drawn from these predictive computations:

- 787 1. For the case of blower-off, the ventilation air from the ceiling inlet grilles moves downwards,
 788 then is deflected by the surgical lights and the table, impinges on the floor farther away from
 789 the OT, and finally exits through the outlet grilles. Large recirculation regions are created on
 790 both sides of the table. The flow is not symmetric owing to asymmetries in the configuration
 791 of the OR contents. The maximum turbulence intensity level is about 30% in the high shear
 792 regions between the inlet air streams and the initial stagnant air in the OR, as well as near the
 793 warm surgical lights due to the buoyant plume. It is observed that the buoyant plumes from
 794 the patient's knee and other warm surfaces are relatively weak, and do not significantly alter
 795 the mean ventilation air flow.
- 796 2. For the case of blower-on, the mean flow underneath and around the OT is significantly mod-
 797 ified and large levels of turbulence intensity are observed under the OT. The turbulence inten-
 798 sity levels are as high as 60% in regions affected by the rising thermal plumes from the blower.
 799 The instantaneous temperature contours confirm that the increased turbulence level is mainly
 800 because of the thermal plumes from the hot blower air causing higher temperature regions un-
 801 der the OT in comparison with the blower-off case. The flow is also highly asymmetric owing
 802 to the orientation and location of the drape. The rising thermal plumes are even observed to
 803 reach the ceiling in some regions and the downward ventilation flow from the inlet grilles was
 804 modified above the OT which also affected the recirculation region.
- 805 3. Drastic differences in the trajectories of the squames are observed between the blower-off
 806 and blower-on cases. With the blower-off, the majority of the squames are dispersed by the
 807 ventilation air flow towards the outlet grilles. None of the squames actually rise to the level of
 808 the side tables or the OT. In contrast, with the blower-on, a large number of squames are lifted
 809 upwards by the rising thermal plumes. Some of the squames are lifted above the surgeons

heads and are blown towards the OT by the downward moving ventilation air. Large number of squames are seen to be above the OT, several are surrounding the surgeons hands, above the side tables, and some are very close to the patient's knee and the surgical site. Majority of the squames that come close to the surgical site were found to have originated from the sides parallel to the length of the OT.

4. With the blower off, none of the squames particles were found to enter the four imaginary boxes placed above the side tables, OT, and a region surrounding the patient's knee. Some particles are lifted from the floor over time, but none rise close to the level of the imaginary boxes as the downward flow due to the ventilation air keeps the particles closer to the floor. With the blower turned on, hot air discharged from the edges of the drape and the resultant thermal plumes drag the squames, making them rise upwards. Some of the squames rise above the surgeons heads in the recirculation region on the sides of the OT. These particles are then flushed down onto the OT by the ventilation air from the inlet grilles. Statistically significant particles do enter the imaginary boxes of interest above the operating table and the patient's knee. Few particles are also observed above the side tables.

Starting with the worst-case scenario of having squames on the floor, it was shown that the hot air from the blower and the resultant thermal plumes are capable of lifting the particles and transporting them to the side tables, above the operating table, and the surgical site. It should be emphasized that if we also include the repetitive motion of the surgeons, the motion of medical assistants to fetch the surgical instruments placed on the side tables, and the resulting suspended squames shed by all staff in the OR, then the probability of dispersing the squames to the surgical site will be increased even further.

Although computationally intensive, large-eddy simulation of convective ventilation air flow and hot air from the blower in an OR is necessary to provide reliable predictions of the turbulent flow and dispersion of squames.

835 **Appendix A**

836 The aerodynamic behavior of squames suspended in a fluid is in general dependent upon the size and
 837 shape of the squames, their density, relative velocity with respect to the fluid motion, and density of
 838 the fluid. In the present study, the squames are suspended in air at room temperature (density ρ_g).
 839 The human skin cells or squames typically are disc-shaped with a diameter ranging from 4–20 μm
 840 and a thickness of 3–5 μm with density close to that of liquid water ($\rho_p = 1000\text{kg/m}^3$) (Noble *et al.*,
 841 1963; Noble, 1975; Snyder, 2009).

842 Settling of a squame particle depends on its weight, the drag and buoyancy force on the particle,
 843 and its orientation relative to the flow direction. Owing to the changes in orientation and also re-
 844 sultant rotation and torque on disc particles, computing large number of trajectories in a Lagrangian
 845 frame is complicated. It is thus easier to assume these particles of spherical shape with an equivalent
 846 diameter such that their aerodynamic characteristics are matched. An equivalent diameter of the
 847 spherical particle should be calculated by matching the settling velocities for the two shapes.

848 Since $\rho_p/\rho_g = 1000$, the buoyancy force is much smaller compared to the weight of the particle.
 849 Then the settling velocity can be obtained from the balance of drag and gravitational forces,

$$F_d = F_g. \quad (24)$$

The drag and gravitational forces on a disc-shaped particle are given as,

$$F_d = C_{d,\text{disc}} \frac{1}{2} \rho_g U_{\text{disc}}^2 A_p, \quad (25)$$

$$F_g = (A_p h_{\text{disc}}) \rho_p g; \quad A_p = \frac{\pi}{4} D_{p,\text{disc}}^2 \quad (26)$$

850 where U_{disc} is the settling velocity of the disc, $C_{d,\text{disc}}$ is the drag coefficient, A_p is the frontal area of
 851 the circular disc, g is the gravitational acceleration, $D_{p,\text{disc}}$ is the diameter, and h_{disc} is the thickness
 852 of the disc. Equating the drag force to the weight of the disc to obtain the settling velocity as,

$$U_{\text{disc}} = \sqrt{2g \left(\frac{\rho_p}{\rho_g} \right) \left(\frac{h_{\text{disc}}}{C_{d,\text{disc}}} \right)}. \quad (27)$$

Following similar procedure, the settling velocity of a sphere of diameter $D_{p,\text{sphere}}$ can be ob-

tained as,

$$U_{\text{sphere}} = \sqrt{\frac{4}{3}g \left(\frac{\rho_p}{\rho_g} \right) \left(\frac{D_{p,\text{sphere}}}{C_{d,\text{sphere}}} \right)}, \quad (28)$$

where $C_{d,\text{sphere}}$ is the drag coefficient on a spherical particle.

In order to match the aerodynamic performance of the two shapes, the two settling velocities should be the same. Equating U_{disc} and U_{sphere} we get,

$$D_{p,\text{sphere}} = \frac{3}{2}h_{\text{disc}} \left(\frac{C_{d,\text{sphere}}}{C_{d,\text{disc}}} \right). \quad (29)$$

For Stokes flow ($Re \leq 1$), the drag coefficients are given as (Munson *et al.*, 1990),

$$C_{d,\text{sphere}} = \frac{24}{Re} \quad (30)$$

$$C_{d,\text{disc}} = \frac{20.4}{Re}, \quad \text{flow normal to circular disc} \quad (31)$$

$$= \frac{13.6}{Re}, \quad \text{flow parallel to circular disc.} \quad (32)$$

Using a disc thickness of $h_{\text{disc}} = 5\mu\text{m}$, and using the drag coefficients for the disc and the sphere, equation (29) gives an equivalent spherical diameter in the range of $D_{p,\text{sphere}} = 8.78$ and $13.2\mu\text{m}$. Thus, an assumption of 10 micron spherical particle is reasonable to obtain similar dispersion behavior on an average as that of the disc-shaped squames particles.

860 **References**

- 861 ALBRECHT, MARK, GAUTHIER, ROBERT L, BELANI, KUMAR, LITCHY, MARK & LEAPER,
 862 DAVID 2011 Forced-air warming blowers: An evaluation of filtration adequacy and airborne con-
 863 tamination emissions in the operating room. *American journal of infection control* **39** (4), 321–
 864 328.
- 865 APTE, SV, GOROKHOVSKI, M. & MOIN, P. 2003a LES of atomizing spray with stochastic mod-
 866 eling of secondary breakup. *International Journal of Multiphase Flow* **29** (9), 1503–1522.
- 867 APTE, SV, MAHESH, K. & LUNDGREN, T. 2008a Accounting for finite-size effects in simulations
 868 of disperse particle-laden flows. *International Journal of Multiphase Flow* **34** (3), 260–271.
- 869 APTE, SV, MAHESH, K. & MOIN, P. 2008b Large-eddy simulation of evaporating spray in a
 870 coaxial combustor. *Proceedings of the Combustion Institute* **32**, accepted for publication.
- 871 APTE, SV, MAHESH, K., MOIN, P. & OEFELIN, JC 2003b Large-eddy simulation of swirling
 872 particle-laden flows in a coaxial-jet combustor. *International Journal of Multiphase Flow* **29** (8),
 873 1311–1331.
- 874 APTE, SOURABH V, MAHESH, KRISHNAN, GOROKHOVSKI, MICHAEL & MOIN, PARVIZ 2009
 875 Stochastic modeling of atomizing spray in a complex swirl injector using large eddy simulation.
 876 *Proceedings of the Combustion Institute* **32** (2), 2257–2266.
- 877 AUSTIN, PAUL N 2015 Guest editorial. *AANA journal* **83** (4), 237.
- 878 CHEN, X-Q & PEREIRA, JCF 1998 Computation of particle dispersion in turbulent liquid flows
 879 using an efficient lagrangian trajectory model. *International journal for numerical methods in
 880 fluids* **26** (3), 345–364.
- 881 CHOW, TIN-TAI & WANG, JINLIANG 2012 Dynamic simulation on impact of surgeon bending
 882 movement on bacteria-carrying particles distribution in operating theatre. *Building and Environ-
 883 ment* **57**, 68–80.
- 884 CLARK, RAYMOND P. & DE CALCINA-GOFF, MERVYN L. 2009 Some aspects of the airborne
 885 transmission of infection. *Journal of The Royal Society Interface* **6** (Suppl 6), S767–S782.

- 886 CROWE, CT, TROUTT, TR & CHUNG, JN 1996 Numerical models for two-phase turbulent flows.
- 887 *Annual Review of Fluid Mechanics* **28** (1), 11–43.
- 888 DRUZHININ, OA & ELGHOBASHI, S. 1998 Direct numerical simulations of bubble-laden turbulent
- 889 flows using the two-fluid formulation. *Physics of Fluids* **10**, 685.
- 890 EATON, JK & FESSLER, JR 1994 Preferential concentration of particles by turbulence. *Interna-*
- 891 *tional Journal of Multiphase Flow* **20**, 169–209.
- 892 EATON, J.K. & SEGURA, J.C. 2006 On momentum coupling methods for calculation of turbulence
- 893 attenuation in dilute particle-laden gas flows. *Fluid Mechanics and its Applications* **81**, 39.
- 894 ELGHOBASHI, S. 1994 On predicting particle-laden turbulent flows. *Flow, Turbulence and Com-*
- 895 *bustion* **52** (4), 309–329.
- 896 ELGHOBASHI, S. 2006 An updated classification map of particle-laden turbulent flows. *Fluid Me-*
- 897 *chanics and Its Applications* **81**, 3–10.
- 898 FERRANTE, A. & ELGHOBASHI, S. 2004 On the physical mechanisms of drag reduction in a spa-
- 899 tially developing turbulent boundary layer laden with microbubbles. *Journal of Fluid Mechanics*
- 900 **503**, 345–355.
- 901 FERRANTE, A. & ELGHOBASHI, S. 2007 On the accuracy of the two-fluid formulation in direct
- 902 numerical simulation of bubble-laden turbulent boundary layers. *Physics of Fluids* **19**, 045105.
- 903 GERMANO, MASSIMO, PIOMELLI, UGO, MOIN, PARVIZ & CABOT, WILLIAM H 1991 A dynamic
- 904 subgrid-scale eddy viscosity model. *Physics of Fluids A: Fluid Dynamics (1989-1993)* **3** (7),
- 905 1760–1765.
- 906 HAM, F., APTE, S., IACCARINO, G., WU, X., HERRMANN, M., CONSTANTINESCU, G., MA-
- 907 HESH, K. & MOIN, P. 2003 Unstructured LES of reacting multiphase flows in realistic gas turbine
- 908 combustors. Annual Research Briefs 2003. *Center for Turbulence Research, NASA Ames/Stanford*
- 909 *Univ* pp. 139–160.
- 910 HAM, FRANK & IACCARINO, GIANLUCA 2004 Energy conservation in collocated discretization
- 911 schemes on unstructured meshes. *Annual Research Briefs* **2004**, 3–14.

- 912 KELLAM, MELISSA D, DIECKMANN, LORAIN S & AUSTIN, PAUL N 2013 Forced-air warming
 913 devices and the risk of surgical site infections. *AORN journal* **98** (4), 353–369.
- 914 KRAVCHENKO, AG & MOIN, PARVIZ 1997 On the effect of numerical errors in large eddy simu-
 915 lations of turbulent flows. *Journal of Computational Physics* **131** (2), 310–322.
- 916 KULICK, JD, FESSLER, JR & EATON, JK 2006 Particle response and turbulence modification in
 917 fully developed channel flow. *Journal of Fluid Mechanics Digital Archive* **277**, 109–134.
- 918 LEAPER, DAVID, ALBRECHT, MARK & GAUTHIER, ROBERT 2009 Forced-air warming: a source
 919 of airborne contamination in the operating room? *Orthopedic reviews* **1** (2), 28.
- 920 LEES, JULIENNE & BRIGHTON, WD 1972 Simulated human skin scales. *Journal of Hygiene*
 921 **70** (03), 557–565.
- 922 LEGG, AJ, CANNON, T & HAMER, AJ 2012 Do forced air patient-warming devices disrupt unidi-
 923 rectional downward airflow? *J Bone Joint Surg Br* **94** (2), 254–256.
- 924 MAHESH, K., CONSTANTINESCU, G., APTE, S., IACCARINO, G., HAM, F. & MOIN, P. 2006
 925 Large-eddy simulation of reacting turbulent flows in complex geometries. *Journal of Applied*
 926 *Mechanics* **73**, 374.
- 927 MAHESH, K., CONSTANTINESCU, G. & MOIN, P. 2004 A numerical method for large-eddy sim-
 928 ulation in complex geometries. *Journal of Computational Physics* **197** (1), 215–240.
- 929 MAXEY, MARTIN R & RILEY, JAMES J 1983 Equation of motion for a small rigid sphere in a
 930 nonuniform flow. *Physics of Fluids (1958-1988)* **26** (4), 883–889.
- 931 McGOVERN, PD, ALBRECHT, M, BELANI, KG, NACHTSHEIM, C, PARTINGTON, PF, CAR-
 932 LUKE, I & REED, MR 2011 Forced-air warming and ultra-clean ventilation do not mix. *J Bone*
 933 *Joint Surg Br* **93** (11), 1537–1544.
- 934 MCNEILL, JAMES, HERTZBERG, JEAN & ZHAI, ZHIQIANG JOHN 2013 Experimental investiga-
 935 tion of operating room air distribution in a full-scale laboratory chamber using particle image
 936 velocimetry and flow visualization .

- 937 MCNEILL, JAMES S *et al.* 2012 Field measurements of thermal conditions during surgical proce-
938 dures for the development of cfd boundary conditions. *ASHRAE Transactions* **118**, 596.
- 939 MEMARZADEH, FARHAD 2003 Reducing risks of surgery. *ASHRAE journal* **45** (2), 28.
- 940 MEMARZADEH, FARHAD & MANNING, ANDREW P 2002 Comparison of operating room ventila-
941 tion systems in the protection of the surgical site/discussion. *ASHRAE transactions* **108**, 3.
- 942 MITTAL, RAJAT & MOIN, PARVIZ 1997 Suitability of upwind-biased finite difference schemes for
943 large-eddy simulation of turbulent flows. *AIAA journal* **35** (8), 1415–1417.
- 944 MOIN, P. & APTE, SV 2006 Large-eddy simulation of realistic gas turbine combustors. *AIAA Jour-*
945 *nal* **44** (4), 698–708.
- 946 MOIN, P. & MAHESH, K. 1998 Direct numerical simulation: A tool in turbulence research. *Annual*
947 *Reviews in Fluid Mechanics* **30** (1), 539–578.
- 948 MOIN, P., SQUIRES, K., CABOT, W. & LEE, S. 1991 A dynamic subgrid model for compressible
949 turbulence and scalar transport. *Physics of Fluids A*. **3**, 2746–2757.
- 950 MORETTI, B, LAROCCA, AMV, NAPOLI, C, MARTINELLI, D, PAOLILLO, L, CASSANO, M,
951 NOTARNICOLA, A, MORETTI, L & PESCE, V 2009 Active warming systems to maintain pe-
952 rioperative normothermia in hip replacement surgery: a therapeutic aid or a vector of infection?
953 *Journal of Hospital Infection* **73** (1), 58–63.
- 954 MUNSON, BRUCE ROY, YOUNG, DONALD F & OKIISHI, THEODORE H 1990 Fundamentals of
955 fluid mechanics. *New York* **3** (4).
- 956 NG, V, LAI, A & HO, V 2006 Comparison of forced-air warming and electric heating pad for
957 maintenance of body temperature during total knee replacement. *Anaesthesia* **61** (11), 1100–1104.
- 958 NOBLE, WC 1975 Dispersal of skin microorganisms. *British Journal of Dermatology* **93** (4), 477–
959 485.
- 960 NOBLE, WC, LIDWELL, OM, KINGSTON, D *et al.* 1963 The size distribution of airborne particles
961 carrying micro-organisms. *J Hyg (Lond)* **61** (385), e391.

- 962 PEREIRA, MARCELO LUIZ & TRIBESS, ARLINDO 2005 A review of air distribution patterns in
 963 surgery rooms under infection control focus. *Revista de Engenharia Térmica* **4** (2).
- 964 PIERCE, C.D. & MOIN, P. 1998a Turbulent flow over three-dimensional dunes: 2. Fluid and bed
 965 stresses. *Physics of Fluids* **10**, 3041–3044.
- 966 PIERCE, CHARLES DAVID 2001 Progress-variable approach for large-eddy simulation of turbulent
 967 combustion. PhD thesis, Citeseer.
- 968 PIERCE, CHARLES D & MOIN, PARVIZ 1998b Large eddy simulation of a confined coaxial jet with
 969 swirl and heat release. *AIAA paper* **2892**.
- 970 PIOMELLI, U 2014 Large eddy simulations in 2030 and beyond. *Philosophical Transactions of
 971 the Royal Society of London A: Mathematical, Physical and Engineering Sciences* **372** (2022),
 972 20130320.
- 973 POPE, SB 2000 *Turbulent Flows*. Cambridge University Press.
- 974 POZORSKI, JACEK & APTE, SOURABH V 2009 Filtered particle tracking in isotropic turbulence
 975 and stochastic modeling of subgrid-scale dispersion. *International Journal of Multiphase Flow*
 976 **35** (2), 118–128.
- 977 READE, W.C. & COLLINS, L.R. 2000 Effect of preferential concentration on turbulent collision
 978 rates. *Physics of Fluids* **12**, 2530.
- 979 ROUSON, D.W.I. & EATON, J.K. 2001 On the preferential concentration of solid particles in tur-
 980 bulent channel flow. *Journal of Fluid Mechanics* **428**, 149–169.
- 981 SAARINEN, PEKKA E, KALLIOMÄKI, PETRI, TANG, JULIAN W & KOSKELA, HANNU 2015
 982 Large eddy simulation of air escape through a hospital isolation room single hinged doorwayval-
 983 idation by using tracer gases and simulated smoke videos. *PloS one* **10** (7), e0130667.
- 984 SAFFMAN, PGT 1965 The lift on a small sphere in a slow shear flow. *Journal of fluid mechanics*
 985 **22** (02), 385–400.

- 986 SESSLER, DANIEL I, OLMSTED, RUSSELL N & KUELPMANN, RUEDIGER 2011 Forced-air warming
 987 does not worsen air quality in laminar flow operating rooms. *Anesthesia & Analgesia* **113** (6),
 988 1416–1421.
- 989 SNYDER, OP 2009 A ‘Safe Hands’ hand wash program for retail food operations: a technical
 990 review. *Yeast* **55** (18.5), 14–8.
- 991 SOMMERFELD, M, ANDO, A & WENNERBERG, D 1992 Swirling, particle-laden flows through a
 992 pipe expansion. *Journal of fluids engineering* **114** (4), 648–656.
- 993 SRIDHAR, G. & KATZ, J. 1999 Effect of entrained bubbles on the structure of vortex rings. *J. Fluid
 994 Mech.* **397** (-1), 171–202.
- 995 STRAUB, A. 2016 *Bentley Microstation Design V8i, M/E Engineering, P.C.*. 150 North Chestnut
 996 Street, Rochester, NY 14604, www.meengineering.com.
- 997 TENNEKES, HENDRIK & LUMLEY, JOHN LEASK 1972 *A first course in turbulence*. MIT press.
- 998 WARTTIG, SHERYL, ALDERSON, PHIL, CAMPBELL, GILLIAN & SMITH, ANDREW F 2014 Inter-
 999 ventions for treating inadvertent postoperative hypothermia. *The Cochrane Library* .
- 1000 WOOD, AM, MOSS, C, KEENAN, A, REED, MR & LEAPER, DAVID J 2014 Infection control
 1001 hazards associated with the use of forced-air warming in operating theatres. *Journal of Hospital
 1002 Infection* **88** (3), 132–140.